UNIVERSITÀ DEGLI STUDI DI UDINE
DOTTORATO DI RICERCA IN
SCIENZE DELL'INGEGNERIA ENERGETICA E AMBIENTALE
XXXII CICLO

TECHNISCHE UNIVERSITÄT WIEN
DOKTORATSSTUDIUM DER
TECHNISCHE WISSENSCHAFTEN MASCHINENBAU

Numerical simulations of breakage, coalescence and droplet size distribution

Giovanni Soligo

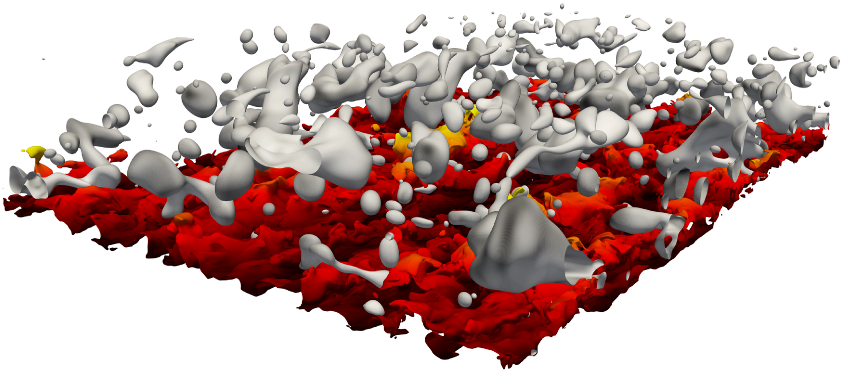

BOARD MEMBERS

Prof. Luca Brandt	COMMITTEE MEMBER
Prof. Günter Brenn	COMMITTEE MEMBER
Prof. Alfredo Soldati	SUPERVISOR
Prof. Cristian Marchioli	CO-SUPERVISOR
Prof. Alessandro Trovarelli	DOCTORATE CHAIR

Author's e-mail:
soligo.giovanni@spes.uniud.it
giovanni.soligo@tuwien.ac.at

Author's address:
Dipartimento Politecnico di Ingegneria e Architettura
Università degli Studi di Udine
Via delle Scienze 206
33100 Udine, Italy
Web: `DIEGM - University of Udine`

Institute of Fluid Mechanics and Heat Transfer
Technische Universität Wien
Getreidemarkt 9/E322
1060 Wien, Austria
Web: `ISW - TU Wien`

Cover:
Instantaneous representation of the droplets at $t^+ = 3750$ (case $We = 3.00$, $\beta_s = 4.00$). Droplets (iso-contour $\phi = 0$) are colored by the local surfactant concentration (white: low, black: high). The flow field is visualized via the streamwise velocity iso-surface (corresponding to $u^+ = 15$) colored by the distance from the bottom wall (black-near wall, yellow-channel centre).

Abstract

The dynamics of surfactant-laden droplets are investigated in this thesis using Direct Numerical Simulations (DNS) of turbulence coupled with a two-order-parameter Phase Field (PF) method to describe interface and surfactant dynamics. This problem is characterized by the presence of a deformable interface transported by the (eventually turbulent) flow and of a soluble surfactant. The complex interplay among flow, interface and surfactant, whose effects are deeply intertwined, is presented in detail in the following chapters and is also briefly summarized here with the help of the graphical abstract. The flow deforms the interface and advects surfactant via the shear stresses at the interface. In turn, the interface feeds back onto the flow field via capillary stresses (normal to the interface). The interface also, while deforming, breaking and merging, modifies the local surfactant concentration over the interface. Surfactant locally reduces surface tension of the interface, changing the local deformability of the interface. In addition, eventual surface tension gradients, generated by an uneven surfactant distribution, introduce stresses tangential to the interface (Marangoni stresses). Surfactant, indeed, feeds back onto the flow field via Marangoni stresses and onto the interface by locally reducing surface tension.
In the thesis, the outcome of this complex interplay is characterized, starting from simpler laminar cases (as for instance the deformation and interaction of droplets in laminar flow) and concluding with the more complex case of a swarm of surfactant-laden droplets in turbulence.

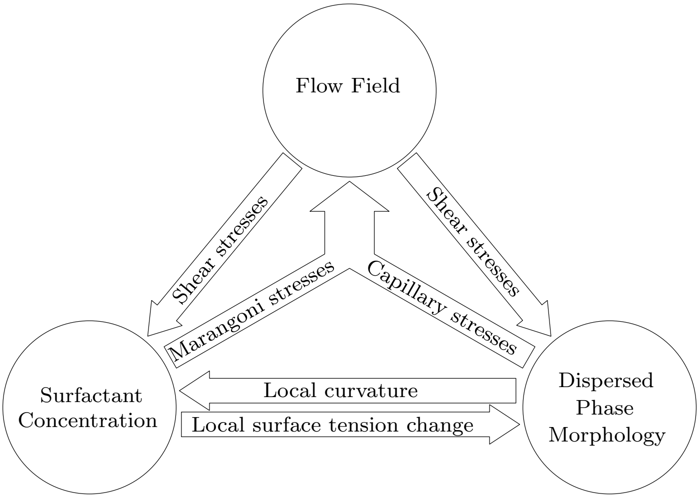

Contents

1

Introduction

Multiphase flows are common in our everyday life: they are of crucial importance in a large number of industrial applications and environmental phenomena. For instance, multiphase flows are often found in pharmaceutical [85], power [65] and process [156, 133] engineering (mixers, separators, boilers, heat exchangers, etc.), in micro-fluidic devices [28] and environmental [173] and physiological processes [41]. All of these systems involve liquid-liquid or gas-liquid mixtures characterized, in most of the cases, by the presence of an additional element (as an additive or as an impurity). When this additional element locally modifies the surface tension of the interface between the phases (liquid and/or gas), it is referred to as surfactant (surface active agent). Surfactants are amphiphilic molecules composed of a polar head and non-polar tails; due to this particular configuration, surfactant molecules are most likely found at the interface between the phases, where they arrange exposing their polar head towards the polar phase and the non-polar tails towards the other phase. The main effect introduced by a surfactant is a local modification of the surface tension of the interface; the magnitude of this modification depends on the local concentration of surfactant. A local modification of the surface tension introduces, however, an additional factor: Marangoni stresses. These stresses, tangential to the interface, are proportional to the surface tension gradients; clearly, the presence of a surfactant, locally modifying the surface tension value, can generate Marangoni stresses [68]. Surfactants, even at extremely low concentrations, can strongly influence the dynamics of the multiphase system [32, 151]; the aim of this work is to better understand the complex physics underlying surfactant-laden multiphase flows. The accurate physical insights will be useful in the control, improvement and optimization of many industrial processes and natural phenomena.

As the dynamics of surfactant-laden multiphase flows will be investigated via numerical simulations, first the numerical framework that will be adopted must be defined. Multiphase flows are characterized by physics acting at many different scales: from the molecular scale of the interface up to the largest scales of the problem. The smallest length scale (molecular scale of the interface) is of the orders of few nanometers, while the largest scale can be of the order of tenths of meters for industrial setups or even larger (tens of meters) for natural phenomena, thus spanning eight or more orders of magnitude. Resolving all these scales is however impossible, even with the help of the most modern supercomputing resources currently available, which can handle a length scale separation of about three to four orders of magnitude. Thus, the small interfacial scales cannot be resolved and must be accounted for through assumptions and numerical models. Several numerical methods have been developed to overcome the multi-scale aspects of multiphase flows. Broadly speaking, these numerical methods can be categorized, based on the approach adopted to describe the interface, in interface tracking and interface capturing methods.

The formers, interface tracking methods, rely on the advection of a set of Lagrangian markers, which define the instantaneous position of the interface. Among these methods, the Front Tracking method has been used for the simulation of droplets and bubbles in turbulence [102], and has been recently extended to model surfactant-laden droplets [105] and topology changes of the interface [103]. Indeed, interface tracking methods need closure models to describe interface interactions and topological changes (as for instance collision, breakage and coalescence) [158] and complex re-meshing algorithms to properly describe the interface morphology upon stretching, breakage and coalescence.

On the other hand, interface capturing methods use a Eulerian concentration field to describe the instantaneous distribution of the various phases; the interface is defined as an iso-level of this concentration field. Among interface capturing method, there are the Volume of Fluid [62], the Level Set [49], the Lattice Boltzmann [58, 138] and the Phase Field method [3, 69]. The chapter dedicated to the methodology, Chap. 2, will briefly review some of these approaches; for a more complete review, the reader is referred to Elghobashi [46] for a general review on numerical methods for multiphase flows, to Scardovelli and Zaleski [136] for the Volume of Fluid methods, to Gibou et al. [52] for the Level Set methods and to Chen and Doolen [27] for the Lattice Boltzmann methods.

While there is plenty of methods for the description of multiphase flows, fewer methods have been developed for multiphase flows involving surface active agents and even fewer works considered a surfactant-laden turbulent multiphase flow [105, 142]. Indeed, the description of a surfactant and of its effects on the multiphase flow adds further complexity to an already challenging problem: an additional variable, the surfactant concentration, has to be computed over a deformable, topologically changing and ever moving interface, considering also eventual exchanges among the interface and the bulk of the phases (adsorption/desorption phenomena). In recent years several numerical methods have been extended to consider the effect introduced by a surfactant; among these there are the Front Tracking [105, 112], the Immersed Boundary [88, 89], the Volume of Fluid [70, 126], the Level Set [122, 174, 175], the Lattice Boltzmann [48, 98] and the Phase Field method [47, 82, 145].

In this work a two-order-parameter formulation of the Phase Field method for the simulation of surfactant-laden multiphase flows is developed based on the original formulation proposed by Engblom et al. [47] and including further improvements by Yun et al. [184]. With respect to previous works, the range of validity of the method is also widened: the original method was limited to low surfactant concentrations, while here this limitation is removed and surfactant saturation dynamics are included. This novel numerical approach is employed to simulate the dynamics of a soluble surfactant over a deformable and topologically-changing interface. At first, simpler simulation setups are adopted to investigate and better highlight the effects of a dissolved surfactant; taking these preliminary simulations as a starting ground, the surfactant effects have been characterized in more complex setups involving turbulence, strong deformations and topological modifications of the interface. In Chap. 6 the limitations and prospects of the capabilities of current numerical methods for multiphase flows in simulating topological modifications of the interface (i.e. coalescence and breakage phenomena) are reviewed, giving an important insight on what numerical simulations can tell us about the real physics underlying these phenomena.

Thesis outline

- **Chap. 2: Methodology**
  The governing equations that define the dynamics of a surfactant-laden multiphase flows are introduced: the two-order-parameter formulation of the Phase Field method and the coupling with the momentum equations (Navier-Stokes equations) are presented in this chapter. The discretization, the numerical method and its implementation are also reported. In the last part the performances of the numerical implementation are investigated and the validation benchmarks are presented.

- **Chap. 3: Mass-conservation-improved Phase Field Methods**
  An improvement to the classic phase field method is presented. This modified formulation circumvents some of the drawbacks of the phase field method, in particular reducing shrinkage and coarsening and improving the representation of thermo-physical properties and the calculation of surface forces. Numerical simulations are performed to test the capabilities of the method.

- **Chap. 4: Comparison of 2D *vs* 3D droplet deformation**
  The effect of problem dimensionality on the deformation of a surfactant-laden droplet is investigated: the steady-state deformation and the surfactant distribution are analyzed for a circular (2D) and a spherical (3D) droplet in laminar shear flow. The deformation is also compared with the theoretical solution.

- **Chap. 5: Surfactant effects on binary droplet interactions**
  The effects of a soluble surfactant on binary droplet interactions are investigated, for different surfactant strengths and total concentrations. The increased deformability and the stresses tangential to the interface (Marangoni stresses) prevent coalescence for high surfactant concentrations and/or strong surfactants.

- **Chap. 6: Breakage, coalescence and droplet size distribution**
  The dynamics of a large swarm of deformable, surfactant-laden droplets are investigated, particularly focusing on the morphology of the dispersed phase. The surfactant effects on the dynamics of the droplets are investigated and the final droplet size distribution is computed and compared with theoretical scaling, experimental measurements and numerical results.

2

Methodology

Reproduced in part from:

G. Soligo, A. Roccon, and A. Soldati, *Coalescence of surfactant-laden drops by Phase Field Method*, Journal of Computational Physics 376:1292–1311, 2019,

and

G. Soligo, A. Roccon, and A. Soldati, *Mass-conservation-improved phase field methods for turbulent multiphase flow simulation*, Acta Mechanica 230:683–696, 2019.

The most commonly used approaches for the description of multiphase flows will be briefly reviewed throughout the first section, Sect. 2.1, particularly focusing on the method chosen, the Phase Field (PF) method. The following section, Sect. 2.2, is devoted to the presentation of a two-order-parameter phase field method [47, 145, 184] capable of describing the dynamics of a soluble surfactant. The presence of a moving and deformable interface and of a dissolved surfactant affects the surrounding flow field: the coupling among flow field, interface and surfactant is described in Sect. 2.3. Once all the equations have been defined, all the relevant dimensionless parameters are introduced, together with the dimensional analysis, Sect. 2.4. Then, the numerical method is described in Sect. 2.5. This section covers the pseudo-spectral discretization and the solution algorithm; additional details on the Fortran 2003/2008 code that has been purposely developed are given in Sect. 2.6. Finally, the last section, Sect. 2.7, presents the validation benchmarks used to test the code. In particular, the deformation of a droplet in laminar shear flow and the Rayleigh-Taylor instability are used as validation tools.

2.1 Interface modelling

This section introduces some among the most widespread approaches adopted in the description of multiphase flows. These approaches can be split in two categories: interface tracking and interface capturing methods. The former adopt a set of marker points, which identify the position of the interface (explicit definition of the interface). The latter methods rely instead on a marker function; the interface corresponds to a specific iso-level of this function (implicit definition of the interface). The main feature differentiating these methods is indeed the definition of the interface: interface tracking methods explicitly track the interface through the advection of a set of marker points, while interface capturing ones use a marker function (representing, for example, the concentration of one of the phases) to define the local distribution of each phase and the interface is identified as a particular value of this function.

2.1.1 Front Tracking

The Front Tracking (FT) method [15, 158, 161] is the most popular among the interface tracking methods. A set of Lagrangian marker points defines the interface position and shape; each of these points is advected by the local flow field.

$$\frac{\partial \mathbf{x}^i}{\partial t} = \mathbf{u}^i \tag{2.1}$$

The position of the i-th marker point, $\mathbf{x}^i$, is updated according to the local flow velocity, $\mathbf{u}^i$, which is interpolated from the flow field computational grid to the marker point position. The interface is then reconstructed by linking together this set of points. Once the interface shape has been computed, the interface curvature and, thus, interfacial forces can be calculated. These forces act at the marker point position and have to be redistributed on the Eulerian grid on which the flow field is solved (smoothing operation). This method thus requires continuous interpolation between the two grids: from the Eulerian (flow field) grid to the Lagrangian marker points to get the advection velocity and from the Lagrangian marker points to the Eulerian grid to obtain the distributed interfacial forces. The main drawbacks of the Front Tracking method are the low accuracy in the interface curvature computation from the Lagrangian marker points and the need for additional models to describe interface topological changes, as coalescences or breakages of the interface.

2.1.2 Volume of Fluid

The Volume of Fluid (VoF) [62] method belongs to the interface capturing methods. An Eulerian marker function, f, defined in the entire domain defines the concentration of one of the phases. This Eulerian marker function is advected by the flow field:

$$\frac{\partial f}{\partial t} + \mathbf{u} \cdot \nabla f = 0 \; . \tag{2.2}$$

The cell value, f_i, of the local concentration is the volume average of the concentration over the computational cell:

$$f_i = \frac{1}{V_i} \int_v f(\mathbf{x}) \mathrm{d}V \; . \tag{2.3}$$

The local marker function is initialized as a Heaviside function; to avoid numerical diffusion of the marker function over time, specific advection algorithms must be adopted [123]. The volume-averaged value in the neighbouring computational cells is used to reconstruct the shape of the interface front, thus avoiding numerical diffusion problems. Interface topological changes (coalescence and breakup) are implicitly handled by the volume-averaged marker function. It must be noted that this volume-averaged marker function, f_i, does not give an exact representation of the interface, which must be reconstructed (using for example a PLIC algorithm [127, 178]). Coalescence and breakage of the interface thus may not be properly resolved [42]. The main advantage of the Volume of Fluid method is the exact mass conservation of each phase.

2.1.3 Level Set

The Level Set (LS) method [115, 116] is another of the interface capturing methods, which is gaining an increasing popularity as a viable alternative to the VoF method. The interface is identified as the zero-level of a smooth function, ϕ; an advection equation determines the evolution of the interface.

$$\frac{\partial \phi}{\partial t} + \mathbf{u} \cdot \nabla \phi = 0 \tag{2.4}$$

In the original formulation ϕ is defined as the signed distance from the interface; due to numerical diffusion the marker function may lose its signed distance property. A reinitialization operation may be performed to restore the marker function profile: the iso-level $\phi = 0$ (interface) is kept fixed and the marker function is reinitialized to be the signed distance from the interface. This reinitialization procedure leads to mass leakages among the two phases. To reduce mass leakages the Level Set method is often coupled with a VoF approach [109] or different marker functions are used instead of the signed distance from the interface (conservative Level Set [38]). As for the VoF, the Level Set method is capable of handling merging and breakage of the interface without the need for any additional model. In addition, interface topological changes are accurately captured as the interface is exactly identified as the zero-level of a smooth function. It must be noted, however, that merging and breakage of the interface are not based on physical considerations, but on the local grid resolution. The computation of the curvature and, thus, of interfacial forces is extremely accurate, as it is based on the gradients of the smooth marker function.

2.1.4 Phase Field method

The Phase Field (PF) method [16, 17, 18] belongs to the interface capturing methods. This method was initially developed to model the microstructure dynamics of alloys during spinodal decomposition. Later on, the method has been generalized to the study of incompressible multiphase flow [3, 69] by adding an advection term and coupling the description of the interface to the Navier-Stokes equations. A marker function, ϕ, defines the dynamics of the interface; this function (order parameter) is usually referred to as phase field. The phase field corresponds to the local concentration of one of the phases; this variable changes smoothly across the interface (finite thickness interface). A Cahn-Hilliard equation describes the transport of the order parameter:

$$\frac{\partial \phi}{\partial t} + \mathbf{u} \cdot \nabla \phi = \nabla \cdot \left(\mathcal{M}_\phi \nabla \mu_\phi \right) \ . \tag{2.5}$$

With respect to the original Cahn-Hilliard equation, an advection term has been included ($\mathbf{u}$ is the velocity field). The diffusive term on the right hand side is the flux of the chemical potential gradient, with $\mathcal{M}_\phi$ being the mobility (Onsager) coefficient (relaxation time of the interface) and μ_ϕ the phase field chemical potential. Here, the mobility coefficient is set constant [8]. The chemical potential is obtained as the variational derivative of a Ginzburg-Landau free energy functional $\mathcal{F}[\phi, \nabla\phi]$ [8, 69]:

$$\mu_\phi = \frac{\delta \mathcal{F}[\phi, \nabla\phi]}{\delta\phi} \ . \tag{2.6}$$

When considering a mixture of two immiscible fluids, the free energy functional is the sum of two contributions, the first one accounting for the system bulk free energy (f_0), while the second one for the mixing free energy (f_i). The bulk free energy describes the tendency of the system to separate in two pure (stable) phases; the mixing free energy considers the energy stored within the interfacial layer, which, for a fluid-fluid system, corresponds to the surface tension.

$$\mathcal{F}[\phi, \nabla\phi] = \int_\Omega [f_0(\phi) + f_i(\nabla\phi)]\mathrm{d}\Omega \tag{2.7}$$

The first term, f_0, is a double well potential, Fig. 2.1(a), with the two minima corresponding to the pure phases, $\phi = \pm\sqrt{\beta/\alpha}$.

$$f_0(\phi) = \frac{\alpha}{4}\left(\phi - \sqrt{\frac{\beta}{\alpha}}\right)^2 \left(\phi + \sqrt{\frac{\beta}{\alpha}}\right)^2 \tag{2.8}$$

The parameters α and β are positive constant corresponding to the bulk properties of the fluids. The mixing term, Fig. 2.1(b) is proportional to the gradient of the marker function, which is maximum at the interface and zero in the bulk of the phases.

$$f_i(\nabla\phi) = \frac{\kappa}{2}|\nabla\phi|^2 \tag{2.9}$$

The positive constant κ defines the magnitude of surface tension. The chemical potential, obtained by taking the variational derivative of the free energy functional, is:

$$\mu_\phi = \frac{\delta \mathcal{F}[\phi, \nabla\phi]}{\delta\phi} = \alpha\phi^3 - \beta\phi - \kappa\nabla^2\phi \ . \tag{2.10}$$

From the chemical potential the phase field equilibrium profile can be derived: at the equilibrium the chemical potential is constant in the entire domain, $\nabla\mu_\phi = 0$. Imposing a constant phase field chemical potential throughout the entire domain, the equilibrium profile for a flat interface (Fig. 2.3) results in:

$$\phi = \sqrt{\frac{\beta}{\alpha}} \tanh\left(\frac{s}{\sqrt{2}\xi}\right) \ , \tag{2.11}$$

with $\xi = \sqrt{k/\beta}$ being a measure of the interfacial layer thickness, $\sqrt{\beta/\alpha}$ the absolute value of the phase field in the bulk of the phases and s a coordinate normal to the interface. From the equilibrium solution it can be seen how the phase field is constant in the bulk of the phases ($s \to \pm\infty$) and it undergoes a smooth transition following a

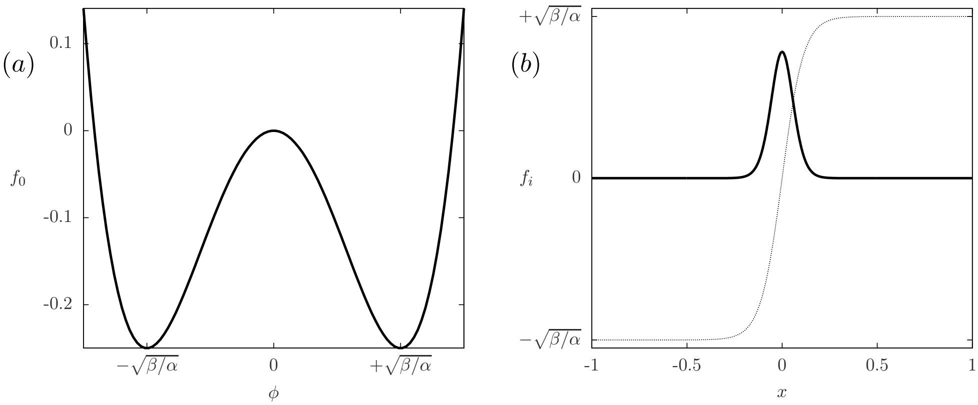

FIGURE 2.1 – Panel (a): double well potential, f_0. Panel (b): mixing free energy, f_i; the interface has been marked for reference with a thin dotted line.

hyperbolic tangent profile across the interface, whose thickness is proportional to the parameter ξ.

The main advantages of the phase field method include the implicit handling of topological changes at the interface (coalescences and breakages) and the accurate description of the interface and calculation of the interfacial curvature. Thanks to the chemical potential diffusive fluxes, reinitialization of the interface is not needed (as for the LS method): specific advection schemes are not necessary to keep the marker function profile. The main drawbacks of the phase field method are shrinkage, coarsening and misrepresentation of surface forces and thermo-physical properties. As for the Level Set method, also the phase field method suffers of mass leakages among the phases (shrinkage): when a double well potential is adopted together with a constant mobility, the phase field deviates from its equilibrium profile and the phase enclosed by the interface diffuses in the other phase to restore the equilibrium profile [39, 182]. Shrinkage could be avoided by adopting a non-constant mobility and a different bulk free energy functional (for example a logarithmic bulk free energy functional); this choice would however introduce severe numerical difficulties (including singularities in the free energy functional) in the solution of the equation, also reducing the stability of the numerical method. For these reasons a constant mobility together with a double well potential are usually preferred. The energy minimization criterion on which the method is based introduces coarsening phenomena: larger domains of one phase grow at the expense of smaller domains of the same phase to reduce the system interfacial energy. The last drawback, misrepresentation of surface forces and thermo-physical properties, originates from the deviation of the phase field from its equilibrium profile: overshoots and undershoots of the phase field may generate unphysical values of surface tension forces and negative values of the thermo-physical properties. Thermo-physical properties (density and viscosity) are assumed to be a function of the phase field, thus undershoots and overshoots of the phase field could lead to negative/unphysical values of these properties. Further details on the treatment of non-matched thermo-physical properties among the phases are reported in Sect. 2.3.1. The following section addresses the problem of shrinkage, coarsening and misrepresentation of surface forces and thermo-physical properties: a profile-corrected [11, 96, 144] and a flux-corrected [185] phase field formulations are introduced to limit these drawbacks.

Mass-conservation-improved phase field methods

Corrected formulations of the original phase field method have been proposed [11, 96, 185] to overcome the method drawbacks, namely shrinkage, coarsening and misrepresentation of surface tension forces and thermo-physical properties. The original phase field method formulation for incompressible multiphase flows [3, 69] from now on will be referred to as classic formulation. The two proposed corrections will be briefly reviewed in the following part of this section; further details on these formulations and on their performances are reported in Chap. 3.

Shrinkage and misrepresentation of surface forces and thermo-physical properties originate from the same issue: an out-of-equilibrium interfacial profile. To restore the equilibrium profile, the phase enclosed by the interface diffuses into the other phase, leading to mass leakages among the phases (shrinkage). In addition, as surface tension forces and thermo-physical properties are calculated from the phase field, an out-of-equilibrium interfacial profile introduces inaccuracies. Surface tension forces are defined to match the exact surface tension of the sharp interface model [8, 69, 76, 77, 79, 179]: the integral of the system free energy density across the interface must be equal to the surface tension, σ.

$$\sigma = \frac{\beta\kappa}{\alpha} \int_{-\infty}^{+\infty} \mathcal{F}[\phi, \nabla\phi] \mathrm{d}x \tag{2.12}$$

The equilibrium profile, which minimizes the free energy, is used in the integration:

$$\sigma = \frac{2\sqrt{2}}{3} \frac{\beta\kappa}{\alpha\xi} = \frac{2\sqrt{2}}{3} \frac{\sqrt{\beta^3\kappa}}{\alpha} \ . \tag{2.13}$$

Clearly, if the interfacial profile is perturbed from its equilibrium, the correct surface tension, and thus surface tension forces, cannot be recovered. On the other hand, thermo-physical properties are a function of the phase field variable; overshoots and undershoots with respect to bulk values introduce inaccuracies in the calculation of the thermo-physical properties or even unphysical values (e.g. a negative density or viscosity). The profile-corrected formulation introduces a penalty flux that forces the interfacial profile towards its equilibrium profile; this penalty flux is proportional to the magnitude of the perturbation from the equilibrium.

The flux-corrected phase field model builds on the profile-corrected formulation: in addition to the profile-correction penalty flux, the component normal to the interface of the chemical potential gradient is cancelled out. This way, no diffusive fluxes normal to the interface appear, preventing shrinkage and coarsening.

2.2 Surfactant

The dynamics of a soluble surfactant is described using a modified phase field method [47, 145, 184], which considers the transport of surfactant over the interface and surfactant exchanges among the interface and the bulk phases or among different interfaces. The surfactant distribution is described by the variable ψ, which is the local surfactant concentration; this variable can span from 0 (absence of surfactant) up to 1 (maximum concentration). The original single-order-parameter Ginzburg-Landau free energy functional has been modified in a two-order-parameter free energy functional to consider also surfactant dynamics: the first order parameter is the phase field, while the second one is the surfactant concentration.

$$\mathcal{F}[\phi, \nabla\phi, \psi] = \int_{\Omega} [f_0 + f_i + f_\psi + f_1 + f_{E_x}] \mathrm{d}\Omega \tag{2.14}$$

The first two terms, f_0 and f_i, are the same for the single-order-parameter formulation, Eq. (2.8) and Eq. (2.9). The latter three terms account for the presence of a dissolved surfactant. The term f_ψ, Fig. 2.2(a), is an entropy term: it defines the entropy decrease obtained when the surfactant is uniformly distributed in the entire domain Ω.

$$f_\psi = \kappa T[\psi \log \psi + (1-\psi)\log(1-\psi)] \tag{2.15}$$

T is the absolute temperature, while κ is the same positive constant defined for the single-order-parameter free energy functional defining the surface tension magnitude. The dimensionless parameter Pi can be defined as $Pi = \kappa T \alpha / \beta^2$. The entropy term thus becomes:

$$f_\psi = \frac{\beta^2}{\alpha} Pi[\psi \log \psi + (1-\psi)\log(1-\psi)] \ . \tag{2.16}$$

This term strictly limits the possible values assumed by the surfactant concentration between the lower bound, $\psi = 0$ (absence of surfactant), and the upper bound, $\psi = 1$ (maximum concentration). The temperature-dependent parameter Pi defines surfactant diffusivity: a higher value of Pi increases surfactant diffusion, thus a uniform surfactant distribution in the entire domain is favoured. The terms f_1 and f_{E_x}, Fig. 2.2(b), describe the amphiphilic character of surfactant molecules: due to their particular configuration (hydrophilic head and hydrophobic tail), surfactant molecules naturally gather at the interface between two fluids, minimizing the system configuration energy. In particular f_1 describes the adsorption of surfactant at the interface; in the original formulation [91, 164] this term is proportional to $(\nabla\phi)^2$. Engblom et al. [47] showed that this term can be replaced by a polynomial one, so that the range of parameters in which the problem is well-posed is widened.

$$f_1 = -\frac{\alpha}{2}\psi\left(\frac{\beta}{\alpha} - \phi^2\right)^2 \tag{2.17}$$

This term is active at the interface where the gradients of the phase field are non-zero; this behaviour is properly captured by the polynomial approximation as f_1 is zero in the bulk of the phases, which correspond to $\phi = \pm\sqrt{\beta/\alpha}$. The last term, f_{E_x}, penalizes the presence of surfactant in the bulk of the phases (cost of free surfactant), thus favoring its adsorption at the interface.

$$f_{E_x} = \frac{W}{2}\psi\phi^2 \tag{2.18}$$

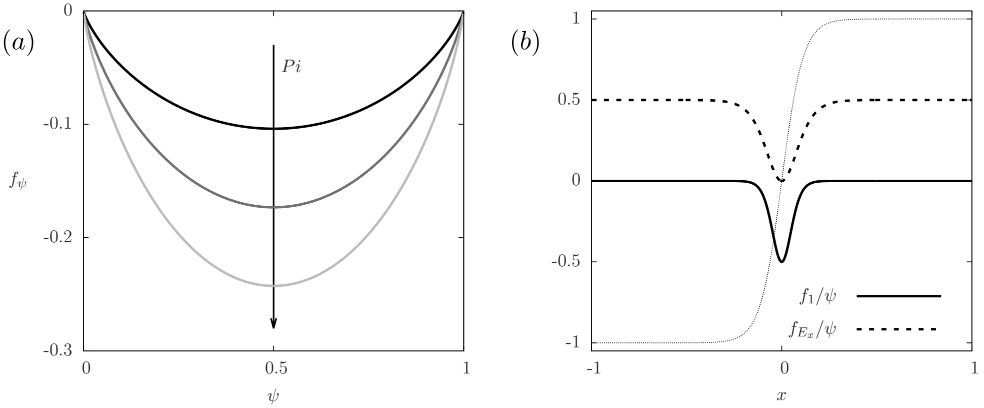

FIGURE 2.2 – Panel (*a*): entropy term f_ψ for different values of the surfactant diffusivity, Pi. Panel (*b*): for ease of visualization the terms f_1 and f_{E_x} have been divided by the surfactant concentration, ψ. The interface has been marked with a thin dotted line.

The parameter W defines the surfactant solubility in the bulk. f_{E_x} has a minimum at the interface ($\phi \sim 0$) and is positive in the bulk of the phases. Once defined all the terms of the two-order-parameter free energy functional, the chemical potentials of the phase field, μ_ϕ, and of the surfactant, μ_ψ, can be calculated:

$$\mu_\phi = \frac{\delta \mathcal{F}}{\delta \phi} = \alpha\phi^3 - \beta\phi - \kappa\nabla^2\phi + \overbrace{2\alpha\psi\phi\left(\frac{\beta}{\alpha} - \phi^2\right) + W\phi\psi}^{C_{\phi\psi}} \, , \tag{2.19}$$

$$\mu_\psi = \frac{\delta \mathcal{F}}{\delta \psi} = \frac{\beta^2}{\alpha} Pi \log\left(\frac{\psi}{1-\psi}\right) - \frac{\alpha}{2}\left(\frac{\beta}{\alpha} - \phi^2\right)^2 + \frac{W}{2}\phi^2 \, . \tag{2.20}$$

The dynamics of the phase field is controlled by the phase field chemical potential, Eq. (2.19). The phase field chemical potential depends also on the surfactant concentration (terms collected in $C_{\phi\psi}$); this dependence induces an unphysical behaviour of the interface [184]. According to Yun et al. [184], this term has to be neglected in the phase field chemical potential to restore the correct interfacial behaviour. From the two chemical potentials the equilibrium profile for both the phase field and the surfactant concentration can be obtained. As the phase field chemical potential is unchanged, the phase field equilibrium profile of the single-order-parameter formulation is maintained, Eq. (2.11). At equilibrium conditions the chemical potential is constant in the entire domain. In the bulk of the phases ($\phi = \pm\sqrt{\beta/\alpha}$) the surfactant chemical potential is:

$$\mu_{\psi,b} = \frac{\beta^2}{\alpha} Pi \log\left(\frac{\psi_b}{1-\psi_b}\right) + \frac{W}{2}\frac{\beta}{\alpha} \, , \tag{2.21}$$

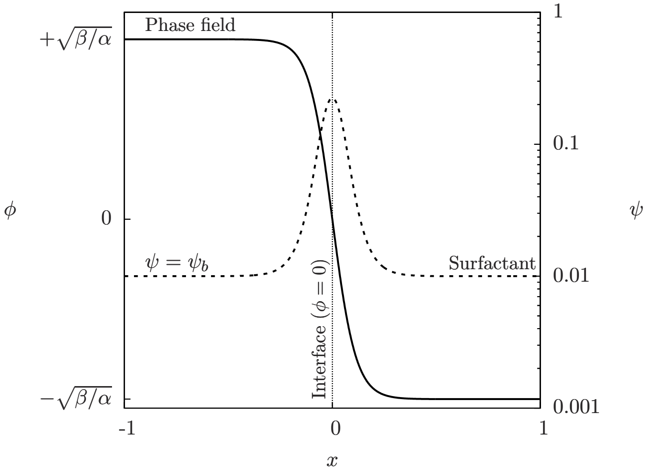

FIGURE 2.3 – Phase field and surfactant equilibrium profiles. The phase field is uniform in the bulk of the phases, $\phi = \pm\sqrt{\beta/\alpha}$, and it undergoes a smooth transition at the interface. The equilibrium surfactant concentration is equal to the surfactant bulk concentration, ψ_b, in the bulk of the phases and reaches its maximum at the interface.

with ψ_b being the surfactant bulk concentration. As the chemical potential at equilibrium is constant, we have $\mu_\psi = \mu_{\psi,b}$. From this condition we obtain:

$$\frac{\psi_b}{1-\psi_b}\frac{1-\psi}{\psi} = \overbrace{\exp\left\{-\frac{\alpha}{2\beta^2 Pi}\left(\frac{\beta}{\alpha}-\phi^2\right)\left[\alpha\left(\frac{\beta}{\alpha}-\phi^2\right)+W\right]\right\}}^{\psi_c} . \tag{2.22}$$

The auxiliary variable ψ_c is a function of the phase field solely. The final surfactant equilibrium profile results in:

$$\psi = \frac{\psi_b}{\psi_b + \psi_c(1-\psi_b)} . \tag{2.23}$$

The phase field and the surfactant equilibrium profiles are displayed in Fig. 2.3. Once the chemical potential for the surfactant has been defined, a second Cahn-Hilliard-like equation, which describes the surfactant dynamics can be obtained:

$$\frac{\partial \psi}{\partial t} + \mathbf{u}\cdot\nabla\psi = \nabla\cdot\left(\mathcal{M}_\psi \nabla\mu_\psi\right) . \tag{2.24}$$

The surfactant mobility coefficient (Onsager coefficient) is a function of the surfactant concentration: $\mathcal{M}_\psi = m_\psi \psi(1-\psi)$.

2.2.1 Calculation of surface forces

Surfactants (surface active agents) locally reduce surface tension with respect to a clean (surfactant-free) interface. The surface tension reduction depends on the local surfactant concentration: a lower surface tension can be obtained with a higher surfactant

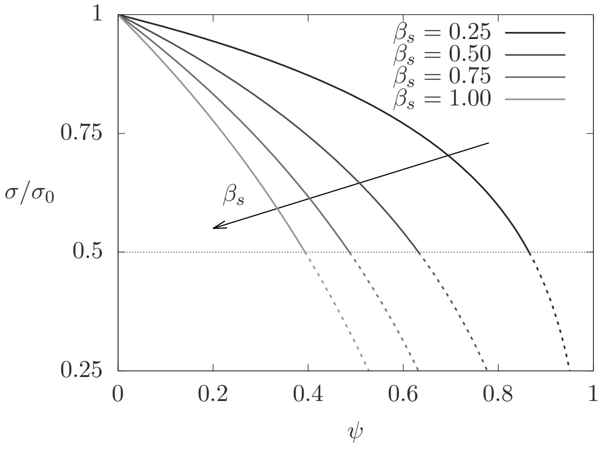

FIGURE 2.4 – Langmuir equation of state for different values of the elasticity number β_s; the thick dashed lines show the equation of state beyond its range of validity, marked with the thin dotted line. A higher elasticity number leads to a stronger surface tension reduction.

concentration. Surface tension, thus, varies with the local surfactant concentration and can be non-homogeneous over the interface (non-homogenous surfactant concentration). In turn, surface tension gradients generate Marangoni stresses; these stresses are directed as the surface tension gradients (thus opposite to surfactant gradients) and are tangential to the interface.

The surface tension reduction operated by the surfactant is quantified using a Langmuir equation of state (Szyszkowski equation, Fig. 2.4) [10, 118]:

$$\sigma(\psi) = \sigma_0 \left[1 + \beta_s \log(1 - \psi)\right] \ , \tag{2.25}$$

where σ_0 is the clean interface surface tension and β_s is the elasticity number, which characterizes the strength of the surfactant. The surface tension reduction is proportional to the elasticity number: the higher the elasticity number is, the stronger the surface tension reduction will be. This equation of state is valid in the limit of low to moderate surfactant concentration. Experimental works [21, 71, 100, 149] showed that surface tension never decreases below about half of its clean interface value; this limit is not captured by the Langmuir equation of state, which has then been modified to extend its range of validity:

$$\sigma(\psi) = \sigma_0 \max\left[1 + \beta_s \log(1 - \psi), 0.5\right] \ . \tag{2.26}$$

With this modification, the equation of state better follows experimental observations and unphysical values of surface tension are avoided. The physical mechanism that limits the minimum surface tension traces back to the local saturation of surfactant: due to the finite-size of surfactant molecules, the maximum surfactant concentration is limited. The saturation concentration is also known as critical micelle concentration, as surfactant molecules, once reached the saturation concentration, start forming aggregates (micelles) made of surfactant molecules alone. Large-scale numerical simulations, however, cannot capture these molecular-scale phenomena: indeed, numerical simulations can cover a limited range of length scales (about three to four orders of magnitude). This limitation originates from the available computational power: the computational cost grows as the range of resolved scales is increased (this issue will be extensively addressed in Chap. 6). The usual choice of resolved scales ranges from the macroscopic flow (larger scales) down to the smallest structures of the flow (smaller scales, order of Kolmogorov length scale). Thus, all phenomena occurring at even smaller scales (as for instance, at the molecular scale) are modelled on a larger, resolved scale. For this reason, the numerical simulations presented here do not directly simulate the formation of micelles, which in addition would be too small to affect the macroscopic dynamics of the multiphase flow system. However, the effect of the surfactant saturation limit is still considered in the model: surface tension keeps constant when the surfactant exceeds the saturation limit. As the molecular-scale dynamics of the surfactant molecules and of the micelles formation are not directly simulated, in the following the surfactant saturation concentration is referred to as shutdown concentration instead of critical micelle concentration.

2.3 Flow field

Continuity and Navier-Stokes equations describe the dynamics of the turbulent flow. The presence of moving and deformable interfaces and of a dissolved surfactant is accounted for in the Navier-Stokes equations with an interfacial term, which indeed couples the Navier-Stokes equations to the two Cahn-Hilliard equations (one for the phase field and one for the surfactant concentration). In the following the most general formulation of the Navier-Stokes and continuity equations will be introduced: the two phases can have different thermo-physical properties, in particular density [40] and viscosity [128]. Density and viscosity depend on the local concentration of each phase; further details are reported in Sect. 2.3.1. The mass conservation (continuity equation) for incompressible flows results in a divergence-free flow:

$$\nabla \cdot \mathbf{u} = 0 \; . \tag{2.27}$$

The velocity field is divergence-free also when phases with different densities are considered: imposing the conservation of volume at the interface, the volume diffusive fluxes of the two species cancel out, resulting in a divergence-free field [40]. The mass conservation of the two incompressible phases are:

$$\frac{\partial(\rho_1 C)}{\partial t} + \nabla \cdot (\rho_1 C\mathbf{u} - \rho_1 \mathbf{j}_1) = 0 \; , \tag{2.28}$$

$$\frac{\partial[\rho_2(1-C)]}{\partial t} + \nabla \cdot [\rho_2(1-C)\mathbf{u} - \rho_2 \mathbf{j}_2] = 0 \; , \tag{2.29}$$

where $C = (\phi + 1)/2$ is the local concentration of phase 1 (characterized by the subscript 1, while the subscript 2 stands for the other phase) and $\mathbf{j_1}$, $\mathbf{j}_2$ are the diffusive volume fluxes (volume diffusive flow rates) present at the interface. As both phases are incompressible, their density is constant.

$$\frac{\partial C}{\partial t} + \nabla \cdot (C\mathbf{u} - \mathbf{j}_1) = 0 \; , \tag{2.30}$$

$$\frac{\partial(1-C)}{\partial t} + \nabla \cdot [(1-C)\mathbf{u} - \mathbf{j}_2] = 0 \; . \tag{2.31}$$

Summing the latter two equations we obtain:

$$\nabla \cdot \mathbf{u} = \nabla \cdot (\mathbf{j}_1 + \mathbf{j}_2) \; . \tag{2.32}$$

Imposing the conservation of volume at the interface constrains the two diffusive fluxes to $\mathbf{j}_1 = -\mathbf{j}_2$, thus resulting in a divergence-free velocity field.

The Navier-Stokes equations (momentum conservation) for a divergence-free velocity field is:

$$\rho(\phi)\left(\frac{\partial \mathbf{u}}{\partial t} + \mathbf{u} \cdot \nabla \mathbf{u}\right) = -\nabla p + \nabla \cdot \left[\eta(\phi)(\nabla \mathbf{u} + \nabla \mathbf{u}^T)\right] + \rho(\phi)\mathbf{g} + \nabla \cdot [\overline{\tau}_c \kappa f_\sigma(\psi)] \; , \tag{2.33}$$

with $\mathbf{u} = (u, v, w)$ being the velocity field, t time, ∇p the pressure gradient, $\rho(\phi)$ and $\eta(\phi)$ respectively the local density and dynamic viscosity, $\mathbf{g}$ the gravity acceleration, $\overline{\tau}_c$ the Korteweg tensor [83] and $f_\sigma(\psi) = \sigma(\psi)/\sigma_0$ the dimensionless surface tension equation of state.

Surface forces are calculated adopting a geometric approach: the Korteweg tensor, $\overline{\tau}_c = |\nabla\phi|^2\mathbf{I} - \nabla\phi \otimes \nabla\phi$, considers the interface shape and curvature, while the Langmuir equation of state takes into account the surface tension local value. The geometric approach was selected over the thermodynamic one, based on the chemical potentials, for mainly two reasons: (i) the effect of surfactant on surface tension is completely customizable (choice of equation of state and relative parameters), (ii) the thermodynamic approach [47, 91] cannot be easily applied as the phase field chemical potential was modified to remove the unphysical behaviour of the interface [184].

2.3.1 Treatment of non-matched properties

Thermo-physical properties are defined as a linear function of the phase field: at the interface they undergo a smooth transition following the phase field profile. This feature circumvents all the complications that could arise from jumps and discontinuities across the interface. The properties of the carrier phase are taken as reference quantities: the carrier phase density, ρ_c, and the carrier phase viscosity, η_c. The density and viscosity ratios among the two phases are respectively defined as:

$$\rho_r = \frac{\rho_d}{\rho_c} \quad , \qquad \eta_r = \frac{\eta_d}{\eta_c} \; , \tag{2.34}$$

with the subscripts d denoting the dispersed phase properties and c the carrier phase properties. Fig. 2.5 shows the profile of a generic thermo-physical property, either density or viscosity, across the interface. The interface is identified by the red dashed line, while the interfacial layer (±96% of the phase field bulk value) is marked with a light red rectangle. Two different property ratios are displayed, $\gamma_r > 1$ (solid line) and $\gamma_r < 1$ (dashed line). As the property of the carrier phase (phase field bulk value $\phi = -\sqrt{\beta/\alpha}$) are taken as a reference, the value of the dimensionless thermo-physical property is equal to one in the bulk of the carrier phase.

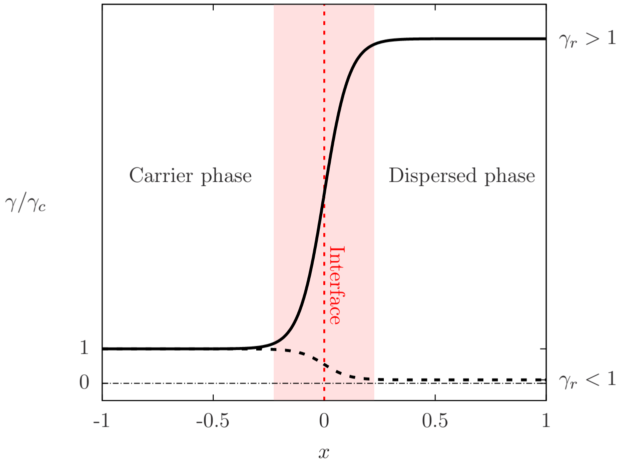

FIGURE 2.5 – Profile of a generic thermo-physical property γ across the interface (red dashed line) for two different property ratios γ_r. The carrier phase thermo-physical property γ_c is taken as reference value. The interfacial layer (light red area) identifies the region in which the phase field spans ±96% of its bulk value.

$$\rho(\phi) = \rho_c \left[1 + \frac{\rho_r - 1}{2}\left(\frac{\phi}{\sqrt{\beta/\alpha}} + 1\right)\right] \tag{2.35}$$

$$\eta(\phi) = \eta_c \left[1 + \frac{\eta_r - 1}{2}\left(\frac{\phi}{\sqrt{\beta/\alpha}} + 1\right)\right] \tag{2.36}$$

With the current definition of the thermo-physical properties as a function of the phase field, their value never reduces below zero (unphysical value for density or viscosity) if the phase field profile does not strongly overshoot/undershoot its equilibrium profile. As interactions with the surrounding (even turbulent) flow field perturb the interfacial profile, the thermo-physical properties may be misrepresented; Chap. 3 tackles this issue by introducing two corrected formulations of the phase field method tailored to circumvent the drawbacks of the method.

2.4 Dimensional analysis

All the equations presented so far are in dimensional form; the non-dimensionalizing procedure will be now introduced. Dimensionless quantities will be indicated using a superscript *. A flat channel geometry is adopted in all the simulations presented in this work, Fig. 2.6. The channel is bounded by two solid walls at $z = \pm h$, with h being the channel half height. The reference velocity depends on the problem considered: for pressure-driven flows it is the friction velocity, $u_\tau = \sqrt{\tau_w/\rho_c}$ (τ_w is the shear stress at the wall and ρ_c the reference density), while for the shear flow configuration it corresponds to the wall velocity, u_w. In the following the friction velocity, u_τ, will be used for ease of notation. From the velocity and the length scale, the time scale can

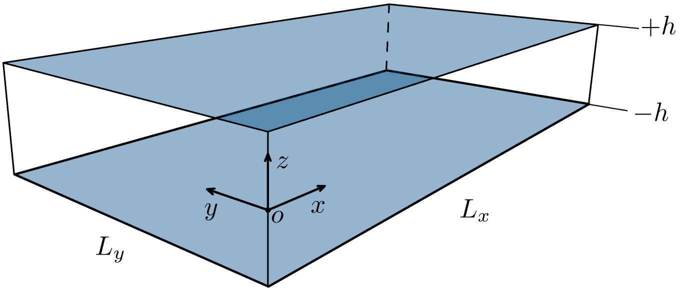

FIGURE 2.6 – Sketch of the simulation domain. The closed channel is bounded by solid walls at $z = \pm h$. The channel has dimensions L_x in the streamwise direction (x), L_y in the spanwise direction (y) and $2h$ in the wall-normal direction (z). The reference frame is centered in o, located at the channel mid-plane.

be derived:

$$\mathbf{x}^* = \frac{\mathbf{x}}{h} \quad , \qquad \mathbf{u}^* = \frac{\mathbf{u}}{u_\tau} \quad , \qquad t^* = \frac{u_\tau}{h} t \; , \tag{2.37}$$

with $\mathbf{x} = (x, y, z)$ being the position, $\mathbf{u} = (u, v, w)$ the fluid velocity and t time. The value of the phase field in the bulk of the phases, $\sqrt{\beta/\alpha}$ is used to make the phase field dimensionless.

$$\phi^* = \frac{\phi}{\sqrt{\beta/\alpha}} \tag{2.38}$$

The thermo-physical properties of the carrier fluid (subscript c) have been taken as reference quantities.

$$\rho^*(\phi^*) = \frac{\rho(\phi)}{\rho_c} = 1 + \frac{\rho_r - 1}{2}(\phi^* + 1) \tag{2.39}$$

$$\eta^*(\phi^*) = \frac{\eta(\phi)}{\eta_c} = 1 + \frac{\eta_r - 1}{2}(\phi^* + 1) \tag{2.40}$$

The dimensionless continuity equation results in:

$$\nabla \cdot \mathbf{u}^* = 0 \; . \tag{2.41}$$

The dimensionless surface force term is:

$$\frac{h}{\rho_c u_\tau^2} \nabla \cdot [\overline{\tau}_c \kappa f_\sigma(\psi)] = \frac{1}{\rho_c u_\tau^2 h} \frac{\sqrt{\kappa/\beta}}{h} \frac{\sqrt{\kappa\beta^3}}{\alpha} \nabla \cdot [\overline{\tau}_c^* f_\sigma(\psi)] \; . \tag{2.42}$$

The dimensionless Korteweg stress tensor, $\overline{\tau}_c^*$ is:

$$\overline{\tau}_c^* = |\nabla\phi^*|^2 \mathbf{I} - \nabla\phi^* \otimes \nabla\phi^* = \frac{\beta/\alpha}{h^2} \overline{\tau}_c \; . \tag{2.43}$$

Exploiting Eq. (2.13) and defining two dimensionless quantities, We and Ch, the dimensionless surface force term becomes:

$$\frac{3}{\sqrt{8}}\frac{\sigma_0}{\rho_c u_\tau^2 h}\frac{\sqrt{\kappa/\beta}}{h}\nabla\cdot\left[\overline{\tau}_c^* f_\sigma(\psi)\right] = \frac{3}{\sqrt{8}}\frac{Ch}{We}\nabla\cdot\left[\overline{\tau}_c^* f_\sigma(\psi)\right] . \tag{2.44}$$

The Cahn number, Ch, is the dimensionless interface thickness; it is defined as the ratio ξ/h. The Weber number, We, is the ratio of inertia forces over surface tension forces:

$$We = \frac{\rho_c u_\tau^2 h}{\sigma_0} , \tag{2.45}$$

where σ_0 the reference surface tension (clean interface). This dimensionless parameter, thus, does not account for any surface tension reduction operated by a dissolved surfactant. The dimensionless Navier-Stokes equation is:

$$\begin{aligned}\rho^*(\phi^*)\left(\frac{\partial\mathbf{u}^*}{\partial t^*} + \mathbf{u}^*\cdot\nabla\mathbf{u}^*\right) =& -\nabla p^* + \frac{1}{Re_\tau}\nabla\cdot\left[\eta^*(\phi^*)\left(\nabla\mathbf{u}^* + \nabla{\mathbf{u}^*}^T\right)\right] + \\ &+ \frac{1}{Fr^2}\rho^*(\phi^*)\mathbf{g}^* + \frac{3}{\sqrt{8}}\frac{Ch}{We}\nabla\cdot\left[\overline{\tau}_c^* f_\sigma(\psi)\right] .\end{aligned} \tag{2.46}$$

The dimensionless pressure is defined as $p^* = p/(\rho_c u_\tau^2)$. The shear Reynolds number, Re_τ is the ratio of inertial over viscous forces:

$$Re_\tau = \frac{\rho_c u_\tau h}{\eta_c} ; \tag{2.47}$$

it is defined using the carrier phase properties as reference quantities. The Froude number, Fr is defined as:

$$Fr = \frac{u_\tau}{\sqrt{gh}} , \tag{2.48}$$

where g is the modulo of the gravity vector and $\mathbf{g}^*$ is the gravity unit vector.
The dimensionless transport equation for the phase field is:

$$\frac{\partial\phi^*}{\partial t^*} + \mathbf{u}^*\cdot\nabla\phi^* = \frac{1}{Pe_\phi}\nabla^2\mu_\phi^* . \tag{2.49}$$

The phase field Péclet number, Pe_ϕ, is the ratio of convective over diffusive phenomena of the phase field. The dimensionless phase field equilibrium profile is $\phi^* = \tanh(s^*/\sqrt{2}Ch)$, with s^* being a dimensionless coordinate normal to the interface. The chemical potential is made dimensionless by a factor $\sqrt{\beta^3/\alpha}$.

$$\mu_\phi = \sqrt{\frac{\beta^3}{\alpha}}\mu_\phi^* = \sqrt{\frac{\beta^3}{\alpha}}\left({\phi^*}^3 - \phi^* - Ch^2\nabla^2\phi^*\right) \tag{2.50}$$

The phase field Péclet number is defined as:

$$Pe_\phi = \frac{u_\tau h}{\beta m_\phi} , \tag{2.51}$$

where m_ϕ is the constant mobility coefficient for the phase field.

The surfactant concentration is already a dimensionless quantity; its dimensionless transport equation reads:

$$\frac{\partial \psi}{\partial t^*} + \mathbf{u}^* \cdot \nabla \psi = \frac{1}{Pe_\psi} \nabla \cdot \left[\psi (1-\psi) \nabla \mu_\psi^* \right] . \tag{2.52}$$

Pe_ψ is the surfactant concentration Péclet number, representing the ratio of convective over diffusive phenomena.

$$Pe_\psi = \frac{u_\tau h \alpha}{m_\psi \beta^2} \tag{2.53}$$

The surfactant concentration chemical potential is:

$$\mu_\psi = \frac{\beta^2}{\alpha} \mu_\psi^* = \frac{\beta^2}{\alpha} \left[Pi \log \left(\frac{\psi}{1-\psi} \right) - \frac{(1-{\phi^*}^2)^2}{2} + \frac{1}{2E_x} {\phi^*}^2 \right] . \tag{2.54}$$

The dimensionless parameter $E_x = \beta / W$ defines the surfactant solubility in the bulk of the two phases.
In the following the dimensionless notation * will be dropped for ease of reading; from now on, all equations presented are however dimensionless (outer units scaling system, for the wall units scaling system the reader is referred to Appendix B). The dimensionless equations are (in order: continuity, Navier-Stokes, density, viscosity, phase field transport, surfactant concentration transport, phase field and surfactant concentration chemical potentials):

$$\nabla \cdot \mathbf{u} = 0 \; ; \tag{2.55}$$

$$\begin{aligned} \rho(\phi) \left(\frac{\partial \mathbf{u}}{\partial t} + \mathbf{u} \cdot \nabla \mathbf{u} \right) = & - \nabla p + \frac{1}{Re_\tau} \nabla \cdot \left[\eta(\phi) \left(\nabla \mathbf{u} + \nabla \mathbf{u}^T \right) \right] + \\ & + \frac{\rho(\phi) \mathbf{g}}{Fr^2} + \frac{3}{\sqrt{8}} \frac{Ch}{We} \nabla \cdot \left[\overline{\tau}_c f_\sigma(\psi) \right] ; \end{aligned} \tag{2.56}$$

$$\rho(\phi) = 1 + \frac{\rho_r - 1}{2} (\phi + 1) \; ; \tag{2.57}$$

$$\eta(\phi) = 1 + \frac{\eta_r - 1}{2} (\phi + 1) \; ; \tag{2.58}$$

$$\frac{\partial \phi}{\partial t} + \mathbf{u} \cdot \nabla \phi = \frac{1}{Pe_\phi} \nabla^2 \mu_\phi \; ; \tag{2.59}$$

$$\frac{\partial \psi}{\partial t} + \mathbf{u} \cdot \nabla \psi = \frac{1}{Pe_\psi} \nabla \cdot \left[\psi (1-\psi) \nabla \mu_\psi \right] ; \tag{2.60}$$

$$\mu_\phi = \phi^3 - \phi - Ch^2 \nabla^2 \phi \; ; \tag{2.61}$$

$$\mu_\psi = Pi \log \left(\frac{\psi}{1-\psi} \right) - \frac{(1-\phi^2)^2}{2} + \frac{1}{2E_x} \phi^2 \; . \tag{2.62}$$

The shear Reynolds number and the Weber number are phenomenological parameters, which determine the setup of the problem analyzed. The Cahn number, which sets the interface thickness with respect to the channel size, is determined based on the computational grid. First, the grid spacing and problem size are selected in order to properly resolve the flow configuration studied, then the Ch number is chosen so that there are at least five grid points across the interface (clean interface). When the surfactant is considered, this grid requirement almost doubles: at least eight grid points across the interface are needed to resolve all the steep gradients appearing at the interface. Then, the phase field Péclet number, Pe_ϕ, is set according to the scaling $Pe_\phi = 1/Ch$ [108, 144, 183].

2.5 Numerical method

The dimensionless system of equations is solved in a closed-channel configuration, with two solid walls at $z = \pm 1$, as shown in Fig. 2.6. A velocity-vorticity approach is adopted to solve the flow field: the Navier-Stokes and continuity equations are replaced by a second-order equation for the wall-normal component of the vorticity (curl of the Navier-Stokes equation), a fourth-order equation for the wall-normal component of velocity (twice the curl of the Navier-Stokes equation), the definition of the wall-normal vorticity and the continuity equation itself. With this approach time-consuming Poisson solvers for the calculation of the pressure field can be avoided. The transport equations for the phase field and for the surfactant concentration are directly solved, Eq. (2.59) and Eq. (2.60). A more compact notation is now introduced; all non-linear terms that will be time-integrated using an explicit scheme are collected in a non-linear term. The various non-linear terms are $\mathbf{S}$, S_ϕ and S_ψ, respectively for the Navier-Stokes, phase field and surfactant concentration transport equation.

$$\begin{aligned}\mathbf{S} = \begin{bmatrix} S_x \\ S_y \\ S_z \end{bmatrix} = & -\mathbf{u}\cdot\nabla\mathbf{u} - \frac{\rho_r - 1}{2}(\phi+1)\left(\frac{\partial \mathbf{u}}{\partial t} + \mathbf{u}\cdot\nabla\mathbf{u}\right) - \Pi + \\ & + \frac{1}{Re_\tau}\nabla\cdot\left[\frac{\eta_r - 1}{2}(\phi+1)\left(\nabla\mathbf{u} + \nabla\mathbf{u}^T\right)\right] + \\ & + \frac{\rho(\phi)\mathbf{g}}{Fr^2} + \frac{3}{\sqrt{8}}\frac{Ch}{We}\nabla\cdot\left[\overline{\tau}_c f_\sigma(\psi)\right]\end{aligned} \tag{2.63}$$

$$S_\phi = -\mathbf{u}\cdot\nabla\phi + \frac{1}{Pe_\phi}\left[\nabla^2\phi^3 - (1+s)\nabla^2\phi + f_c\right] \tag{2.64}$$

$$S_\psi = -\mathbf{u}\cdot\nabla\psi + \frac{1}{Pe_\psi}\nabla\cdot\left[\psi(1-\psi)\nabla\left(\frac{(1-\phi^2)^2}{2} + \frac{\phi^2}{2E_x}\right)\right] \tag{2.65}$$

The pressure gradient has been split in two components, a constant mean pressure gradient, Π, and a fluctuating component, $\nabla p'$ [143]. A splitting coefficient, s, appears in the phase field transport equation; the splitting of the Laplace operator improves the stability of the numerical scheme [8, 179]. This splitting coefficient is defined as:

$$s = \sqrt{\frac{4Pe_\phi Ch^2}{\Delta t}}\ , \tag{2.66}$$

with Δt being the integration time step. For the sake of completeness, also the contribution from the corrected phase field formulations, f_c, has been included in the phase field transport equation. In a more compact form, the complete system of equations thus results in:

$$\nabla \cdot \mathbf{u} = 0 \; ; \tag{2.67}$$

$$\frac{\partial \mathbf{u}}{\partial t} = \mathbf{S} - \nabla p' + \frac{1}{Re_\tau}\nabla^2 \mathbf{u} \; ; \tag{2.68}$$

$$\frac{\partial \phi}{\partial t} = S_\phi + \frac{s}{Pe_\phi}\nabla^2 \phi - \frac{Ch^2}{Pe_\phi}\nabla^4 \phi \; ; \tag{2.69}$$

$$\frac{\partial \psi}{\partial t} = S_\psi + \frac{Pi}{Pe_\psi}\nabla^2 \psi \; . \tag{2.70}$$

The Navier-Stokes equation is solved in a velocity-vorticity formulation. First, by taking the curl of the Navier-Stokes equation, a transport equation for the vorticity, $\boldsymbol{\omega}$ is obtained:

$$\frac{\partial \boldsymbol{\omega}}{\partial t} = \nabla \times \mathbf{S} + \frac{1}{Re_\tau}\nabla^2 \boldsymbol{\omega} \; . \tag{2.71}$$

The wall-normal component of this equation gives the wall-normal component of the vorticity vector, ω_z. Then, a fourth-order equation for the velocity can be obtained by taking the curl of Eq. (2.71) (twice the curl of the Navier-Stokes equation).

$$\frac{\partial(\nabla^2 \mathbf{u})}{\partial t} = \nabla^2 \mathbf{S} - \nabla(\nabla \cdot \mathbf{S}) + \frac{1}{Re_\tau}\nabla^4 \mathbf{u} \tag{2.72}$$

The wall-normal projection of this equation results in a fourth-order equation for the wall-normal velocity.
The final system of equations solved results in:

$$\begin{cases} \nabla \cdot \mathbf{u} = 0 \\ \boldsymbol{\omega} \cdot \mathbf{n}_z = (\nabla \times \mathbf{u}) \cdot \mathbf{n}_z \\ \dfrac{\partial(\nabla^2 \mathbf{u})}{\partial t} \cdot \mathbf{n}_z = \left[\nabla^2 \mathbf{S} - \nabla(\nabla \cdot \mathbf{S}) + \dfrac{1}{Re_\tau}\nabla^4 \mathbf{u}\right] \cdot \mathbf{n}_z \\ \dfrac{\partial \boldsymbol{\omega}}{\partial t} \cdot \mathbf{n}_z = \left(\nabla \times \mathbf{S} + \dfrac{1}{Re_\tau}\nabla^2 \boldsymbol{\omega}\right) \cdot \mathbf{n}_z \\ \dfrac{\partial \phi}{\partial t} = S_\phi + \dfrac{s}{Pe_\phi}\nabla^2 \phi - \dfrac{Ch^2}{Pe_\phi}\nabla^4 \phi \\ \dfrac{\partial \psi}{\partial t} = S_\psi + \dfrac{Pi}{Pe_\psi}\nabla^2 \psi \end{cases} \tag{2.73}$$

The symbol $\mathbf{n}_z$ represents the wall-normal direction unit vector (z axis). This dimensionless system of equations has been spatially-discretized using a pseudo-spectral approach [19, 64, 121] with Fourier discretization in the streamwise (x) and spanwise (y) directions and Chebyshev polynomials in the wall-normal (z) direction. The adoption of Fourier series in the x and y directions implicitly enforces periodic boundary conditions on all variables along these directions. All variables are Eulerian and are solved on the same computational grid; only the surfactant concentration is solved on a finer grid in order to properly resolve the steep gradients present at the interface. All the other variables are solved on the coarser grid to limit the overall computational cost. Variables are interpolated in modal space from one grid to the other by adding/removing high wavenumber modes and renormalizing the modes. A uniform grid spacing is adopted in the streamwise and spanwise directions (Fourier discretization), while in the wall-normal direction Chebyshev-Gauss-Lobatto points were chosen, thus leading to a much finer grid close to the channel walls. The points (x_i, y_j, z_k) of the Cartesian grid are defined as:

$$\begin{aligned} x_i &= (i-1)\frac{L_x}{N_x-1} && i = 1,\dots,N_x \\ y_j &= (j-1)\frac{L_y}{N_y-1} && j = 1,\dots,N_y \quad . \\ z_k &= \cos\left(\frac{k-1}{N_z-1}\pi\right) && k = 1,\dots,N_z \end{aligned} \tag{2.74}$$

The number of grid points in each direction is N_x (x direction), N_y (y direction) and N_z (z direction).

The time-advancement is performed adopting a IMplicit-EXplicit scheme (IMEX); the terms $\mathbf{S}$, S_ϕ and S_ψ are integrated explicitly with an Adams-Bashforth scheme, while the other terms implicitly. A Crank-Nicolson scheme is used to integrate the implicit terms of the second order equation for the wall-normal vorticity and of the fourth order equation for the wall-normal velocity. The implicit part of the two Cahn-Hilliard equations for the phase field and surfactant transport is integrated with an implicit Euler scheme; this choice reduces the unphysical high frequency oscillations that could arise from the steep gradients of the equations [8, 179]. At the first time step an explicit Euler scheme is used for the explicit part of all the equations. At the generic time step n (current time step) the time-discretized system of equations is:

$$\begin{cases} \nabla \cdot \mathbf{u}^{n+1} = 0 \\ \boldsymbol{\omega}^{n+1} \cdot \mathbf{n}_z = (\nabla \times \mathbf{u}^{n+1}) \cdot \mathbf{n}_z \\ \dfrac{\nabla^2 \mathbf{u}^{n+1} - \nabla^2 \mathbf{u}^n}{\Delta t} \cdot \mathbf{n}_z = \Bigg[\dfrac{3[\nabla^2 \mathbf{S}^n - \nabla(\nabla \cdot \mathbf{S}^n)] - [\nabla^2 \mathbf{S}^{n-1} - \nabla(\nabla \cdot \mathbf{S}^{n-1})]}{2} + \\ \qquad\qquad + \dfrac{1}{Re_\tau} \dfrac{\nabla^4 \mathbf{u}^{n+1} + \nabla^4 \mathbf{u}^n}{2} \Bigg] \cdot \mathbf{n}_z \\ \dfrac{\boldsymbol{\omega}^{n+1} - \boldsymbol{\omega}^n}{\Delta t} \cdot \mathbf{n}_z = \left(\dfrac{3\nabla \times \mathbf{S}^n - \nabla \times \mathbf{S}^{n-1}}{2} + \dfrac{1}{Re_\tau} \dfrac{\nabla^2 \boldsymbol{\omega}^{n+1} + \nabla^2 \boldsymbol{\omega}^n}{2} \right) \cdot \mathbf{n}_z \\ \dfrac{\phi^{n+1} - \phi^n}{\Delta t} = \dfrac{3S_\phi^n - S_\phi^{n-1}}{2} + \dfrac{s}{Pe_\phi} \nabla^2 \phi^{n+1} - \dfrac{Ch^2}{Pe_\phi} \nabla^4 \phi^{n+1} \\ \dfrac{\psi^{n+1} - \psi^n}{\Delta t} = \dfrac{3S_\psi^n - S_\psi^{n-1}}{2} + \dfrac{Pi}{Pe_\psi} \nabla^2 \psi^{n+1} \end{cases} \tag{2.75}$$

2.5.1 Pseudo-spectral discretization

All equations are solved in modal space; Fourier and Chebyshev transforms are employed to switch from a physical to a modal representation of variables. A generic variable, $f(x,y,z,t)$, in physical space can be represented in modal space as a function of Fourier wavenumbers and Chebyshev polynomials, T_k.

$$f(x,y,z,t) = \sum_{i=0}^{N_x/2} \sum_{j=-N_y/2+1}^{N_y/2} \sum_{k=0}^{N_z-1} \hat{f}(k_{x,i}, k_{y,j}, k, t) T_k(z) e^{\iota(k_{x,i}x + k_{y,j}y)} \tag{2.76}$$

The Fourier coefficient $\hat{f}(k_{x,i}, k_{y,j}, k, t)$ depends on the wavenumbers, $k_{x,i}$ and $k_{y,j}$, on the k^{th} Chebyshev polynomial and on time ($\iota = \sqrt{-1}$ is the imaginary unit). The x and y Fourier wavenumbers are defined as:

$$k_{x,i} = \frac{2\pi(i-1)}{L_x} \qquad i = 1, \ldots, N_x/2+1 \ , \tag{2.77}$$

$$k_{y,j} = \begin{cases} \dfrac{2\pi(j-1)\pi}{L_y} & j = 1, \ldots, N_y/2+1 \\ -\dfrac{2\pi(N_y - j + 1)}{L_y} & j = N_y/2+2, \ldots, N_y \end{cases} . \tag{2.78}$$

Chebyshev polynomials and their derivatives are defined recursively:

$$\begin{aligned} &T_0(z) = 1 && \frac{\partial T_0(z)}{\partial z} = 0 \\ &T_1(z) = z && \frac{\partial T_1(z)}{\partial z} = 1 \\ &\vdots && \vdots \\ &T_n(z) = 2zT_{n-1}(z) - T_{n-2}(z) && \frac{\partial T_n(z)}{\partial z} = \frac{\partial T_{n-2}(z)}{\partial z} + 2nT_{n-1} \end{aligned} . \tag{2.79}$$

One of the main advantages of spectral and pseudo-spectral method is the accuracy in the calculation of derivatives: spatial derivatives in modal space are exact. However, a truncation error is introduced when truncating the infinite Fourier and Chebyshev series to a finite sum of interpolating functions; nevertheless this truncation error is extremely small. Derivatives in the homogeneous directions (x and y) can be immediately computed from Eq. (2.76):

$$\frac{\partial f(x,y,z,t)}{\partial x} = \sum_{i=0}^{N_x/2} \sum_{j=-N_y/2+1}^{N_y/2} \sum_{k=0}^{N_z-1} \iota k_{x,i} \hat{f} T_k e^{\iota(k_{x,i}x + k_{y,j}y)} \ , \tag{2.80}$$

$$\frac{\partial f(x,y,z,t)}{\partial y} = \sum_{i=0}^{N_x/2} \sum_{j=-N_y/2+1}^{N_y/2} \sum_{k=0}^{N_z-1} \iota k_{y,j} \hat{f} T_k e^{\iota(k_{x,i}x + k_{y,j}y)} \ . \tag{2.81}$$

Once defined the variables in modal space, the system of equations Eq. (2.75) can be transformed in modal space. As Fourier modes are all orthogonal, the problem can be split in $(N_x/2+1) \times N_y$ independent subproblems, one for every wavenumber couple $(k_{x,i}, k_{y,j})$. To shorten the notation, in the following the symbol $\hat{f}$ will correspond to the Chebyshev discretization of Fourier modes at a generic wavenumber couple:

$$\hat{f} = \hat{f}_{i,j} = \sum_{k=0}^{N_z-1} \hat{f}(k_{x,i}, k_{y,j}, k, t) T_k(z) e^{\iota(k_{x,i}x + k_{y,j}y)} \ , \tag{2.82}$$

for each couple $(i,j) \in ([1, N_x/2+1], [-N_y/2+1, N_y/2])$. With this compact notation, the system of equation results in:

$$\begin{cases}
\iota k_{x,i}\hat{u}^{n+1} + \iota k_{y,j}\hat{v}^{n+1} + \dfrac{\partial \hat{w}^{n+1}}{\partial z} = 0 \\
\hat{\omega}_z^{n+1} = \iota k_{x,i}\hat{v}^{n+1} - \iota k_{y,j}\hat{u}^{n+1} \\
\dfrac{1}{\Delta t}\left(\dfrac{\partial^2 \hat{w}^{n+1}}{\partial z^2} - k_{i,j}^2 \hat{w}^{n+1} - \dfrac{\partial^2 \hat{w}^{n}}{\partial z^2} + k_{i,j}^2 \hat{w}^{n}\right) = \\
\qquad = \dfrac{3}{2}\left(-k_{i,j}^2 \hat{S}_z^n - \iota k_{x,i}\dfrac{\partial \hat{S}_x^n}{\partial z} - \iota k_{y,j}\dfrac{\partial \hat{S}_y^n}{\partial z}\right) - \\
\qquad - \dfrac{1}{2}\left(-k_{i,j}^2 \hat{S}_z^{n-1} - \iota k_{x,i}\dfrac{\partial \hat{S}_x^{n-1}}{\partial z} - \iota k_{y,j}\dfrac{\partial \hat{S}_y^{n-1}}{\partial z}\right) + \\
\qquad + \dfrac{1}{2Re_\tau}\left(k_{i,j}^4 \hat{w}^{n+1} + \dfrac{\partial^4 \hat{w}^{n+1}}{\partial z^4} - 2k_{i,j}^2\dfrac{\partial^2 \hat{w}^{n+1}}{\partial z^2}\right) + \\
\qquad + \dfrac{1}{2Re_\tau}\left(k_{i,j}^4 \hat{w}^{n} + \dfrac{\partial^4 \hat{w}^{n}}{\partial z^4} - 2k_{i,j}^2\dfrac{\partial^2 \hat{w}^{n}}{\partial z^2}\right) \\
\dfrac{\hat{\omega}_z^{n+1} - \hat{\omega}_z^{n}}{\Delta t} = \dfrac{3}{2}\left(\iota k_{x,i}\hat{S}_y^n - \iota k_{y,j}\hat{S}_x^n\right) - \dfrac{1}{2}\left(\iota k_{x,i}\hat{S}_y^{n-1} - \iota k_{y,j}\hat{S}_x^{n-1}\right) + \\
\qquad + \dfrac{1}{2Re_\tau}\left(\dfrac{\partial^2 \hat{\omega}_z^{n+1}}{\partial z^2} - k_{i,j}^2\hat{\omega}_z^{n+1} + \dfrac{\partial^2 \hat{\omega}_z^{n}}{\partial z^2} - k_{i,j}^2\hat{\omega}_z^{n}\right) \\
\dfrac{\hat{\phi}^{n+1} - \hat{\phi}^{n}}{\Delta t} = \dfrac{3\hat{S}_\phi^n - \hat{S}_\phi^{n-1}}{2} + \dfrac{s}{Pe_\phi}\left(\dfrac{\partial^2 \hat{\phi}^{n+1}}{\partial z^2} - k_{i,j}^2\hat{\phi}^{n+1}\right) - \\
\qquad - \dfrac{Ch^2}{Pe_\phi}\left(k_{i,j}^4\hat{\phi}^{n+1} + \dfrac{\partial^4 \hat{\phi}^{n+1}}{\partial z^4} - 2k_{i,j}^2\dfrac{\partial^2 \hat{\phi}^{n+1}}{\partial z^2}\right) \\
\dfrac{\hat{\psi}^{n+1} - \hat{\psi}^{n}}{\Delta t} = \dfrac{3\hat{S}_\psi^n - \hat{S}_\psi^{n-1}}{2} + \dfrac{Pi}{Pe_\psi}\left(\dfrac{\partial^2 \hat{\psi}^{n+1}}{\partial z^2} - k_{i,j}^2\hat{\psi}^{n+1}\right)
\end{cases} . \tag{2.83}$$

The coefficient $k_{i,j}^2$ is the sum of the square of the corresponding wavenumbers: $k_{i,j}^2 = k_{x,i}^2 + k_{y,j}^2$. All terms, which are already known (current, n, and previous, $n-1$, time step), can be collected in a history term.

$$H_x^n = \Delta t\left[\frac{3\hat{S}_x^n - \hat{S}_x^{n-1}}{2} + \frac{1}{2Re_\tau}\frac{\partial^2 \hat{u}^n}{\partial z^2} + \left(\frac{1}{\Delta t} - \frac{k_{i,j}^2}{2Re_\tau}\right)\hat{u}^n\right] \tag{2.84}$$

$$H_y^n = \Delta t \left[\frac{3\hat{S}_y^n - \hat{S}_y^{n-1}}{2} + \frac{1}{2Re_\tau}\frac{\partial^2 \hat{v}^n}{\partial z^2} + \left(\frac{1}{\Delta t} - \frac{k_{i,j}^2}{2Re_\tau} \right) \hat{v}^n \right] \tag{2.85}$$

$$H^n = \frac{\partial}{\partial z}(\imath k_{x,i} H_x^n + \imath k_{y,j} H_y^n) + k_{i,j}^2 H_z^n \tag{2.86}$$

$$H_\phi^n = \frac{\Delta t}{2}(3\hat{S}_\phi^n - \hat{S}_\phi^{n-1}) + \hat{\phi}^n \tag{2.87}$$

$$H_\psi^n = \frac{\Delta t}{2}(3\hat{S}_\psi^n - \hat{S}_\psi^{n-1}) + \hat{\psi}^n \tag{2.88}$$

Exploiting the history terms and taking the unknowns (time step $n+1$) at the left hand side, we obtain for each couple (i, j):

$$\begin{cases} \imath k_{x,i}\hat{u}^{n+1} + \imath k_{y,j}\hat{v}^{n+1} + \dfrac{\partial \hat{w}^{n+1}}{\partial z} = 0 \\ \hat{\omega}_z^{n+1} = \imath k_{x,i}\hat{v}^{n+1} - \imath k_{y,j}\hat{u}^{n+1} \\ \left(\dfrac{\partial^2}{\partial z^2} - \beta^2 \right)\left(\dfrac{\partial^2}{\partial z^2} - k_{i,j}^2 \right)\hat{w}^{n+1} = \dfrac{H^n}{\gamma} \\ \left(\dfrac{\partial^2}{\partial z^2} - \beta^2 \right)\hat{\omega}_z^{n+1} = -\dfrac{\imath k_{x,i}H_y^n - \imath k_{y,j}H_x^n}{\gamma} \\ \left(\dfrac{\partial^2}{\partial z^2} - \beta_\phi^2 \right)\left(\dfrac{\partial^2}{\partial z^2} - \beta_\phi^2 \right)\hat{\phi}^{n+1} = \dfrac{H_\phi^n}{\gamma_\phi} \\ \left(\dfrac{\partial^2}{\partial z^2} - \beta_\psi^2 \right)\hat{\psi}^{n+1} = -\dfrac{H_\psi^n}{\gamma_\psi} \end{cases} . \tag{2.89}$$

The parameters γ, γ_ϕ, γ_ψ and β, β_ϕ, β_ψ are defined as:

$$\gamma = \frac{\Delta t}{2Re_\tau} \quad , \quad \beta^2 = \frac{1 + \gamma k_{i,j}^2}{\gamma} \ , \tag{2.90}$$

$$\gamma_\phi = \frac{Ch^2 \Delta t}{Pe_\phi} \quad , \quad \beta_\phi^2 = \frac{s}{2Ch^2} + k_{i,j}^2 \ , \tag{2.91}$$

$$\gamma_\psi = \frac{Pi \Delta t}{Pe_\psi} \quad , \quad \beta_\psi^2 = \frac{1 + \gamma_\psi k_{i,j}^2}{\gamma_\psi} \ . \tag{2.92}$$

Chebyshev-Tau method

The Chebyshev-Tau method is employed to solve all the independent problems for each Fourier wavenumber couple. This method can be applied to solve one-dimensional second order equations with mixed boundary conditions. The Chebyshev polynomials are chosen as test functions together with the weights $(1 - z^2)^{-1/2}$. This choice allows to exploit the orthogonality of the polynomials.

$$\int_{-1}^{+1} T_j(z)T_k(z)\frac{1}{\sqrt{1-z^2}}\mathrm{d}z = \begin{cases} 0 & \text{if } j \neq k \\ \pi & \text{if } j = k = 0 \\ \pi/2 & \text{if } j = k \neq 0 \end{cases} \tag{2.93}$$

In total $N_z - 2$ test function are employed; the boundary conditions at $z = \pm 1$ close the problem.

The Chebyshev-Tau method will be now presented for a generic one-dimensional Helmholtz equation:

$$\frac{\partial^2 u}{\partial z^2} - \alpha^2 u = F \ . \tag{2.94}$$

The functions u and F can be written as truncated Chebyshev series:

$$u = \sum_{n=0}^{N_z-1} a_n T_n(z) \ , \tag{2.95}$$

$$F = \sum_{n=0}^{N_z-1} b_n T_n(z) \ . \tag{2.96}$$

The equation is then integrated twice in z from -1 to z. The following property of Chebyshev polynomials is exploited:

$$\int_{-1}^{z} \sum_{n=0}^{N_z-1} c_n T_n(s)\mathrm{d}s = \sum_{n=1}^{N_z} l_n T_n(z) \ . \tag{2.97}$$

The coefficients l_n can be expressed in terms of the coefficients c_n:

$$\begin{cases} l_n = \dfrac{1}{2(Nz-1)}(c_{n-1} - c_{n+1}) & \text{for } n = 1, \ldots, N_z - 2 \\ l_{N_z-1} = \dfrac{c_{N_z-1}}{2(N_z-1)} & \\ l_{N_z} = \dfrac{c_{N_z-1}}{2N_z} & \end{cases} \ . \tag{2.98}$$

Upon integration over z twice we get:

$$\sum_{n=0}^{N_z-1} a_n T_n(z) - AT_1(z) - BT_0(z) - \alpha^2 \sum_{n=2}^{N_z+1} m_n T_n(z) = \sum_{n=2}^{N_z+1} f_n T_n(z) \ . \tag{2.99}$$

where the coefficients m_n and f_n are obtained exploiting twice Eq. (2.98). The coefficient A and B are:

$$A = \left.\frac{\partial u}{\partial z}\right|_{z=-1} \ , \qquad B = \left.\frac{\partial u}{\partial z}\right|_{z=-1} + u(z=-1) \ . \tag{2.100}$$

To get a more compact notation the coefficient $h_n = a_n - \beta^2 m_n - f_n$ is introduced.

$$(a_0 - B)T_0(z) + (a_1 - A)T_1(z) + \sum_{n=2}^{N_z-1} h_n T_n(z) - \sum_{n=N_z}^{N_z+1} (\beta^2 m_n - f_n)T_n(z) = 0 \quad (2.101)$$

The Chebyshev-Tau method solves the differential equation in weak form, so the integral over the domain of the equation multiplied by a test function f must be zero for each test function. By choosing the Chebyshev polynomials $T_2, \ldots, T_{N_z-1}$ as test functions with the weight $(1-z^2)^{-1/2}$, the orthogonality of Chebyshev polynomials can be exploited. The missing two equations are obtained from the boundary conditions:

$$p_1 \sum_{n=0}^{N_z-1} a_n T_n(-1) + q_1 \sum_{n=0}^{N_z-1} a_n \left.\frac{\partial T_n}{\partial z}\right|_{z=-1} = r_1 \ , \quad (2.102)$$

$$p_2 \sum_{n=0}^{N_z-1} a_n T_n(+1) + q_2 \sum_{n=0}^{N_z-1} a_n \left.\frac{\partial T_n}{\partial z}\right|_{z=+1} = r_2 \ . \quad (2.103)$$

In a more compact form, $d_n = p_1 T_n + q_1 \partial T_n/\partial z$ and $e_n = p_2 T_n + q_2 \partial T_n/\partial z$. Using the relation reported in Eq. (2.98) the coefficient m_n can be expressed as a linear function of a_n coefficients, while f_n as a linear function of b_n; this way a linear system of equations for the unknown coefficents a_n is obtained.

$$\begin{bmatrix} d_1 & d_2 & d_3 & d_4 & d_5 & d_6 & d_7 & d_8 & \ldots & d_{N_z} \\ e_1 & e_2 & e_3 & e_4 & e_5 & e_6 & e_7 & e_8 & \ldots & e_{N_z} \\ s_1 & 0 & v_1 & 0 & t_1 & 0 & 0 & 0 & \ldots & 0 \\ 0 & s_2 & 0 & v_2 & 0 & t_2 & 0 & 0 & \ldots & 0 \\ 0 & 0 & s_3 & 0 & v_3 & 0 & t_3 & 0 & \ldots & 0 \\ \vdots & \vdots & \vdots & \vdots & \vdots & \vdots & \vdots & \vdots & \ddots & \vdots \\ 0 & 0 & 0 & 0 & 0 & 0 & 0 & 0 & \ldots & v_{N_z-2} \end{bmatrix} \begin{bmatrix} a_0 \\ a_1 \\ a_2 \\ a_3 \\ a_4 \\ \vdots \\ a_{N_z-1} \end{bmatrix} = \begin{bmatrix} r_1 \\ r_2 \\ g_1 \\ g_2 \\ g_3 \\ \vdots \\ g_{N_z-2} \end{bmatrix} \quad (2.104)$$

The coefficients of the matrix are:

$$s_{n-2} = -\alpha^2 n \qquad n = 3, \ldots, N_z \ , \quad (2.105)$$

$$v_{n-2} = 4n(n-1)(n-2) + 2(n-1)\alpha^2 \qquad n = 3, \ldots, N_z \ , \quad (2.106)$$

$$t_{n-2} = -\alpha^2(n-2) \qquad n = 3, \ldots, N_z - 2 \ , \quad (2.107)$$

$$g_n = \begin{cases} g_{n-2} = n b_{n-2} - 2(n-1)b_n + (n+2)b_{n+2} & n = 3, \ldots, N_z - 2 \\ g_{N_z-3} = (N_z - 3)b_{N_z-5} - 2(N_z - 4)b_{N_z-3} & \\ g_{N_z-2} = (N_z - 2)b_{N_z-4} - 2(N_z - 3)b_{N_z-2} & \end{cases} \ . \quad (2.108)$$

The coefficient matrix has the first two rows full (from the boundary conditions) and from the third to the last (N_z) row is a tridiagonal matrix. This system can be readily solved using a Gauss-Jordan elimination algorithm followed by forward substitution.

The Chebyshev-Tau method is applied to the fourth order equation for the velocity, the second order equation for the vorticity, the fourth order equation for the phase field and the second order equation for the surfactant concentration. In the following it will be shown how to get from the problem equations to an Helmholtz form, as in Eq. (2.94). Then, the Chebyshev-Tau method applies to each Helmholtz-like equation as shown in the previous steps.

Boundary conditions

Due to the Fourier discretization in the streamwise and spanwise directions (x and y), periodic boundary conditions are implicitly enforced in these directions. A closed channel setup is being considered: two solid walls bound the channel at $z = \pm 1$ (dimensionless units). No-slip and no-flux boundary conditions are imposed on the flow field; at the wall the fluid moves with the same velocity of the wall.

$$\begin{cases} \mathbf{u}(x,y,z=\pm 1) = [u_w, v_w, 0] \\ \left.\dfrac{\partial w}{\partial z}\right|_{z=\pm 1} = 0 \end{cases} \tag{2.109}$$

For the shear flow setup u_w and v_w are respectively the x and y direction velocities of the moving wall. From the no-slip condition at the wall the boundary condition for the wall-normal component of the vorticity is obtained:

$$\omega_z(x,y,z=\pm 1) = 0 \ . \tag{2.110}$$

No-flux boundary conditions are enforced for both the phase field and the surfactant concentration. As the phase field transport equation is a fourth order differential equation, two additional boundary conditions are needed; in particular, a no-flux boundary condition is imposed at the two solid walls also on the phase field chemical potential.

$$\begin{cases} \left.\dfrac{\partial \phi}{\partial z}\right|_{z=\pm 1} = 0 \\ \left.\dfrac{\partial^3 \phi}{\partial z^3}\right|_{z=\pm 1} = 0 \end{cases} \tag{2.111}$$

$$\left.\frac{\partial \psi}{\partial z}\right|_{z=\pm 1} = 0 \tag{2.112}$$

Solution of the velocity equation

The equation for the wall-normal velocity is a fourth-order equation, thus the Chebyshev-Tau method cannot be directly applied. The equation is then split in two second order Helmholtz-like equations, so that the Chebyshev-Tau method can be applied to each of these second order equations.

$$\begin{cases} \dfrac{\partial^2 \theta^{n+1}}{\partial z^2} - \beta^2 \theta^{n+1} = \dfrac{H^n}{\gamma} \\ \dfrac{\partial^2 \hat{w}^{n+1}}{\partial z^2} - k_{i,j}^2 \hat{w}^{n+1} = \theta^{n+1} \end{cases} \tag{2.113}$$

Two separate differential problems are obtained for the wall-normal velocity $\hat{w}^{n+1}$ and the auxiliary variable $\hat{\theta}^{n+1}$; however, the physical boundary conditions apply only to the first problem (boundary conditions on the value of the velocity and its derivative at the wall). As there are no physical boundary conditions for the auxiliary problem, the influence matrix method has to be employed.

Using the influence matrix method, the solutions $\hat{w}^{n+1}$ and θ^{n+1} can be split in three contributions: a first contribution that does not necessarily verify the boundary conditions (w_1 and θ_1) and two contributions that verify the boundary conditions at one boundary (w_2, w_3 and θ_2, θ_3). A linear combination of these three contributions gives the solution $\hat{w}^{n+1}$ and θ^{n+1}.

$$\begin{cases} \hat{w}^{n+1} = w_1 + A w_2 + B w_3 \\ \theta^{n+1} = \theta_1 + A\theta_2 + B\theta_3 \end{cases} \tag{2.114}$$

The coefficients A and B have to be determined to obtain the value of the unknowns; the subproblems denoted by the subscript 1, 2 and 3 are second order differential equations with a unique solution. In particular the first subproblem, subscript 1, has a solution which does not necessarily satisfy the imposed boundary conditions; subproblem 2 verifies the boundary conditions at $z = -1$, while subproblem 3 verifies the boundary conditions at $z = +1$. In the following the domain will be denoted as Ω, while its boundaries ($z = \pm 1$) as Γ.

$$[P_1] = \begin{cases} \dfrac{\partial^2 w_1}{\partial z^2} - k_{i,j}^2 w_1 = \theta_1 & \text{in } \Omega \\ w_1 = w_\Gamma & \text{in } \Gamma \\ \dfrac{\partial^2 \theta_1}{\partial z^2} - \beta^2 \theta_1 = \dfrac{H^n}{\gamma} & \text{in } \Omega \\ \theta_1 = \theta_\Gamma & \text{in } \Gamma \end{cases} \tag{2.115}$$

$$[P_2] = \begin{cases} \dfrac{\partial^2 w_2}{\partial z^2} - k_{i,j}^2 w_2 = \theta_2 & \text{in } \Omega \\ w_2 = 0 & \text{in } \Gamma \\ \dfrac{\partial^2 \theta_2}{\partial z^2} - \beta^2 \theta_2 = 0 & \text{in } \Omega \\ \theta_2(z = -1) = 1 \qquad \theta_2(z = +1) = 0 & \end{cases} \tag{2.116}$$

$$[P_3] = \begin{cases} \dfrac{\partial^2 w_3}{\partial z^2} - k_{i,j}^2 w_3 = \theta_3 & \text{in } \Omega \\ w_3 = 0 & \text{in } \Gamma \\ \dfrac{\partial^2 \theta_3}{\partial z^2} - \beta^2 \theta_3 = 0 & \text{in } \Omega \\ \theta_3(z = -1) = 0 \qquad \theta_3(z = +1) = 1 & \end{cases} \tag{2.117}$$

The boundary condition on $[P_1]$ is arbitrary; $w_\Gamma = 0$ and $\theta_\Gamma = 0$ were selected. The subproblem $[P_1]$ is time-dependent as the history term H^n changes over time; the solutions to subproblems $[P_2]$ and $[P_3]$ do not depend on time and are calculated only once.

The most general form of the boundary conditions on the wall-normal velocity is:

$$\begin{cases} p_1 \hat{w}^{n+1}(x, y, z = -1) + q_1 \left.\dfrac{\partial \hat{w}^{n+1}}{\partial z}\right|_{z=-1} = r_1 \\ p_2 \hat{w}^{n+1}(x, y, z = +1) + q_2 \left.\dfrac{\partial \hat{w}^{n+1}}{\partial z}\right|_{z=+1} = r_2 \end{cases} . \tag{2.118}$$

The variable $\hat{w}^{n+1}$ can be split in the three contributions, $\hat{w}^{n+1} = w_1 + Aw_2 + Bw_3$, and substituted in the boundary conditions. This way a linear system for the unknown coefficients A and B is obtained.

$$\begin{bmatrix} p_1 w_2(-1) + q_1 \left.\dfrac{\partial w_2}{\partial z}\right|_{z=-1} & p_1 w_3(-1) + q_1 \left.\dfrac{\partial w_3}{\partial z}\right|_{z=-1} \\ p_2 w_2(-1) + q_2 \left.\dfrac{\partial w_2}{\partial z}\right|_{z=-1} & p_2 w_3(-1) + q_2 \left.\dfrac{\partial w_3}{\partial z}\right|_{z=-1} \end{bmatrix} \begin{bmatrix} A \\ B \end{bmatrix} = \begin{bmatrix} \widetilde{r}_1 \\ \widetilde{r}_2 \end{bmatrix} \tag{2.119}$$

The right hand side is given by:

$$\begin{bmatrix} \widetilde{r}_1 \\ \widetilde{r}_2 \end{bmatrix} = \begin{bmatrix} r_1 - p_1 w_1(-1) - q_1 \left.\dfrac{\partial w_1}{\partial z}\right|_{z=-1} \\ r_2 - p_2 w_1(-1) - q_2 \left.\dfrac{\partial w_1}{\partial z}\right|_{z=-1} \end{bmatrix} . \tag{2.120}$$

Once obtained the unique solutions w_1, w_2 and w_3 from the three subproblems and calculated the unknown parameters A and B, the unknown wall-normal velocity $\hat{w}^{n+1}$ is obtained.

The complete flow field is determined once the wall-normal velocity and vorticity are known; using the continuity equation and the definition of the wall-normal vorticity the values of $\hat{u}^{n+1}$ and $\hat{v}^{n+1}$ are obtained.

$$\begin{bmatrix} -\iota k_{y,j} & \iota k_{x,i} \\ \iota k_{x,i} & \iota k_{y,j} \end{bmatrix} \begin{bmatrix} \hat{u}^{n+1} \\ \hat{v}^{n+1} \end{bmatrix} = \begin{bmatrix} \hat{\omega}_z^{n+1} \\ -\dfrac{\partial \hat{w}^{n+1}}{\partial z} \end{bmatrix} \tag{2.121}$$

This method however fails when the determinant of the matrix of coefficients is zero; this occurs for $k_{i,j}^2 = 0$, so for $k_{x,i} = 0$ and $k_{y,j} = 0$. These wavenumbers correspond to the mean modes in the x and y direction. The solution for the mean mode of u and v can be calculated starting from the fourth order equation Eq. (2.72) and substituting $k_{x,0} = 0$ and $k_{y,0} = 0$. This way, two second order equations for $\hat{u}^{n+1}$ and $\hat{v}^{n+1}$ are obtained.

$$\begin{cases} \dfrac{\partial^2 \hat{u}^{n+1}}{\partial z^2} - \dfrac{\hat{u}^{n+1}}{\gamma} = -\dfrac{H_x^n}{\gamma} \\ \hat{u}(z = \pm 1) = u_w \end{cases} \tag{2.122}$$

$$\begin{cases} \dfrac{\partial^2 \hat{v}^{n+1}}{\partial z^2} - \dfrac{\hat{v}^{n+1}}{\gamma} = -\dfrac{H_y^n}{\gamma} \\ \hat{v}(z = \pm 1) = v_w \end{cases} \tag{2.123}$$

Solution of the vorticity equation

The equation for the wall-normal vorticity is already a one-dimensional second order Helmholtz equation, thus it does not require any particular treatment.

$$\begin{cases} \dfrac{\partial^2 \hat{\omega}_z^{n+1}}{\partial z^2} - \beta^2 \hat{\omega}_z^{n+1} = -\dfrac{\imath k_{x,i} H_y^2 - \imath k_{y,j} H_x^n}{\gamma} \\ \hat{\omega}_z(z = \pm 1) = 0 \end{cases} \tag{2.124}$$

The Chebyshev-Tau method can be readily applied to get the new vorticity value.

Solution of the phase field equation

The fourth order equation for the phase field is split in two subproblems, one for the phase field and one for the auxiliary variable $\hat{\theta}^{n+1}$.

$$\begin{cases} \dfrac{\partial^2 \hat{\phi}^{n+1}}{\partial z^2} - \beta_\phi^2 \hat{\phi}^{n+1} = \theta^{n+1} \\ \left.\dfrac{\partial \hat{\phi}^{n+1}}{\partial z}\right|_{z=\pm 1} = 0 \end{cases} \tag{2.125}$$

$$\begin{cases} \dfrac{\partial^2 \theta^{n+1}}{\partial z^2} - \beta_\phi^2 \theta^{n+1} = \dfrac{H_\phi^n}{\gamma_\phi} \\ \left.\dfrac{\partial \theta^{n+1}}{\partial z}\right|_{z=\pm 1} = 0 \end{cases} \tag{2.126}$$

Here, as both problems have physical boundary conditions, the influence matrix method is not needed and the two subproblems can be directly solved. First, the problem for $\hat{\theta}^{n+1}$ is solved, then the phase field is calculated.

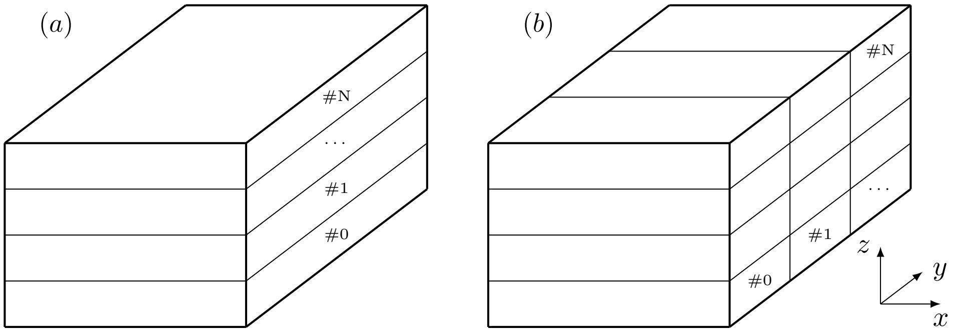

FIGURE 2.7 – Slab, panel (*a*), and pencil, panel (*b*), decomposition of the computational domain in physical space. The numbering of the tasks, #0, #1, ..., #N, is reported for reference.

Solution of the surfactant transport equation

The surfactant concentration transport equation is a second order Helmholtz equation and can be directly solved applying the Chebyshev-Tau method.

$$\begin{cases} \dfrac{\partial^2 \hat{\psi}^{n+1}}{\partial z^2} - \beta_\psi^2 \hat{\psi}^{n+1} = -\dfrac{H_\psi^n}{\gamma_\psi} \\ \left.\dfrac{\partial \hat{\psi}^{n+1}}{\partial z}\right|_{z=\pm 1} = 0 \end{cases} \tag{2.127}$$

2.6 Code implementation

The presented numerical method has been implemented in a parallel Fortran code. A pure-MPI (Message Passing Interface) approach is adopted to divide the workload among independent MPI tasks; the computational domain is evenly distributed among all the tasks. The main idea lying behind the MPI approach is the division of the workload among several different tasks that work independently one from each other (exception made for the communications among tasks); each tasks has its own private variable space, which is not directly accessible to other tasks. With the current implementation, the domain is split using a 2D decomposition (pencil decomposition): the computational domain is partitioned along two out of three dimensions (pencil-like subdomains). This partitioning constitutes an improvement with respect to the 1D decomposition (slab decomposition), in which the computational domain is partitioned along only one direction out of three; a graphical visualization of these domain partitioning approaches is reported in Fig. 2.7. While on one hand the pencil decomposition increases the volume of data communication among the tasks and slightly increases the replication of data across the variable space of different tasks (parameters, constants, ...), on the other hand it greatly increases the maximum number of tasks that can be used to divide the workload. The maximum number of tasks is limited by the number of grid points: for a grid with $\mathcal{O}(N^3)$ points, the maximum number of tasks for the slab decomposition is $\mathcal{O}(N)$, while for the pencil decomposition is $\mathcal{O}(N^2)$. This

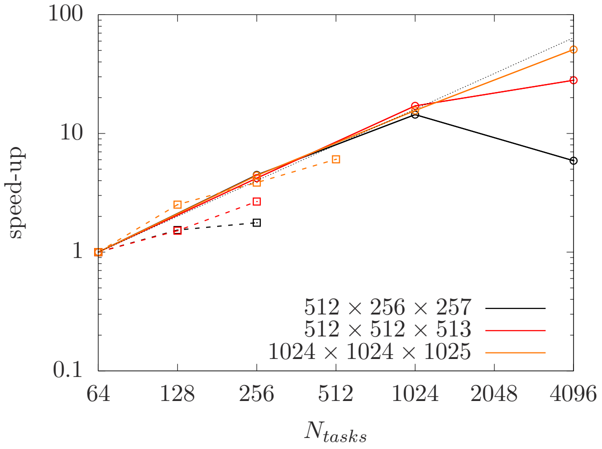

FIGURE 2.8 – Comparison between slab (dashed lines with square markers) and pencil (solid line with circle markers) decomposition for different grid sizes. The speed-up with respect to a reference case on 64 tasks is shown; the ideal scaling is reported with a thin black dotted line. The pencil decomposition achieves better performances than the slab decomposition even at low numbers of tasks. The loss of performances for increasing number of tasks can be appreciated for the coarser grid, $N_x \times N_y \times N_z = 512 \times 256 \times 257$. Performance results were obtained on the Broadwell (BDW) partition of the HPC system Marconi hosted at CINECA (Bologna, Italy).

limitation occurs as the minimum size of a slab is $N \times N \times 1$, while for a pencil it is $N \times 1 \times 1$: each subdomain must include at least one grid point in each direction. The pencil decomposition thus overcomes the limitation of the maximum number of tasks that could be employed; in addition it also shows better performances even at low numbers of tasks, Fig. 2.8. A loss of performances for increasing number of MPI tasks can be observed in Fig. 2.8 for the coarse and intermediate grids: in these cases the number of grid points held by each task becomes too low ($\mathcal{O}(8k)$ points per task for the coarse grid and $\mathcal{O}(33k)$ for the intermediate one). As the number of grid points per task is too low, the time spent in communications among tasks overcomes the time spent in actual calculations, reducing the overall performances of the code.

The distribution of the computational domain is defined with two parameters, $N_{y,CPU}$ and $N_{z,CPU}$; these parameters determine the partitioning of the domain along the y and z directions. In physical space each task holds all the points in the x direction and a fraction of the points in the y and z directions. This way a Fourier transform can be readily taken in the x direction: to compute a Fourier or Chebyshev transform all points in the transform direction are needed. Once the Fourier transform in the x direction has been taken, the pencils are transposed: data are communicated through MPI communications among the various tasks, so that each task holds all the points in the y direction and only a fraction in the remaining directions. Then, Fourier transforms in the y direction are taken. Again, the pencils are transposed so that each task holds all the points in the z direction and then Chebyshev transforms are taken. In modal space the computational domain is divided along the x and y directions (each task holds all the points in the wall-normal direction). The transform from physical to modal space thus requires: (i) one-dimensional Fourier transforms

TABLE 2.1 – Characteristics of the HPC machines on which performance benchmarks were run

Machine	HPC centre	Node layout	Frequency [GHz]
Marconi BDW	CINECA (IT)	2×18 cores Intel Xeon	2.3
Marconi KNL	CINECA (IT)	1×68 cores Intel Xeon Phi	1.4
Vesta	ANL (USA)	1×16 cores IBM BG/Q	1.6
VSC-3	VSC (AT)	2×8 cores Intel Xeon	2.6

(x direction), (*ii*) pencil transposition, (*iii*) one-dimensional Fourier transforms (y direction), (*iv*) pencil transposition and (*v*) one-dimensional Chebyshev transforms (z direction). The transform from modal to physical space follows the same path backwards. This process is thus constituted of intensive computation phases (Fourier and Chebyshev transforms) interleaved with MPI communications among the various tasks. A MPI Cartesian communicator is adopted to easily define the communication pattern. Fast Fourier and Chebyshev transforms are taken using the functions provided in the library *FFTW* (version 3.3.8) by Frigo and Johnson [50]. This domain partitioning choice gives the best performances: MPI communications occur only during transforms from physical to modal space (and backwards) and, in modal space, each task solves a series of Helmholtz problems (all Helmholtz problems are independent one from each other). Most of the transforms occur during the calculation of non-linear terms: to avoid the costly calculation of convolution integrals, products of variables are computed in physical space, then the result is transformed in modal space (pseudo-spectral method).

Finally, parallel input/output instructions (MPI I/O library) are adopted when reading/writing large data files; this choice improves the overall performances of the code and allows to distribute the workload among high number of tasks with a limited amount of replicated data (low usage of memory for each task).

The performances of the code were measured on several High Performance Computing (HPC) machines: Marconi BDW, Marconi KNL, Vesta and VSC-3. Details on these machines are reported in Tab. 2.1. Performance data will be reported for the Broadwell (BDW) and Knights Landing (KNL) partitions of Marconi and for Vesta; VSC-3 (Ivy Bridge) has similar performances to Marconi Broadwell, thus has not be reported. The strong scaling benchmark for the various HPC machines is reported in Fig. 2.9. In this benchmark the problem size is kept constant (fixed grid size), while the total number of MPI tasks, N_{tasks}, is increased, thus reducing the load of each task (lower problem size per node). The strong scaling benchmark measures the speed-up with respect to a reference case; here the reference case has been selected as the lower number of tasks that could be run using all physical cores on all the requested nodes. On Marconi BDW and KNL the available RAM per node is higher ($\mathcal{O}(100)$ GB), thus the problem could fit on the memory of two nodes on the BDW partition and one node on the KNL partition. On the other hand, as on Vesta the available RAM per node is 16 GB, the smaller problem size required a minimum of 4 nodes, while the larger problem size required a minimum of 32 nodes. Ideally, the speed-up should grow linearly with the number of tasks employed (thin black dashed line in Fig. 2.9). This benchmark is the most relevant for the cases that will be presented in the following: the total problem size is kept fixed (between $512 \times 256 \times 257$ and $1024 \times 1024 \times 1025$ grid points)

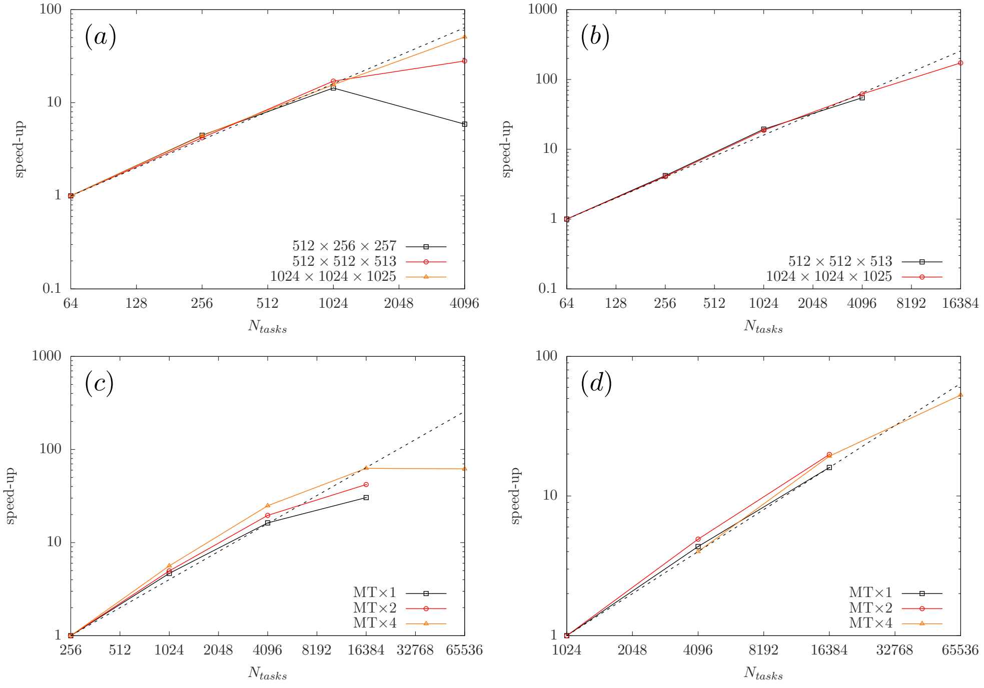

FIGURE 2.9 – Strong scaling for different grid sizes on the various architectures: Marconi BDW, panel (a), Marconi KNL, panel (b), Vesta (grid $512 \times 512 \times 513$ in panel (c) and $1024 \times 1024 \times 1025$ in panel (d)) for different Multi Threading (MT) configurations. A thin black dashed line shows the ideal linear scaling.

and the strong scaling performances of the code are exploited by selecting a total number of tasks that guarantees a reasonable time-to-solution while keeping a high efficiency (speed-up close to the ideal one). As the total number of tasks is increased the parallel overhead also increases: the time spent by the code in communications and synchronizations increases with respect to the time spent in actual computations. This effect is clear for the lower grid sizes (up to $512 \times 512 \times 513$ grid points): as the total number of MPI tasks is increased, the speed-up strongly reduces and departs from the ideal speed-up. The number of points per task becomes too low for increasing total number of tasks, thus the time spent in calculations reduces, while the communication and synchronization time increases. On the larger problem size ($1024 \times 1024 \times 1025$ grid points) the computational load of each task is high enough to mask the time spent in communications and synchronizations calls, thus this case shows an optimal strong scaling for all the numbers of tasks tested. Considering the problem size adopted for the three-dimensional simulations that will be presented in the following, usually about 1024 MPI tasks are employed, so that a strong scaling close to the ideal is always achieved.

Finally, Multi Threading (MT) was also included in the strong scaling benchmarks performed on Vesta (IBM BG/Q architecture). This machine is characterized by 16 physical cores per node; each of these physical cores can spawn up to four virtual cores (threads). A different MPI task can then be assigned to each thread. In total, three Multi Threading configurations were tested: 1, 2 and 4 threads per core (MT×1, MT×2 and MT×4). Multi Threading is an attractive option, as it allows to increase the total number of tasks while keeping the same usage of computational resources: most HPC systems bill for the amount of time a physical core (or node) is requested, without considering the effective number of tasks actually used. Thus, for the same amount of physical computational resources, up to four times virtual computational resources are available with Multi Threading. However, Multi Threading may not always be convenient: the same CPU-level physical resources (for instance registers and L1 and L2 cache levels) are shared among the various threads. Depending on the specifics of the machine it may or may not be advantageous and thus it should be checked beforehand.

2.7 Validation

The numerical method and its implementation have been validated using two different benchmarks. The first one compares the deformation of a droplet in a laminar shear flow with a known analytical solution, while the second one compares the evolution of a Rayleigh-Taylor instability with previous simulations. These benchmarks separately test various components of the method: the former tests the surface force and the viscosity contrast among the phases, while the latter addresses the validation of the density contrast among the phases.

In the following sections each benchmark will be introduced, together with all the relevant parameters and quantities. Then, results from the implemented method will be compared with analytic solutions and widely-accepted numerical solutions.

2.7.1 Drop deformation in shear flow

This benchmark investigates the deformation of a droplet under shear: a single droplet is placed between two walls that move in opposite directions, thus shearing the droplet. This is a commonly used benchmark and several numerical [66, 81, 86, 95] and experimental [55, 124] results are available. An analytic solution was obtained by Taylor [153, 154] with the hypotheses of negligible inertia and small droplet deformation. In his pioneering work with a parallel band apparatus [154], it was shown that the deformation of the droplet is proportional to the capillary number, Ca. With the hypothesis of negligible inertia, the droplet is deformed by viscous shearing (generated by the moving walls), while surface forces oppose this deformation. The capillary number is indeed the ratio of viscous contributions over surface forces:

$$Ca = \frac{We}{Re}\frac{d}{2h} = \frac{u_w \eta}{\sigma_0}\frac{d}{2h} \, . \tag{2.128}$$

Here the velocity of the moving wall, u_w, has been taken as the reference velocity. The rescaling factor $d/2h$ is introduced as in the non-dimensionalization procedure the length scale used is the channel half-height, while most of the previous works use the droplet radius, $d/2$, as the length scale. To better compare with previous works, this rescaling coefficient has been adopted.

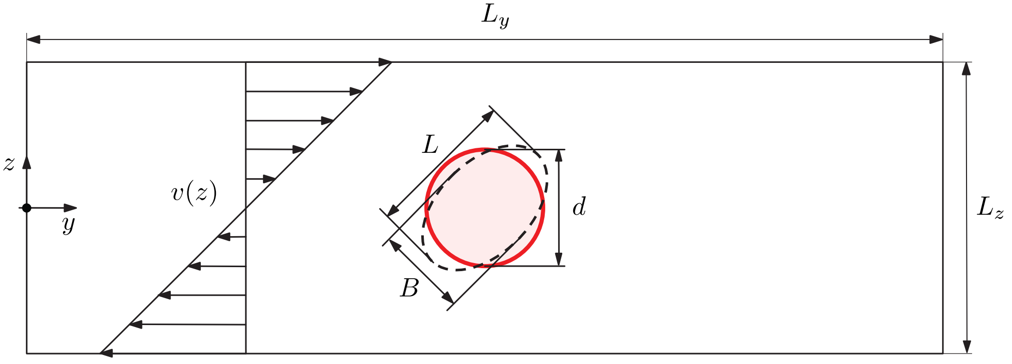

FIGURE 2.10 – Computational domain used for the single droplet deformation benchmark. At the beginning of the simulation a circular droplet (red circle) is released at the channel centre, $z_c = 0$ and $y_c = \pi$. The shear flow, linear velocity profile $v(z)$, deforms the droplet until a new steady-state shape (black dashed line) is reached. In this latter configuration the droplet length, L, and breadth, B, are measured.

The deformation parameter, D, has been here defined according to previous works as:

$$D = \frac{L - B}{L + B} \ . \tag{2.129}$$

The major axis, L, and the minor axis, B, respectively the length and breadth of the droplet, are measured on the droplet projection on the velocity-velocity gradient plane, as shown in Fig. 2.10.

Taylor [153, 154] developed an analytic formula, which describes the small deformation of a droplet as a function of the droplet capillary number, ratio between viscous and surface force contributions, and of the viscosity ratio among the two phases, η_r.

$$D_T = \frac{16 + 19\eta_r}{16 + 16\eta_r} Ca \tag{2.130}$$

This analytic expression was later corrected by Shapira and Haber [139], who accounted for the effect of the lateral confinement on the droplet deformation. This correction includes a factor that considers the ratio of the drop diameter over the channel height, $d/2h$.

$$D = \frac{16 + 19\eta_r}{16 + 16\eta_r} Ca \left[1 + C_{SH} \frac{3.5}{2} \left(\frac{d}{2h} \right)^3 \right] \tag{2.131}$$

The coefficient C_{SH} is a numerical coefficient equal to 5.6996. In the following, this latter formulation will be employed in the comparison against results obtained with the current numerical method.

All simulations for the code validation have been performed considering a two-dimensional domain (2D); the difference between 2D and 3D cases will be later addressed in Chap. 4. There it will be shown how results from 2D numerical simulations well approximate Taylor analytic formula, experimental measurements and results from 3D simulations in the limit of small deformations (low capillary numbers). As

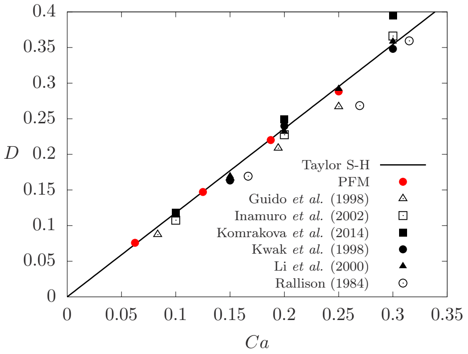

FIGURE 2.11 – Single drop deformation in laminar shear flow. Results from the present simulations (PFM) are compared with Taylor formula (Taylor S-H), Guido and Simeone [55], Inamuro et al. [66], Komrakova et al. [81], Kwak and Pozrikidis [86], Li et al. [95] and Rallison [124]. Shapira and Haber correction is included in Taylor analytic formula.

the following validation is limited to low capillary numbers, the deformation computed for 2D cases can be safely compared with Taylor analytic formula and 3D cases.

The computational setup is reported in Fig. 2.10. The domain size is $L_y \times L_z = 2\pi h \times 2h$ and has been discretized with $N_y \times N_z = 512 \times 513$ grid points in the streamwise and wall-normal directions respectively. The Cahn number has been selected such that there are at least five grid points across the interface; for the present configuration $Ch = 0.02$ was chosen. This value of the Cahn number allows for an accurate description of the phase field and of the steep gradients across the interface. The Péclet number for the phase field was set following the scaling $Pe_\phi = 3/Ch = 150$ [108, 183] in order to achieve the sharp-interface limit. The Reynolds number has been imposed to $Re = 0.1$ to verify the creeping flow hypothesis (negligible inertia). Different values of the capillary number, set via the Weber number, were selected: $Ca = 0.0625$, $Ca = 0.1250$, $Ca = 0.1875$ and $Ca = 0.2500$. The initial velocity field, $v(z)$, is a linear velocity profile for the streamwise component; the other velocity components were set to zero. The top wall moves with velocity $v_w = v(h) = 1$, while the bottom wall moves with velocity $-v_w = v(-h) = -1$. No-slip boundary conditions are enforced at the two moving walls, while periodic conditions are imposed in the streamwise direction. Finally, a single droplet with diameter $d = 0.8h$ is initialized at the channel centre; the phase field follows its equilibrium profile across the interface.

The deformation of the droplet (matched viscosity among the phases) is compared against Taylor corrected formula in Fig. 2.11. An excellent agreement can be observed between results from the current simulations and Taylor formula. Results from previous works (numerical and experimental) are also reported in the figure; the dispersion in these results can be addressed to slightly different flow conditions (Reynolds number), confinement ratio, viscosities of the fluids or presence of impurities. However, a fair agreement among the various results reported can still be appreciated.

The effect of different viscosities between the two phases on the droplet deformation has then been considered and validated against Taylor formula. In particular, two different viscosity ratios have been considered: $\eta_r = 0.1$ and $\eta_r = 0.01$. Results from the simulations are reported in Fig. 2.12; the droplet deformations obtained with the

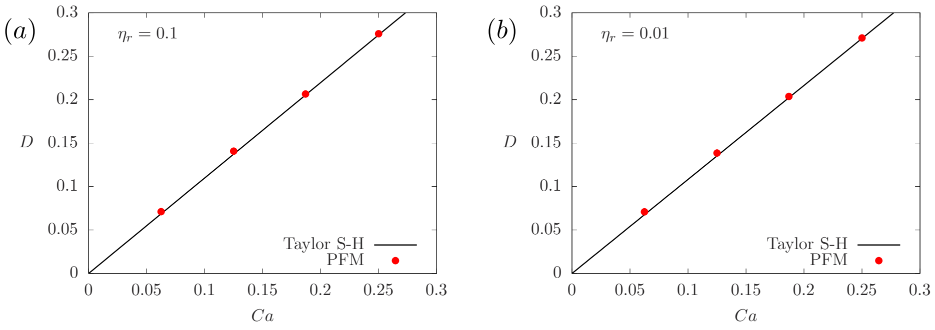

FIGURE 2.12 – Single drop deformation in laminar shear flow, effect of the viscosity ratio. Panel (*a*) refers to $\eta_r = 0.1$, while panel (*b*) refers to $\eta_r = 0.01$. Results from the simulations (PFM) are compared with Taylor formula (Taylor S-H). Corrections from Shapira and Haber are included in Taylor analytic formula.

presented method fall onto the analytic Taylor formula.

2.7.2 Rayleigh-Taylor instability

The Rayleigh-Taylor instability is a fingering instability which arises at the interface between two fluids of different densities [140]. This particular flow instability is frequently found in a number of physical phenomena, ranging from astrophysics, to atmospheric fluid dynamics and cloud physics [12]. The configuration (heavier fluid on top of the lighter one) is unstable and small perturbations at the interface trigger the surface instability, which starts with the formation of fingers. In particular spikes of heavy fluid and bubbles of light fluid will penetrate into the other phase. In archival literature several numerical works investigating the triggering and evolution of the Rayleigh-Taylor instability can be found [31, 40, 54, 59, 157, 170, 171]. The review by Sharp [140] reports a complete picture on analytic, experimental and numerical studies on the topic.

In this section the effect of a different density between the two phases will be validated with the Rayleigh-Taylor instability. Specifically, the position and velocity of spikes and bubbles over time will be compared with widely accepted previous numerical works. Spikes are fingers of heavy fluid falling through the lighter fluid, while bubbles are fingers of light fluid rising through the heavier fluid; Fig. 2.13(*e*) shows an example of a bubble and a spike (red corresponds to the lighter fluid, while blue corresponds to the heavier one).

The present method has been validated against results from He et al. [59] and Wang et al. [170, 171], thus the same configuration used in these works has been adopted. In this benchmark the reference velocity is $u_g = \sqrt{gh}$, where g is the magnitude of the gravity acceleration; gravity is directed downwards (negative z). Using the channel half-height as length scale, the Reynolds number is set to $Re = 724$; this value is different from previous works as here a different length scale has been chosen (other works use the width of the channel, L_y, as length scale). The domain size is $L_y \times L_z = 0.5h \times 2h$ and it has been discretized with $N_y \times N_z = 256 \times 1025$ collocation points. The Cahn number has been set to $Ch = 0.01$ and the Péclet number to

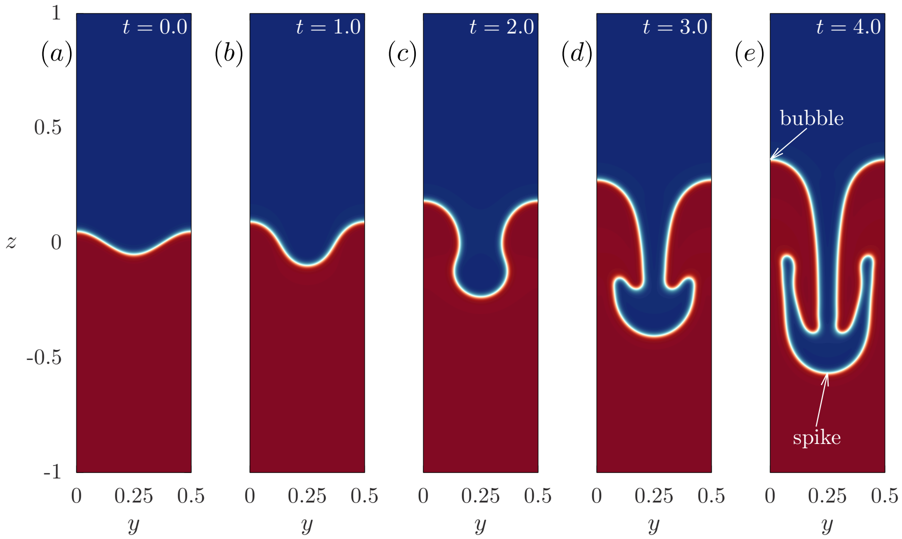

FIGURE 2.13 – Time evolution of the Rayleigh-Taylor instability, time increases from left to right. The heavier fluid (blue) forms a spike that penetrates into the lighter fluid (red). The interface is represented as the thin transition layer between the two phases. The position of the spike and of the bubble is measured over time and compared with previous results.

$Pe_\phi = 1/Ch = 100$. Surface tension is set to zero, thus $We \to \infty$; in the code the calculation of surface forces was switched off to reduce the overall computational cost. Due to the choice of the velocity scale, the Froude number is set to $Fr = 1$. The density ratio between the two phases is $\rho_r = 0.3333$, corresponding to an Atwood number $At = 0.5$.

Fig. 2.13 reports a qualitative view of the time evolution of the Rayleigh-Taylor instability. At the beginning of the simulation, the interface is perturbed with a cosine wave with an amplitude of $0.05h$ and a spatial frequency of $4\pi/h$. This initial perturbation speeds up the triggering of the instability; the same perturbation was adopted by He et al. [59] and Wang et al. [170, 171]. The heavier fluid ($\phi = -1$, blue phase) plunges into the light fluid ($\phi = +1$, red phase) and forms a spike; at the same time the lighter fluid rises in two bubbles at the sides of the spike. Later in time, after $t = 3.0$, the heavy fluid starts to roll up in two side spikes, which further elongates over time. The time evolution of the Rayleigh-Taylor instability is in qualitative agreement with previous reported results for the same parameters. To get a more quantitative comparison, the position and velocity of the bubble and of the main spike are measured over time. These positions are compared against previous numerical results; an excellent agreement among the various methods can be appreciated in Fig. 2.14(a). In addition, the velocity of the interface at the bubble and spike tip is reported in Fig. 2.14(b); the present method accurately follows the benchmark solutions. In the early stages of the simulation ($t < 1$) the perturbation follows an exponential growth; then the bubble reaches a constant velocity and the growth of the perturbation is linear (cruising state). Conversely, after an almost constant velocity stage (ending at about $t = 3.5$), the spike starts to accelerate until the bottom of the domain is reached at about $t = 4.5$ (not

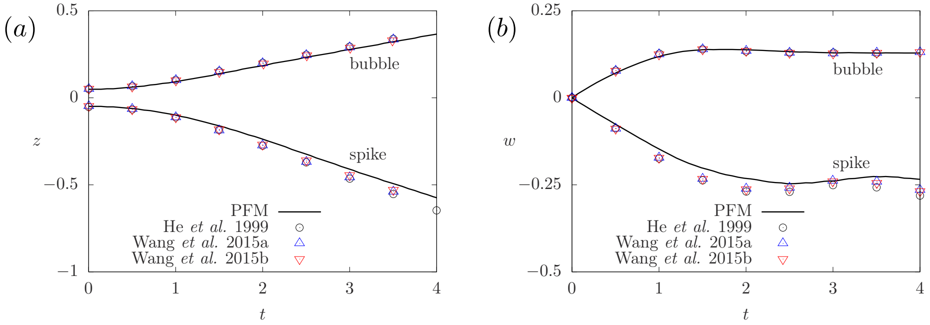

FIGURE 2.14 – Panel (a) compares the results for the spike and tip position from the current method with previous results. Panel (b) compares the results for the spike and tip vertical velocity. The results obtained from the current method (PFM) are compared with results by He et al. [59] (black open circles), Wang et al. [170] (blue upward-pointing triangles) and Wang et al. [171] (red downward-pointing triangles).

shown here).

An excellent agreement with widely accepted results available in archival literature is observed also for the Rayleigh-Taylor benchmark; the present method and its numerical implementation have thus been validated.

3

Mass-conservation-improved Phase Field methods

Reproduced in part from:

G. Soligo, A. Roccon, and A. Soldati, *Mass-conservation-improved phase field methods for turbulent multiphase flow simulation*, Acta Mechanica 230:683–696, 2019.

The phase field method is a powerful tool for the simulation of multiphase flows. In recent years the method has gained increasing popularity due to its sound physical basis, which allows to accurately render physics when using it on a highly refined grid. However, the currently available computational resources introduce a limitation on the grid resolution: in the simulation of turbulent multiphase flows the smallest interfacial scales cannot be resolved, even with modern HPC resources. Indeed, the wide range of scales involved in a multiphase turbulent flow spans form the larger turbulent eddies ($\mathcal{O}(1)$ m), down to the smallest interfacial scales ($\mathcal{O}(1)$ nm), thus covering about nine orders of magnitude in size. The smallest interfacial scales are, indeed, smeared out: a mean-field approximation [90] is adopted. The interface is represented as a finite-thickness transition layer, much larger than a real interface (molecular scale): simulating all the scales, from the problem scale down to the molecular scale is way beyond the capabilities of the current HPC resources. As the smallest interfacial scales are not resolved, some negative effects (namely shrinkage, coarsening and misrepresentation of surface forces and thermo-physical properties), affecting the accuracy of the simulations, arise. Corrected formulations of the phase field method have been proposed to circumvent these drawbacks.

In the following, first, the three issues affecting the classic phase field method will be presented in Sect. 3.1, then two possible corrected formulations, profile-corrected and flux-corrected formulation, will be presented (Sect. 3.2) and benchmarked against the classic formulation (Sect. 3.3).

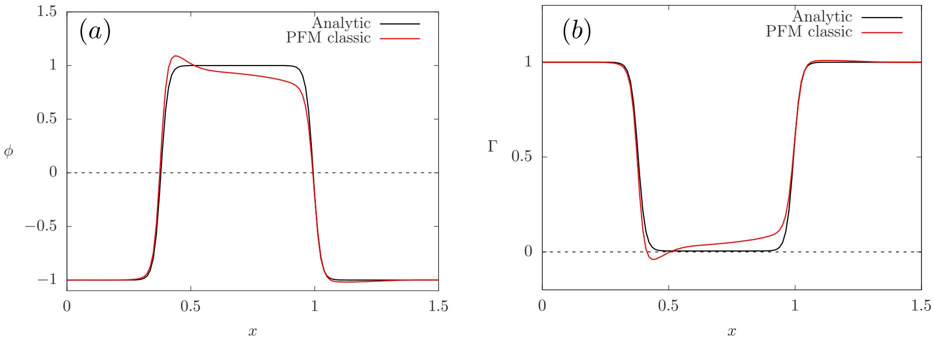

FIGURE 3.1 – Panel (*a*): comparison between the analytic and numeric profile of the phase field. The numeric profile shows an overshoot at the left side and an undershoot at the right side. These overshoots/undershoots influence the representation of thermo-physical properties: panel (*b*) compares the analytic and numeric profiles of a generic thermo-physical property with property ratio $\gamma = 0.005$. Due to the strong overshoot, the thermo-physical property Γ becomes negative.

3.1 Issues of the classic formulation

Shrinkage, coarsening and misrepresentation of surface forces and thermo-physical properties negatively affect the quality of the simulation [78]. Shrinkage and misrepresentation of interfacial forces and thermo-physical properties occur when the interfacial profile deviates from the hyperbolic tangent equilibrium profile; for example, turbulent fluctuations and shear at the interface can perturb the interfacial profile. Surface forces are calculated based on the equilibrium interfacial profile, Eq. (2.13): an out-of-equilibrium interfacial profile introduces an error in the calculation of these forces. Also thermo-physical properties depend on the phase field profile, see Sect. 2.3.1 for further details. Any perturbation of the interfacial profile generates inaccuracies in the local value of these properties; a strong overshoot of the interfacial profile may also lead to negative (unphysical) values of thermo-physical properties, such as density or viscosity. Being γ the ratio of a generic thermo-physical property of the two phases, it is assumed that this thermo-physical property, Γ, is a linear function of the phase field:

$$\Gamma = 1 + \frac{\gamma - 1}{2}(\phi + 1) \ . \tag{3.1}$$

Fig. 3.1 shows an out-of-equilibrium interfacial profile and the relative generic thermo-physical property calculated on that perturbed interfacial profile.

The energy minimization approach, on which the phase field method is based, acts to restore the equilibrium profile: overshoots and undershoots of the interfacial profile are eliminated, originating however another drawback, shrinkage phenomena. Indeed the volume of the phase enclosed by the interface diffuses into the other phase (bulk diffusion), leading to a volume loss of one phase. The total volume is conserved (no-flux and periodic boundary conditions on the phase field), however the volume of each phase is not conserved, as there might be leakages of one phase into the other. These volume leakages are proportional to the interface thickness, thus to the Cahn number; they vanish in the sharp interface limit [108, 183]. The adoption of a logarithmic

potential for the bulk free energy of the phase field free energy functional strictly bounds the interfacial profile between the bulk values and prevents diffusion of one phase into the other outside the interfacial region. However, a logarithmic potential introduces singularities and complicates the numerical resolution, thus a double well potential is usually preferred. Lastly, the coarsening phenomenon is linked to the bulk diffusion of one phase into the other. Shrinkage and coarsening however originate from different causes: coarsening is rooted in the energy minimization approach of the method. To reduce the total interfacial energy, smaller domains enclosed by an interface diffuse (bulk diffusion) into the larger ones, thus reducing the total surface. While shrinkage vanishes in the sharp interface limit, coarsening does not depend on the interface thickness and is still present even for $Ch \to 0$ (sharp interface limit).
Summing up, the phase field drawbacks can be traced back to two main sources: an out-of-equilibrium interfacial profile and bulk diffusion. The corrected formulations act on either of these sources to improve the phase field method.

3.2 Corrected formulations

In the following two corrected formulations will be presented, first the profile-corrected formulation [11, 96] and then the flux-corrected [185] one will be introduced. Each of these formulations acts to circumvent the drawbacks of the classic phase field method.

3.2.1 Profile-corrected Phase Field formulation

The profile-corrected formulation [11, 96] introduces a penalty flux term, f_p, in the phase field transport equation. This penalty flux forces the interfacial profile towards its equilibrium solution, thus reducing the volume leakages among the phases and improving the representation of surface forces and thermo-physical properties.

$$\frac{\partial \phi}{\partial t} + \mathbf{u} \cdot \nabla \phi = \frac{1}{Pe_\phi} \nabla^2 \mu_\phi + f_p \tag{3.2}$$

The penalty flux is defined as:

$$f_p = \frac{\lambda}{Pe_\phi} \left[\nabla^2 \phi - \frac{1}{\sqrt{2}Ch} \nabla \cdot \left((1-\phi^2) \frac{\nabla \phi}{|\nabla \phi|} \right) \right] , \tag{3.3}$$

with λ being a positive constant parameter. Li et al. [96] also proposed a scaling for this parameter based on the Cahn number: $\lambda = \alpha / Ch$. In the following, different values of λ (α) will be tested and benchmarked to investigate the effect of λ and find the optimal choice for this parameter.

3.2.2 Flux-corrected Phase Field formulation

The flux-corrected formulation [185] builds on the profile-corrected one and adds an additional flux, f_f, to this latter formulation.

$$\frac{\partial \phi}{\partial t} + \mathbf{u} \cdot \nabla \phi = \frac{1}{Pe_\phi} \nabla^2 \mu_\phi + f_p + f_f \tag{3.4}$$

This new flux exactly cancels out the component normal to the interface of the diffusive flux produced by the chemical potential:

$$f_f = -\frac{1}{Pe_\phi}\nabla \cdot \left[\left(\nabla\mu_\phi \cdot \frac{\nabla\phi}{|\nabla\phi|}\right)\frac{\nabla\phi}{|\nabla\phi|}\right] . \tag{3.5}$$

The normal to the interface is defined as $\mathbf{n} = \nabla\phi/|\nabla\phi|$ [148]. The flux f_f is the projection on the normal to the interface of the phase field chemical potential gradient. As the diffusive flux normal to the interface has been removed, shrinkage and coarsening phenomena strongly reduce.

3.2.3 Numerical resolution

The newly added fluxes, f_p and f_f, are discretized in time with an explicit Adams-Bashforth scheme. These terms are included in the non-linear term of the phase field equation S_ϕ, Eq. (2.64). The generic penalty flux, f_c, is zero for the classic formulation, while it corresponds to $f_c = f_p$ and to $f_c = f_p + f_f$ for the profile-corrected and flux-corrected formulations respectively.

$$f_c = \begin{cases} 0 & \text{Classic PF formulation} \\ f_p & \text{Profile-corrected PF formulation} \\ f_p + f_f & \text{Flux-corrected PF formulation} \end{cases} \tag{3.6}$$

3.3 Corrected formulations performances

The performances of the corrected phase field formulations have been compared against the classic formulation to benchmark the improvements introduced by the corrections. The effect of the parameter λ (profile-correction penalty flux) has been quantified and an optimal scaling was identified. Three different benchmarks will be presented in the following; each of them is aimed to strongly stress the method. In particular, the capability of each formulation to maintain an interfacial profile as close as possible to the equilibrium profile (thus reducing mass leakages and improving the calculation of surface forces and thermo-physical properties) underwent a severe testing: high shear at the interface (Sect. 3.3.1), interactions among interfaces (Sect. 3.3.2 and Sect. 3.3.3) and turbulent fluctuations (Sect. 3.3.3) were used to perturb the interfacial profile.

3.3.1 Rising bubble

A buoyant bubble (diameter $d = 1$) rising in a vertical two-dimensional (2D) channel is considered for this first benchmark. The sketch of the simulation setup is reported in Fig. 3.2: a 2D circular bubble is initialized at the bottom of the channel. The size of the channel in dimensionless units is $L_y \times L_z = 2\pi \times 2$; periodic boundary conditions are implicitly employed in the y direction, while no-slip conditions are enforced at the two solid walls. The domain has been discretized using $N_y \times N_z = 512 \times 513$ grid points. The Cahn number has thus been set to $Ch = 0.02$, while the phase field Péclet number as been set following the scaling $Pe_\phi = 1/Ch = 50$. The Reynolds number

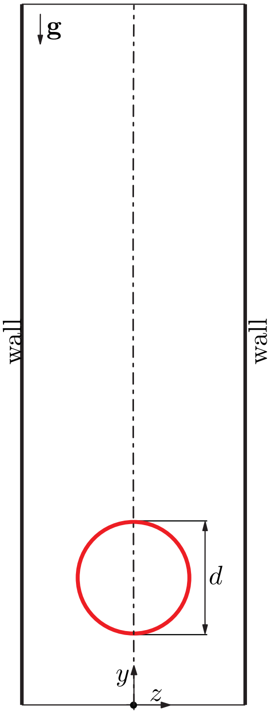

FIGURE 3.2 – Simulation setup for the rising bubble benchmark. A circular bubble with diameter $d = 1$ is released at the bottom of the channel. After its release the bubble, which is lighter than the surrounding fluid, starts rising along the y direction.

has been set to $Re_\tau = 10$, the Weber number to $We = 1$ and the Froude number to $Fr = 0.1$. Three different values of α were selected to calculate the parameter $\lambda = \alpha/Ch$: $\alpha = [0.02\,; 0.05\,; 0.1]$.

At the beginning of the simulation the fluid in the channel is at rest: $\mathbf{u} = 0$. The imposed pressure gradient in the y direction exactly balances the weight of the fluid; the only motion is generated by the density difference among the two phases. The density ratio is set to $\rho_r = 0.1$, while the viscosity ratio is set to $\eta_r = 1$: the two fluids have different density but matched dynamic viscosity. After being released, the bubble starts rising along the y direction; the shear generated by the bubble motion deforms and eventually breaks the interface. This benchmark is extremely challenging, as the strong shear stresses at the interface strongly perturb the interfacial equilibrium profile leading to high mass leakages among the two phases (shrinkage) and to inaccuracies in the calculation of surface forces and thermo-physical properties [182].

Fig. 3.3 shows the time evolution of the droplet for the three different formulations. The results reported in the figure were obtained with $\lambda = 5$ (profile- and flux-corrected formulations). From a macroscopic point of view, the multiphase system evolves similarly over time for the three different formulations: first the droplet strongly deforms due to the strong influence of the wall (no-slip condition), then two elongated tails form and successively break up. Many differences among the corrected formulations

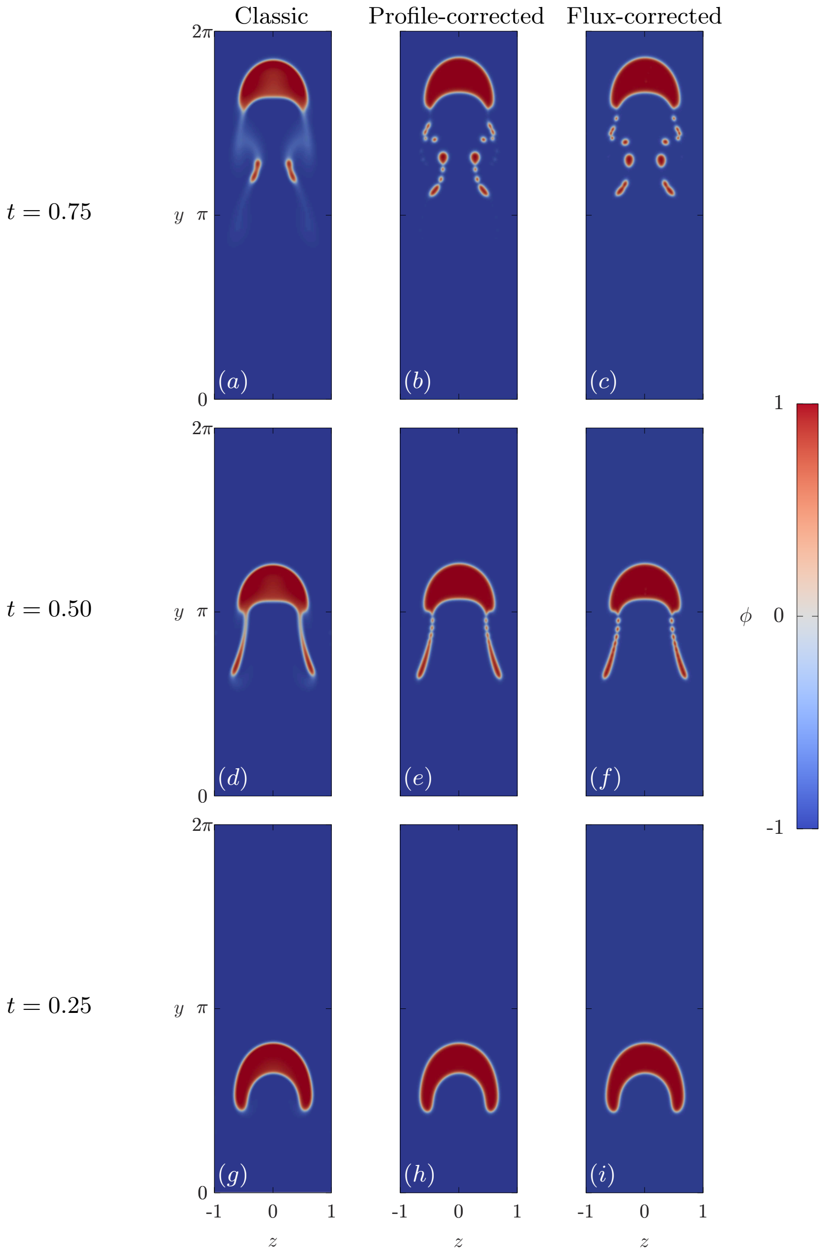

FIGURE 3.3 – Time evolution of the rising droplet; time increases from the bottom to the top, bottom row $t = 0.25$, middle row $t = 0.5$ and top row $t = 0.75$. The leftmost column refers to the classic formulation, the central column to the profile-corrected formulation and the rightmost column to the flux-corrected formulation. For the corrected formulations $\lambda = 5$ was selected.

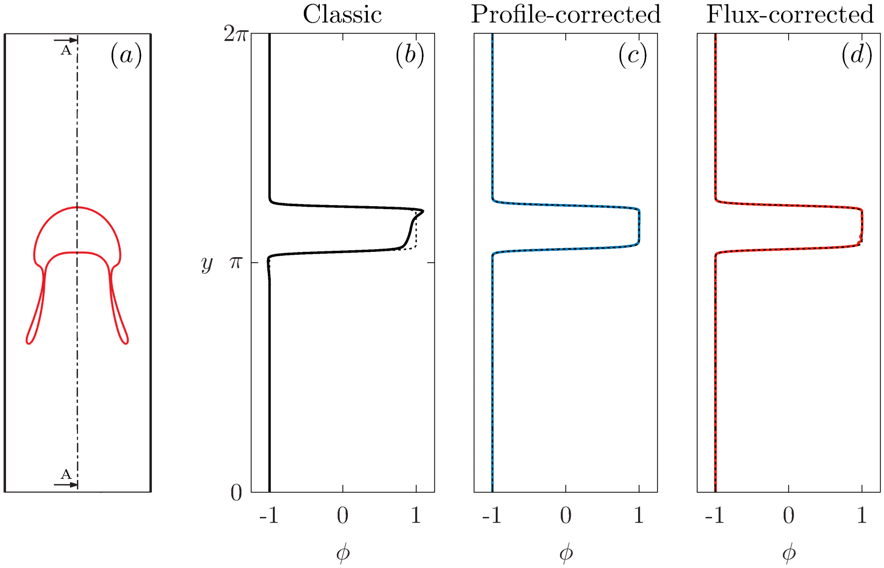

FIGURE 3.4 – Panel (a) shows the generic configuration of the system at $t = 0.5$; panels (b)-(c)-(d) show value of the phase field along the section A-A, dash-dotted line of panel (a). Panel (b) refers to the classic formulation, panel (c) to the profile-corrected formulation ($\lambda = 5$) and panel (d) to the flux-corrected-formulation ($\lambda = 5$). The equilibrium solution is reported for reference with a thin dashed line. The classic formulation exhibits strong overshoots and undershoots, while the corrected formulations well preserve the equilibrium profile.

and the classic one can be noticed in the later stages of the simulation: the interfacial profile and the topology of the tails is substantially different. In the initial part of the simulation, panels (g)-(h)-(i), the three formulations evolve in the same way: the initially circular droplet starts rising and deforms according to the imposed no-slip boundary conditions at the walls.

Starting from the classic formulation, some undershoots (light red regions) and overshoots (dark red regions) in the phase field can be observed already at $t = 0.5$: an overshoot can be seen at the bubble front and an undershoot at the bubble back. These perturbations can be better appreciated in Fig. 3.4, in which the phase field profiles along the channel center-line are plotted for all the three formulations. As the bubble increases its rising velocity the tails further elongate and detach from the main body of the bubble. The tails then undergo further breakages, generating smaller droplets which shrink and dissolve into the bulk phase (light blue region). This benchmark thus immediately exposes the shrinkage phenomenon (shrinkage and diffusion of the tails) and the misrepresentation of surface forces and thermo-physical properties. On the other hand, both corrected formulations well preserve the interfacial profile and strongly limit shrinkage phenomena: after the formation and detachment of the tails from the bubble main body, the smaller droplets are conserved. The flux-corrected formulation shows small fluctuations in the phase field at the back of the bubble, see Fig. 3.4 panel (d). Small differences between the corrected formulations can however be appreciated in the morphology of the detached droplets: at $t = 0.75$ the droplets are slightly larger and already underwent coalescence in the flux-corrected formula-

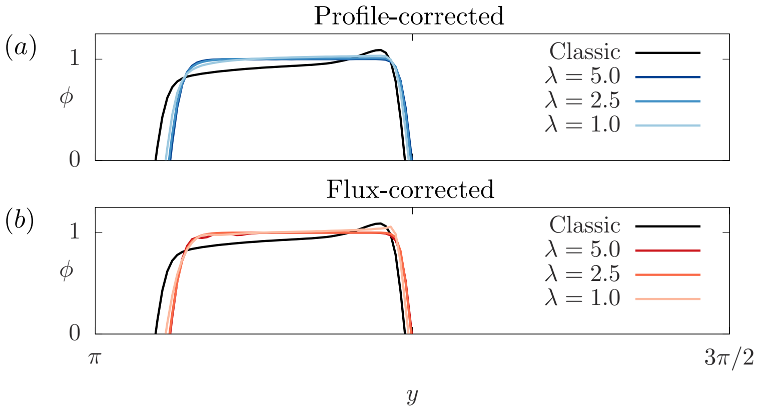

FIGURE 3.5 – Detail of the instantaneous phase field profile along the channel centerline (y axis) at $t = 0.5$ for the three different values of λ. Panel (a) reports the results for the profile-corrected formulation, while panel (b) for the flux-corrected one. The phase field profile obtained with the classic formulation is shown for reference. The parameter λ determines the efficacy of the profile correction: reducing its value, the classic formulation is recovered.

tion. This effect can be traced back to the additional flux, f_f, in the flux-corrected formulation.

Then, the effect of the parameter $\lambda = \alpha/Ch$ is investigated for both corrected formulations. Three different values of α have been selected: $\alpha = [0.02\ ; 0.05\ ; 0.1]$, corresponding respectively to $\lambda = [1\ ; 2.5\ ; 5]$. Fig. 3.5 shows a detail of the phase field profile across the bubble for both corrected formulations and different values of the parameter λ. For the profile-corrected formulation, the parameter λ has a limited influence on the interfacial profile: at the lowest λ value a small overshoot at the bubble front and a small undershoot at the bubble back appear. Reducing λ reduces indeed the efficacy of the correction term. Similarly, the flux-corrected case at the lowest λ shows an overshoot at the bubble front, but it is more uniform at the bubble back. For high values of λ small fluctuations appear in the bulk bubble phase. For the flux-corrected formulation, $\lambda = 2.5$ thus shows the best performances in keeping the equilibrium interfacial profile.

The phase leakages for all the different cases have been quantified by measuring the total volume of the bubble phase during the entire simulation. For the classic simulation at $t = 1$ about 12% of the bubble volume diffused into the other phase; most of the leakages occurs during the shrinkage of the small droplets in the tails of the bubble. The corrected formulations strongly improve the conservation of the bubble volume: with $\lambda = 5$ the leakages amount to about 4% of the initial volume for the profile-corrected formulation and to about 2.5% for the flux-corrected one. Decreasing the value of λ the volume leakages increase: 5% ($\lambda = 2.5$) and 8% ($\lambda = 1$) for the profile-corrected formulation and 3% ($\lambda = 2.5$) and 3.5% ($\lambda = 1$) for the flux-corrected one.

The corrected formulations proved to be effective in maintaining the interfacial profile close to the equilibrium solution and in better conserving the total volume of each phase. As already stated, this benchmark is rather challenging as the high shear at

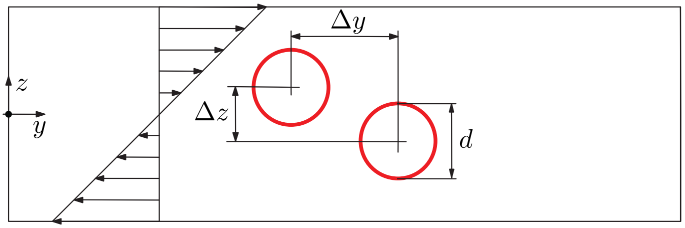

FIGURE 3.6 – Simulation setup used to investigate the effect of the added fluxes on a coalescence event. The imposed shear flow makes the droplets collide. The droplets have diameter $d = 0.7$ and are placed at $y_c = \pi \mp 0.5$ and $z_c = \pm 0.25$ ($\Delta y = 1$, $\Delta z = 0.5$).

the interface and the small droplets in the bubble tails enhance shrinkage phenomena [182]. For the profile-corrected formulation, the parameter λ mostly affected shrinkage phenomena (equilibrium profile kept for all values of λ tested), while for the flux-corrected one it had also a considerable effect on the conservation of the phase field profile (overshoots/undershoots and fluctuations).

3.3.2 Droplet-droplet interaction

As the implicit and accurate description of topological changes is one of the main advantages of the phase field method, the effect of the corrected formulations on a coalescence event has been investigated. The simulation setup is reported in Fig. 3.6: two 2D droplets are placed at $y_c = \pi \mp 0.5$, $z_c = \pm 0.25$ (center position). The imposed shear flow drives the two droplets towards, first, collision and, then, coalescence. The channel dimensions are $L_y \times L_z = 2\pi \times 2$ (discretized with $N_y \times N_z = 512 \times 513$ grid points); the two walls at $z = \pm 1$ move in opposite directions with $v_w = \pm 1$. The initial flow field is a linear profile, $v(z) = z$; the Reynolds number is calculated using the velocity of the wall, v_w, and has been set to $Re = 0.5$. The other two components of the velocity are initially set to zero. The two phases have the same density ($\rho_1 = \rho_2$) and viscosity ($\eta_1 = \eta_2$). Gravity has been neglected as there are no density differences. Given the grid resolution, a Cahn number $Ch = 0.02$ has been chosen; the Péclet number has been thus set to $Pe_\phi = 1/Ch = 50$. The Weber number was set to $We = 1.5$. Again, the effect of the parameter λ was tested: three different values were tested, $\lambda = [1\ ; 2.5\ ; 5]$.

Fig. 3.7 show the time sequence of the coalescence event: after an initial approaching stage, $t = 2.0$, the two droplets start interacting. At this stage almost no differences can be appreciated among the different formulations: the droplets simulated with the classic formulation are slightly smaller as some small mass leakages already occurred. Starting from $t = 2.2$ the effects of the additional fluxes can already be appreciated: the corrected formulations anticipate the coalescence event. This effect can be traced back to two causes: the droplets are slightly larger (lower leakages among the phases, 2% for the classic formulation and about 0% for the corrected ones) and the additional fluxes accelerate the coalescence [185]. The following panels show the completion of the coalescence event: as soon as the interfaces overlap, the droplets merge and, then, surface tension forces reshape the newly formed droplet. As the coalescence event

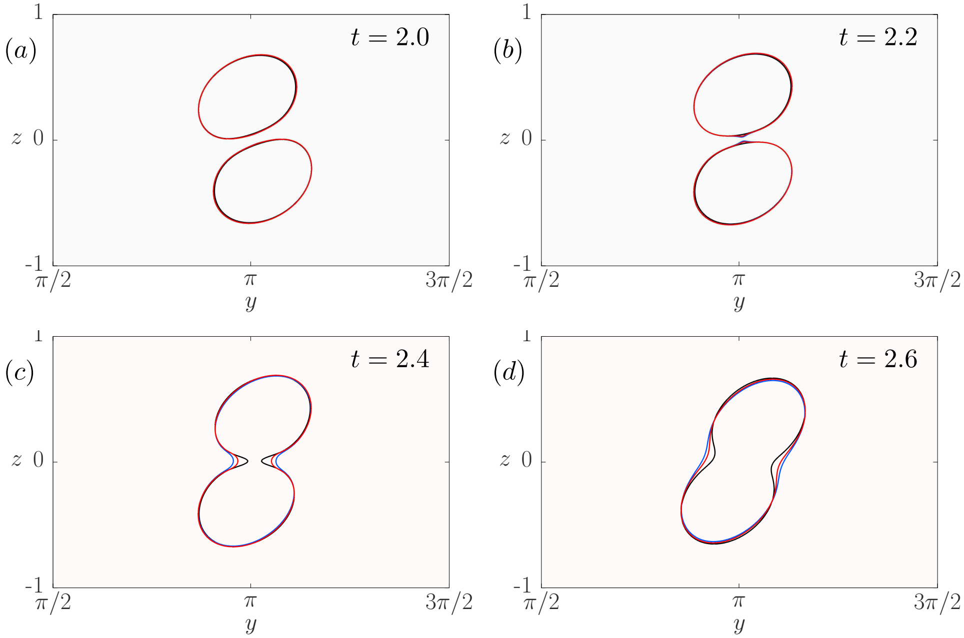

FIGURE 3.7 – Time sequence of the coalescence event: panels (a) to (d) refer respectively to $t = 2.0$, $t = 2.2$, $t = 2.4$ and $t = 2.6$. The interface is identified by the contour line $\phi = 0$. The results for the three formulations are reported in black (classic formulation), blue (profile-corrected, $\lambda = 5$) and red (flux-corrected, $\lambda = 5$).

took place earlier for the corrected formulations, the subsequent evolution for these formulations is slightly anticipated. The flux-corrected formulation undergoes the interface merging later than the profile-corrected formulation; indeed, the lack of the chemical potential gradient diffusive flux normal to the interface slightly delays the coalescence.

The effect of the parameter λ on the coalescence dynamics has been then investigated. Fig. 3.8 shows a detailed view of the coalescence process, right before ($t = 2.2$) and after ($t = 2.4$) the merging of the interfaces. For the sake of clarity only two values of λ have been reported: $\lambda = 5$ (blue and red contour lines) and $\lambda = 1$ (cyan and orange lines). The classic formulation has also been reported for reference (solid black line). For the profile corrected formulation, the effect of the parameter λ is clear: increasing its value anticipates the coalescence event. For $\lambda = 1$ the interface shape almost falls back onto that obtained with the classic formulation. Indeed, the parameter λ determines the strength of the penalty flux: for small values of λ the classic formulation is recovered. Panels (c) and (d) show the snapshots of the coalescence event for the flux-corrected formulation. For the highest value of λ the coalescence is anticipated with respect to the classic formulation. Reducing the values of λ, the merging of the interfaces is delayed; for $\lambda = 1$ (lowest value) coalescence occurs after the merging of the interfaces in the classic formulation.

Thus, stronger correction fluxes, corresponding to high values of the parameter λ, an-

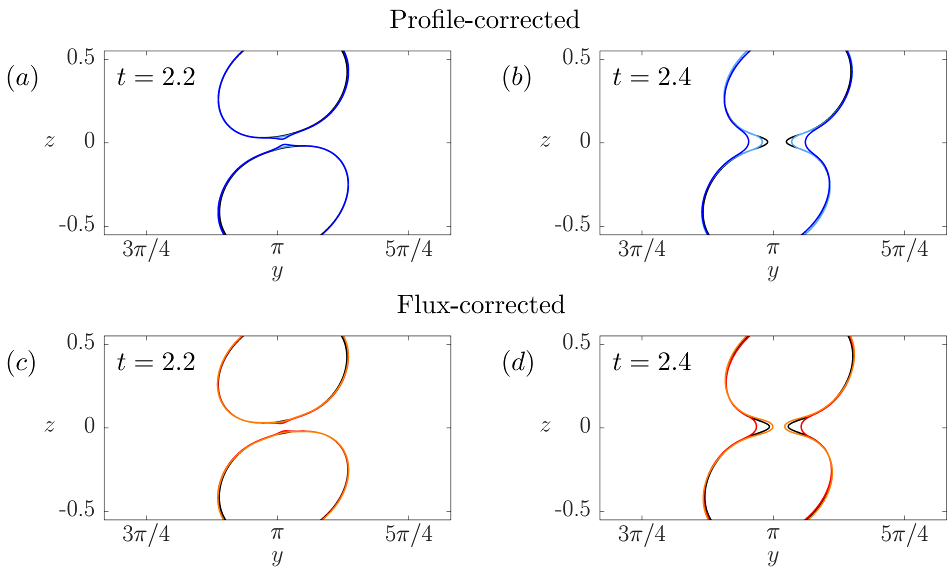

FIGURE 3.8 – Detail of the coalescence event, before ($t = 2.2$) and after ($t = 2.4$) the merging of the interfaces. The top row reports the results for the profile-corrected formulation, while the bottom row those for the flux-corrected one. The classic formulation has been reported for reference with a solid black line. For the sake of clarity only two values of λ have been reported, the highest, $\lambda = 5$, and the lowest, $\lambda = 1$. For the profile-corrected formulation blue lines report the results at $\lambda = 5$, while cyan lines those at $\lambda = 1$; for the flux-corrected formulation red lines show the results at $\lambda = 5$, while orange lines those at $\lambda = 1$.

ticipate the coalescence event: the magnitude of the penalty flux, f_p, is proportional to λ. The effect of the penalty flux is mitigated by the absence of the wall-normal component of the chemical potential flux: coalescence is slightly delayed for the flux-corrected formulation. From the shrinkage point of view, the classic formulation experiences about 2% of leakages among the phases, while in the corrected formulation the leakage is negligible.

3.3.3 Shrinkage in wall-bounded turbulence

The last benchmark consists in the simulation of a swarm of large and deformable droplets in wall-bounded turbulence. A closed channel configuration has been selected, as reported in Fig. 2.6; this configuration is characteristic of multiphase problems of industrial or environmental interest. The previous benchmarks showed that better performances can be obtained with the scaling $\lambda = 0.05/Ch$: shrinkage is limited and interface topological changes are relatively unaffected. As the problem is highly complicated, the effect of the additional fluxes on the interface topological changes was not investigated; however, the dispersed phase (droplets) shrinkage was investigated over time.
An array of 256 spherical droplets (diameter $d = 0.4$) is initialized in a fully-developed turbulent channel flow ($Re_\tau = 300$) at the beginning of the simulation. The droplets and the carrier fluid have the same density and viscosity; gravity was neglected. The channel has dimensions $L_x \times L_y \times L_z = 4\pi \times 2\pi \times 2$; periodic boundary conditions are

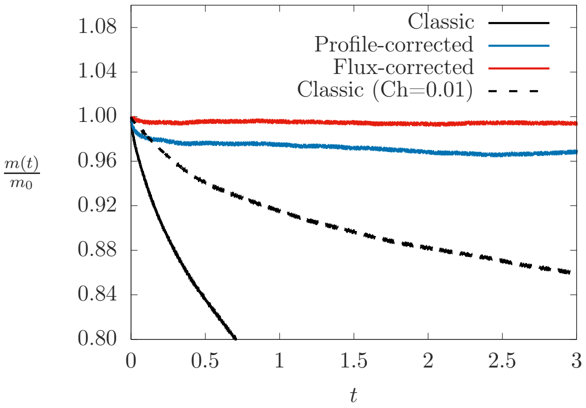

FIGURE 3.9 – Time evolution of the total mass of the droplets, $m(t)$, normalized by its initial value, m_0. The three solid lines correspond to the classic formulation (black), the profile-corrected (blue) and flux-corrected (red). A simulation with an halved Cahn number on a refined grid was also performed for the classic formulation (dashed black line).

applied along the x and y direction, while no-slip boundary conditions are enforced at the walls. $N_x \times N_y \times N_z = 512 \times 256 \times 513$ grid points are used; this grid resolution allows for an accurate description of all flow scales. Given the grid resolution, a Cahn number $Ch = 0.02$ was selected; the Péclet number was set to $Pe_\phi = 50$. An additional simulation was also run with a finer grid (double the resolution along each direction) and $Ch = 0.01$ to investigate the shrinkage for the classic formulation. The Weber number, representative of the importance of surface forces, was set to $We = 1.5$. The parameter $\lambda = 2.5$ has been selected based on the chosen scaling, $\lambda = 0.05/Ch$.

After their initialization, droplets move with the surrounding fluid; turbulent fluctuations shift and deform the droplets. Eventually, turbulent fluctuations can drive droplets towards collision and coalescence. At earlier stages of the simulation the droplets do not interact with each other and just deform; later on turbulence leads to coalescence and breakage events. The time evolution of the total mass of the droplets normalized by its initial value is reported in Fig. 3.9. The turbulent fluctuations strongly perturb the interfacial profile from its equilibrium, leading to a consistent bulk diffusion and thus to the shrinkage of the dispersed phase. Conversely, the corrected formulations are able to keep the equilibrium profile and achieve an almost constant dispersed phase mass. The total mass of the droplets reduces of about 0.5% for the flux-corrected formulation and 2.5% for the profile-corrected formulation. It must however be noted that after an initial shrinkage, the profile-corrected formulation keeps the total droplets mass constant ($t > 1$). This initial sudden shrinkage is generated by the initial conditions chosen: a regular array of droplets is suddenly inserted in a single phase fully-developed turbulent flow field. During the initial stage of the simulation the flow field has to couple with the phase field and the interfacial profile is strongly perturbed. An additional simulation has been performed on a twice as fine grid, $N_x \times N_y \times N_z = 1024 \times 512 \times 1025$, with the classic formulation. For this latter case an halved Cahn number, $Ch = 0.01$, has been used. The magnitude of shrinkage is proportional to the Cahn number, thus a better mass conservation for the dispersed phase is expected. Even though a lower Cahn number has been employed, the corrected formulations still outperform the classic formulation. The better performances of the corrected formulations together with the lower computational cost (a better dispersed phase mass conservation can be achieved on a coarser grid) make the corrected formulations an appealing option.

3.4 Conclusions

In this chapter three different phase field formulations have been tested and benchmarked: the classic, the profile-corrected and the flux-corrected formulation. The drawbacks of the classic phase field method have been exposed and stressed in three different benchmarks and the performances of each formulations have been evaluated. The corrected formulations are able to preserve the phase field equilibrium profile, thus improving the representation of thermo-physical properties and the calculation of surface tension forces. In addition, maintaining the equilibrium profile helps in reducing shrinkage phenomena. The benchmarks also allowed to identify an optimal scaling for the parameter $\lambda = 0.05/Ch$, such that shrinkage is strongly reduced and interface topological changes are not affected by the additional fluxes.

In the following, all simulations will be performed using the profile-corrected formulation with $\lambda = 0.05/Ch$; this formulation has been selected over the flux-corrected one as it achieves similar performances with limited modifications with respect to the classic phase field formulation.

4

Comparison of 2D vs 3D droplet deformation

Reproduced in part from:

G. Soligo, A. Roccon, and A. Soldati, *Coalescence of surfactant-laden drops by Phase Field Method*, Journal of Computational Physics 376:1292–1311, 2019,

and

G. Soligo, A. Roccon, and A. Soldati, *Deformation of clean and surfactant-laden droplets in shear flow*, Meccanica (in press), 2019.

Quantifying the deformation of a droplet in a laminar shear flow is important in many industrial applications and biological systems, among which emulsifying devices [99], polymer blending [53], oil recovery [111], formation and rheology of emulsions [37] and the study of red blood cells [177]. Taylor, in his pioneering works [153, 154], developed an analytic formula capable of quantifying the deformation of a droplet in the limit of negligible inertial effects (low Reynolds number) and small drop deformation. Within these hypothesis, Taylor analytic formula can predict the steady-state deformation of a droplet as a function of the capillary number, Ca, and of the viscosity of the two phases (droplet and carrier liquid). The capillary number is a dimensionless quantity that defines the importance of viscous effects over surface tension forces. Indeed, when inertial effects are negligible, the deformation of a droplet is determined by the competition of viscous and surface tension forces: the shear rate tries to deform the droplet, while surface tension restores the minimal energy configuration of the interface (sphere for three-dimensional droplets, circle for two-dimensional ones). The original Taylor analytic formula has been later corrected by Shapira and Haber [139], who considered the confinement effect due to the presence of walls on the droplet deformation. The correction factor introduced depends only on the ratio between the droplet size and the distance from the walls.

Being a simple and easy to reproduce setup, the measurement of the deformation of a droplet in laminar shear flow is now a well-assessed benchmark used to validate numerical methods and calibrate experimental facilities. Taylor analytic formula [153, 154], together with Shapira and Haber correction [139], has been widely used to benchmark and validate numerical methods and codes for multiphase flows [67, 145, 150, 166, 181, 186]. For validation purposes, a fast and lightweight simulation is always preferable; indeed, two-dimensional (2D) simulations are often preferred to their three-dimensional (3D) counterpart when performing validation tests and benchmarks. However, for the droplet deformation benchmark, 2D and 3D cases are substantially different: the former are circular droplets (cylindrical when extended to 3D), while the latter are spherical droplets. These different interfacial shapes will undergo a different deformation, even at the same capillary number. Thus, reducing a 3D case to a 2D one is a drastic simplification, in which several physical effects are strongly affected (suppression of capillary instabilities, longer and stronger near-contact droplet interaction), but other main effects are still kept (development of high interfacial curvature regions, tip streaming) [187]. Zhou and Pozrikidis [187] presented a first comparison on the deformation of 2D and 3D droplets and they found that 2D and 3D droplets exhibit a similar behavior. Later on, Tang et al. [152] confirmed this result.

This chapter is devoted to the investigation of the limits of Taylor analytic formula: first, the deformation of clean 2D and 3D droplets will be computed and compared, then, the effects of a dissolved surfactant and of the different problem dimensionality on the surfactant distribution will be investigated. The different deformation of 2D and 3D droplets can be traced back to the shrinkage of the droplets in the direction normal to the velocity-velocity gradient plane: in the limit of small deformations, the shrinkage of the droplet along this direction is limited, thus 2D and 3D droplets do experience similar deformations at low capillary numbers. In particular, previous analyses and comparisons among 2D and 3D droplet deformation [1, 152, 187] will be further extended and the limits of applicability of Taylor analytic formula will be tested. The different dimensionality of the problem (2D *vs* 3D) has also important effects on the surfactant distribution and, thus, on Marangoni stresses (stresses acting tangentially to the interface, whenever a surface tension gradient is present). In addition, surfactant also modifies the droplet deformation: (*i*) surfactant reduces surface tension, thus leading to a lower average surface tension over the interface, (*ii*) the imposed external shear stresses accumulate surfactant at the droplet tips, further reducing the local surface tension, and (*iii*) the non-uniform surfactant distribution generates Marangoni stresses along the interface, modifying the local stresses acting on the interface. Numerical simulations allow to separately pinpoint each of these factors and to analyze their effect on the deformation of the droplet separately. In particular, the average surface tension reduction produced by the surfactant accounts for most of the droplet deformation. As a consequence, Taylor analytic formula can be used to compute the deformation of surfactant-laden droplets if the capillary number is rescaled with the lower average surface tension over the interface.

4.1 Simulation setup

The computational setup adopted to simulate the deformation of a droplet in laminar shear flow is sketched in Fig. 4.1: a closed channel setup with two moving walls (top wall moves with velocity u_w, while the bottom wall with velocity $-u_w$). A single droplet, spherical for 3D cases and circular for 2D cases, is initialized at the

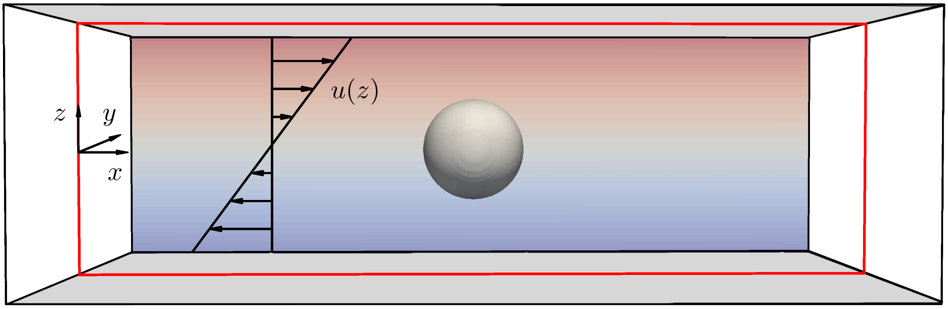

FIGURE 4.1 – Sketch of the computational domain used to analyze the deformation of a single droplet in shear flow. The domain has dimensions $L_x \times L_y \times L_z = 2\pi h \times \pi h \times 2h$ for the 3D simulations and $L_x \times L_z = 2\pi h \times 2h$ for the 2D simulations (red rectangle). A spherical droplet (circular for the 2D simulations) is initialized in the centre of the channel ($x_c = \pi h$, $y_c = \pi h/2$, $z_c = 0$). The two walls, located at $z = \pm h$ and represented in grey, move in opposite directions with constant velocity $u = \pm u_w$.

channel centre. When considering 2D cases a $x - z$ plane is considered (red rectangle in the sketch of the simulation setup). At the beginning of the simulation a linear velocity profile $u = z/h$ is initialized in the x direction; in the other two directions the fluid velocity is set to zero. The computational domain has dimensions $L_x \times L_y \times L_z = 2\pi h \times \pi h \times 2h$ ($L_x \times L_z = 2\pi h \times 2h$ for 2D cases) and the droplet diameter is $d = 0.8h$. The computational domain is discretized with $N_x \times N_y \times N_z = 512 \times 256 \times 513$ grid points ($N_x \times N_z = 512 \times 513$ for 2D cases). A uniform grid spacing is adopted in the homogenous directions (x and y, Fourier discretization), while Chebyshev nodes are used for the wall-normal direction (z). The interface thickness, set via the Cahn number, is 1.25% of the channel height, resulting in a Cahn number $Ch = 0.025$. This value allows to properly resolve the interface and the surfactant concentration at the interface with the current grid resolution: a minimum of about 5 grid spacings is required to correctly capture the phase field, the surfactant concentration and their steep gradients. The Péclet number for the phase variable is set to $Pe_\phi = 3/Ch = 120$, according to the scaling proposed by Magaletti et al. [108]. Concerning the surfactant parameters, the surfactant Péclet number is set to $Pe_\psi = 100$, the temperature dependent parameter to $Pi = 1.689$ and the solubility number to $E_x = 0.1$ [47]. With this value of the surfactant Péclet number, diffusive phenomena act on a much larger timescale than convective phenomena. A moderate strength surfactant has been selected for the surfactant-laden cases, $\beta_s = 0.5$. To test the influence of the total amount of surfactant, the surfactant bulk concentration was varied from $\psi_b = 0$ (clean system) up to $\psi_b = 0.02$ (high surfactant loading). To verify the hypothesis of negligible inertial effects the Reynolds number has been set to $Re = \rho u_w h/\eta = 0.1$; both fluids (droplet and carrier) have the same density and viscosity. Different capillary numbers have been tested in the small deformation regime (low capillary numbers); a total of three different values has been chosen.

A recap of the simulations performed is reported in Tab. 4.1; for each surfactant bulk concentration–capillary number couple, one 2D and one 3D simulations were

TABLE 4.1 – List of the simulations performed; letters define the surfactant loading (C: clean, L: low and H: high), while numbers indicate increasing capillary numbers (1: $Ca = 0.062$, 2: $Ca = 0.125$ and 3: $Ca = 0.187$).

	$Ca = 0.062$	$Ca = 0.125$	$Ca = 0.187$
Clean ($\psi_b = 0$)	C1	C2	C3
$\psi_b = 0.01$	L1	L2	L3
$\psi_b = 0.02$	H1	H2	H3

performed. An additional simulation ($Ca = 0.187$ and $\psi_b = 0.01$, case L3) has been performed to better understand the effects introduced by a surfactant. In particular, this latter simulation neglects Marangoni stresses: surface tension is still free to change along the interface, but surface tension gradients do not generate Marangoni stresses. This way, the importance of Marangoni stresses on the droplet deformation and on the surfactant distribution can be sorted out. Marangoni stresses can be turned off by removing the component tangential to the interface of the surface forces term in the Navier-Stokes equation:

$$\frac{3}{\sqrt{8}}\frac{Ch}{We}\nabla\cdot[\overline{\tau}_c f_\sigma(\psi)] = \frac{3}{\sqrt{8}}\frac{Ch}{We}\left[\underbrace{\nabla\cdot\overline{\tau}_c f_\sigma}_{\text{Normal}} + \underbrace{\overline{\tau}_c\nabla f_\sigma}_{\text{Tangential}}\right]. \tag{4.1}$$

4.2 Droplet deformation parameter

The deformation of a droplet is defined as a function of its major and minor axes in the velocity-velocity gradient plane. Fig. 4.2 reports a sketch of a deformed droplet, showing the three axes a (major axis of deformation), b (minor axis of deformation) and c (third axis, normal to velocity-velocity gradient plane). The Taylor deformation parameter is defined as:

$$D = \frac{a-b}{a+b}\,. \tag{4.2}$$

Taylor deformation parameter thus considers only two axes of the droplet, a and b; this deformation parameter can be easily computed also from experimental data, as it requires only the measurement of two axes. In the limit of validity of Taylor analytic formula (limited inertial effects and small droplet deformation), the droplet never undergoes breakage and it always attains a steady-state shape: surface tension forces balance out the shear stresses. The capillary number, Ca, defines the competition of these two factors: it is defined as the ratio of viscous over surface tension contributions.

$$Ca = \frac{\eta u_w}{\sigma_0}\frac{d}{2h} \tag{4.3}$$

Indeed, Taylor formula computes the steady-state deformation of a droplet as a linear function of this dimensionless number. Taylor deformation for fluids having the same viscosity is:

$$D = \frac{35}{32}Ca\,. \tag{4.4}$$

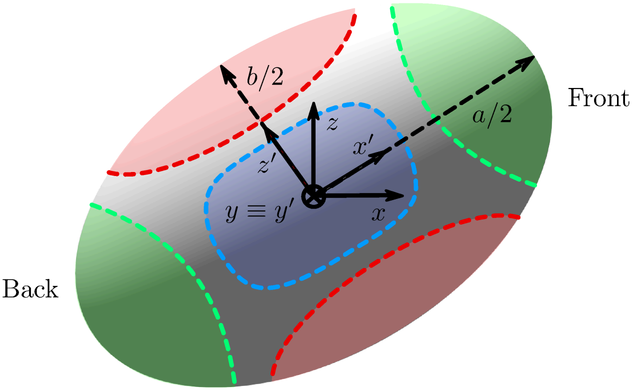

FIGURE 4.2 – The final steady-state shape of the droplet can be characterized by the length of the three principal axes: the major axis of deformation, a, the minor axis of deformation, b, and the third axis, c. The latter one is aligned with the y direction and is thus not shown in this sketch. An additional reference frame (x', y', z') is defined, with the axes corresponding to the deformed droplet principal axes. The different regions of the droplet have been also highlighted for ease of reference: tips (green), belly (red) and sides (blue).

Eventual viscosity contrasts among the two phases only modify the slope: the 35/32 coefficient is specific for matched-viscosity phases. In the more general formulation the slope is a function of the viscosity of each phase. A multiplicative factor can be included to consider the confinement effect brought in by the presence of the two walls. Following the work of Shapira and Haber [139], the actual formula that will be used here to compute the deformation parameter is:

$$D = \frac{35}{32} Ca \left[1 + C_{SH} \frac{3.5}{2} \left(\frac{d}{4h} \right)^3 \right] , \qquad (4.5)$$

where C_{SH} is a numerical coefficient, $C_{SH} = 5.6996$. The confinement effect is accounted for in the ratio of the droplet radius, $d/2$, over the total channel height, $2h$.

4.3 Clean droplets

In this section the deformation parameter for the clean droplets, simulations C1 to C3 (increasing capillary numbers), will be computed and compared with previous analytic [139, 154] and numerical results for both 2D and 3D cases. In the second part, the deformation of each axis will be measured and compared with the predictions of Taylor formula.

4.3.1 Droplet deformation

The time evolution of the droplet deformation parameter, D, has been computed for all the clean cases (C1, C2 and C3) and it is reported in Fig. 4.3. Dashed lines identify the

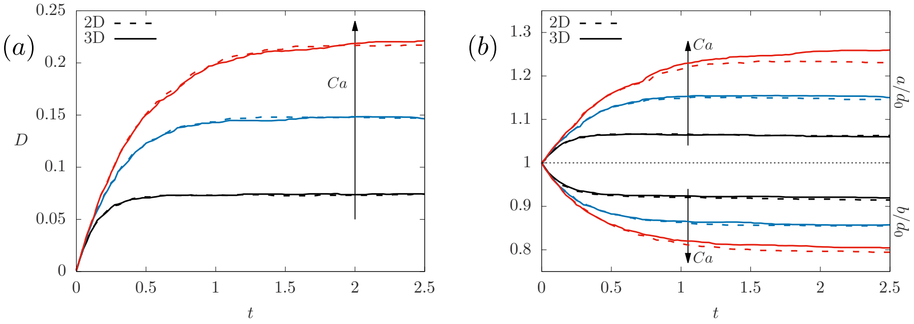

FIGURE 4.3 – Panel (a): time evolution of the deformation parameter D for the different cases. The droplet is initially spherical (circular in 2D simulations) and thus $D = 0$. Then, the shear flow starts to deform the droplet until a new steady-state shape is achieved. Increasing the capillary number, Ca, the droplet deformation increases and a longer time is required to reach the final configuration. Panel (b): time evolution of the major, a, and minor, b, axes normalized by the initial droplet diameter, d_0. In both panels the different colors identify the various capillary numbers: $Ca = 0.062$ (black), $Ca = 0.125$ (blue) and $Ca = 0.187$ (red), while different line styles distinguish 2D (dashed lines) from 3D (solid lines) cases. Time, t, is made dimensionless using the shear rate, u_w/h.

results obtained for 2D cases, while solid lines identify those obtained for 3D cases. At the beginning of the simulation the droplet is spherical (circular for 2D cases), therefore $D = 0$ ($a = b$). Then the imposed shear stresses (the two moving walls generate a Couette-like flow) start to deform the droplet until a steady-state shape is reached at the end of the transient. The time required to attain the steady-state deformation increases with the capillary number: more deformable droplets (higher Ca) require a longer transient before the steady-state shape is reached. In the limit of small deformation (low Ca), 2D and 3D deformation parameters well match each other for each capillary number. Even though 2D and 3D droplets have matching deformation parameters for the entire time span of the simulation, cylindrical and spherical droplets do deform in a different way. In particular, Fig. 4.3(b) shows the time evolution of the major and minor axes of deformation, a and b, normalized by the initial droplet diameter, d_0. For increasing capillary numbers the two axes of deformation start to differentiate between 2D and 3D cases: this difference becomes clear at the highest capillary number tested, $Ca = 0.187$. In particular, the major axis of 3D droplets elongates more than its 2D counterpart, generating a more elongated droplet (see Fig. 4.4). On the other hand, 3D droplets undergo a lower compression along the minor axis of deformation, b with respect to the 2D cases. Thus, for 3D droplets the longer major axis is balanced by a longer minor axis, thus resulting in an overall similar deformation parameter between 2D and 3D cases in the limit of low capillary numbers. As the capillary number is increased (see the case at $Ca = 0.187$), it can be noticed that the major axis of deformation for 3D droplets elongates much more than its 2D counterpart, while the minor axis has a similar length in both cases. This difference results then in an increased deformation for 3D droplets for increasing capillary numbers. This feature can also be appreciated in Fig. 4.4, in which the steady-state droplet shape is compared for different capillary numbers and problem

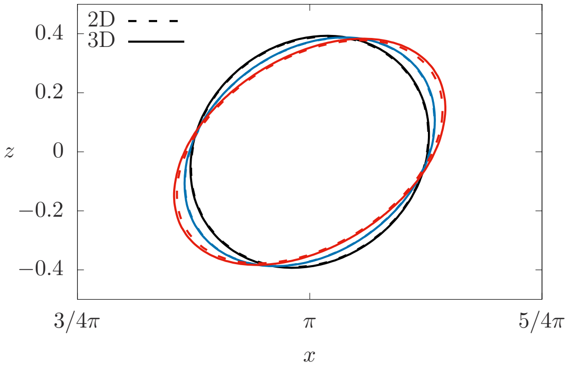

FIGURE 4.4 – Comparison of the steady-shape of the droplet obtained from 2D simulations (dashed lines) and 3D simulations (solid lines) on a $x - z$ plane located at $y = L_y/2$. Different colors distinguish the various capillary numbers: $Ca = 0.062$ (black), $Ca = 0.125$ (blue) and $Ca = 0.187$ (red). The 3D cases experience a higher deformation with respect to their 2D counterpart. Indeed the shrinkage of the third axes c largely contributes to droplet deformation. This difference is more pronounced for the larger capillary number considered, $Ca = 0.187$.

dimensionality. At the lower capillary numbers ($Ca = 0.062$ and $Ca = 0.125$) the cross sections of the deformed droplets fall on top of each other; however, at the highest Ca the 3D droplet major axis elongates more with respect to the 2D case, but the minor axes are almost of the same length. This results in a higher deformation parameter at high capillary numbers for 3D droplets.

The numerical results presented so far have also been compared with previous works. In particular the steady-state value of the deformation parameter, D, has been compared with Taylor analytic formula [154] (including Shapira and Haber corrections [139]), numerical results by Zhou and Pozrikidis [187] (2D Boundary Integral Method), Li et al. [95] (3D simulations) and Komrakova et al. [81] (3D simulations) and experimental results by Guido and Villone [56]. Results from the presented simulations are reported with empty red squares for 2D simulations and empty red diamonds for 3D simulations. A good agreement can be observed among all these works, see Fig. 4.5. In particular, the presented results are in excellent agreement with other numerical results [81, 95, 187] and with the predictions of Taylor analytic formula [139, 154]. A good agreement is also observed with the experimental results from Guido and Villone [56]; the difference observed can be attributed to the small viscosity contrast among the two fluids (in the experiments a slightly more viscous fluid was used for the droplet), which reduces the droplet final deformation. From Fig. 4.5 it can be observed how 2D and 3D steady-state droplet deformations start to deviate for increasing capillary numbers: the deformation of 3D droplets is slightly larger at the highest capillary number tested. This behavior is in agreement with previous findings of Afkhami et al. [1], who performed an extensive comparison of 2D and 3D droplet deformation, showing that a good agreement between 2D and 3D simulations is found only at low capillary numbers.

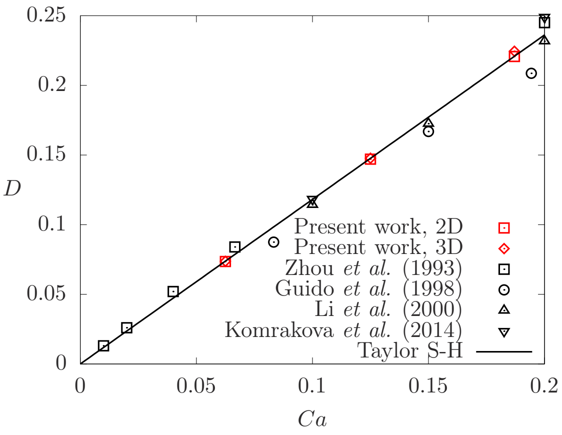

FIGURE 4.5 – Steady-state value of the droplet parameter deformation as a function of the capillary number, Ca. The results obtained from our simulations are reported with empty red squares (2D simulations) and with empty red diamonds (3D simulations). The analytic relation is reported with a black solid-line. The results obtained from previous studies are also reported for comparison: Zhou and Pozrikidis [187] (2D Boundary Integral Method), Guido and Villone [56] (experiments), Li et al. [95] (3D simulation) and Komrakova et al. [81] (3D simulation).

4.3.2 Time evolution of the droplet principal axes

To better understand the origin of the agreement between 2D and 3D droplet deformation at low capillary numbers and of the subsequent divergence at larger capillary numbers, the time evolution of the three principal axes is investigated in this section. This is an important issue, as Taylor analytic formula, which is derived for 3D droplets, is often used as a validation tools of 2D simulations; it is thus important to assess the limit of validity of this formula when comparing it to 2D simulations. In addition, a more detailed study on the deformation of each axis will allow to obtain further insights on the differences observed between 2D and 3D cases and on their agreement at low capillary numbers.

Taylor analytic formula is obtained with the hypothesis that the deformed droplet is a prolate spheroid ($a > b = c$). On the contrary, the numerical simulations performed show that 2D droplets cannot deform in the y direction (c axis), while 3D droplets are not constrained to be a prolate spheroid. This latter observation was also confirmed by the experiments of Guido and Villone [56]. The length of the three principal axes of the droplet is reported in Fig. 4.6 over time. The major axis of deformation, a, is reported with solid lines, the minor axis of deformation, b, with dashed lines and the third axis, c, with dotted lines. The different colors refer to the three capillary numbers tested. At the beginning of the simulation the major axis, a, starts to elongate, while the minor axis, b, starts to shrink. In the initial part of the simulation the c axis does not change. When the major and minor axes of deformation have reached almost their steady-state length, the third axis starts shrinking. Shrinkage/elongation magnitude increases with the capillary number: as surface tension forces becomes weaker with respect to viscous forces, the droplet becomes more deformed. With the prolate spheroid assumption leading to Taylor formula, axes b and c are constrained to

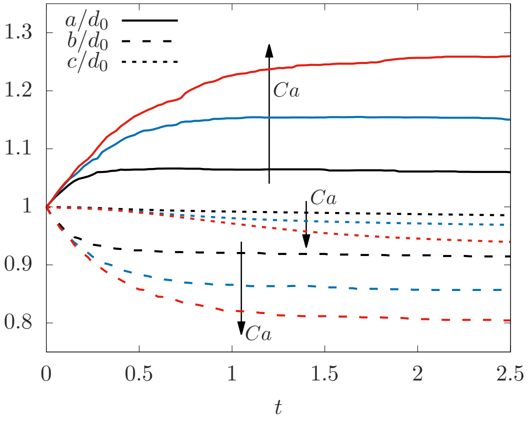

FIGURE 4.6 – Time evolution of the length of the three principal axes of the droplet (3D simulation): major axis of deformation, a (solid line), minor axis of deformation, b (dashed line) and third axis, c (dotted line). The lengths are normalized by the initial droplet diameter, d_0. The results obtained from the different capillary numbers are colored in black ($Ca = 0.062$), blue ($Ca = 0.125$) and red ($Ca = 0.187$). The axis a increases with time, while the axes b and c decrease over time. The shrinkage of the axes c becomes considerable at higher capillary numbers. Time, t, is made dimensionless using the shear rate, u_w/h.

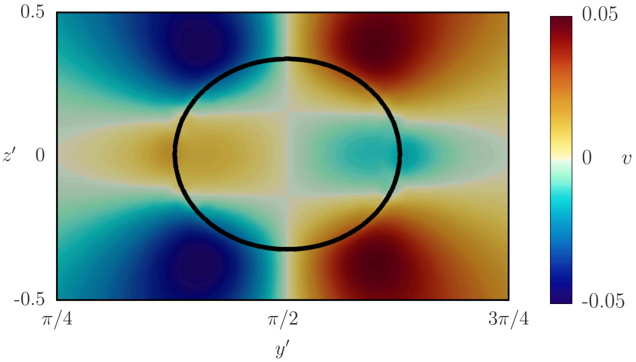

FIGURE 4.7 – Instantaneous spanwise velocity in a y'-z' plane (see also Fig. 4.2 for details on the axes orientation). The map refers to the case $Ca = 0.187$ at time $t = 1.0$. The shrinkage of the c axis induces a flow motion from the sides of the droplet to the core. This flow can be appreciated looking at the central area of the droplet ($-0.2 < z' < 0.2$). In addition, in the carrier phase, four distinct regions with high spanwise velocity can be appreciated. These regions highlight the modifications in the external flow produced by the droplet.

be equal. With this assumption, the integral of surface forces over the droplet interface is higher (on average the curvature is higher) and, thus, a stronger shear rate is needed to achieve the same steady-state deformation of an unconstrained droplet (axes a, b and c can vary independently). Hence, Taylor analytic formula underestimates the droplet deformation; this feature is even clearer at high capillary numbers.

The shrinkage of the third axis is a crucial parameter in determining the deformation of 2D and 3D droplets. For the 2D case no out-of-plane velocity can appear, thus no shrinkage in the third axis direction occurs. Due to this constraint 2D (circular) droplets undergo a lower deformation with respect to their 3D counterpart. Indeed, the shrinkage of c axis enhances the droplet deformation for 3D cases; this finding is confirmed in the experiments of Guido and Villone [56], who were able to measure at the same time all the three principal axes in their experiments. The contribution of the third axis to the overall droplet deformation can be qualitatively visualized in Fig. 4.7: a clear feeding from the sides of the droplet towards the core region (for further details on the auxiliary reference frame and the denomination of the various parts of the droplet, please refer to Fig. 4.2) can be observed. These fluxes are a direct consequence of the shrinkage of the third axis and enhance the deformation of the droplet.

The results, thus, show that the third axis undergoes a limited shrinkage at low capillary numbers, as found in experiments [56]. The low shrinkage of c limits its effect on the deformation of the droplet; indeed a good agreement between 2D (no c shrinkage) and 3D simulations (limited c shrinkage) is found at low capillary numbers. This agreement can also be extended to experiments and Taylor analytic formula in the limit of low capillary numbers. As the capillary number is increased, analytic predictions and 2D simulation results start to deviate from experimental and numerical (3D simulations) results.

4.4 Surfactant-laden droplets

This section is devoted to the analysis of the effects of surfactant on the droplet deformation. In particular, when a surfactant is present at the interface, three additional effects have to be considered: (*i*) surfactant reduces the average surface tension, (*ii*) surfactant accumulates at the tips of the deformed droplet, further reducing the local surface tension, Fig. 4.8(a), and (*iii*) the shear-induced inhomogeneous surfactant distribution generates stresses tangential to the interface, Fig. 4.8(b). Each of these effects contributes in a different way to the overall droplet deformation. In particular, the first and second effects (lower average surface tension and surfactant accumulation at the droplet tips, respectively) favor the droplet deformation. Conversely, the third effect (inhomogeneous distribution of surfactant and, thus, of surface tension) generates tangential (Marangoni) stresses that hinder the droplet deformation.

To investigate each of these effects and quantify their relative contribution to the droplet deformation, two surfactant-laden simulation have been run for each capillary number. The two series of simulations differ for the total amount of surfactant, set via the surfactant bulk concentration; L-series (low surfactant loading) has $\psi_b = 0.01$, while H-series (high surfactant loading) has $\psi_b = 0.02$. Two additional simulations (2D and 3D, same parameters of case L3) have also been run neglecting the contribution

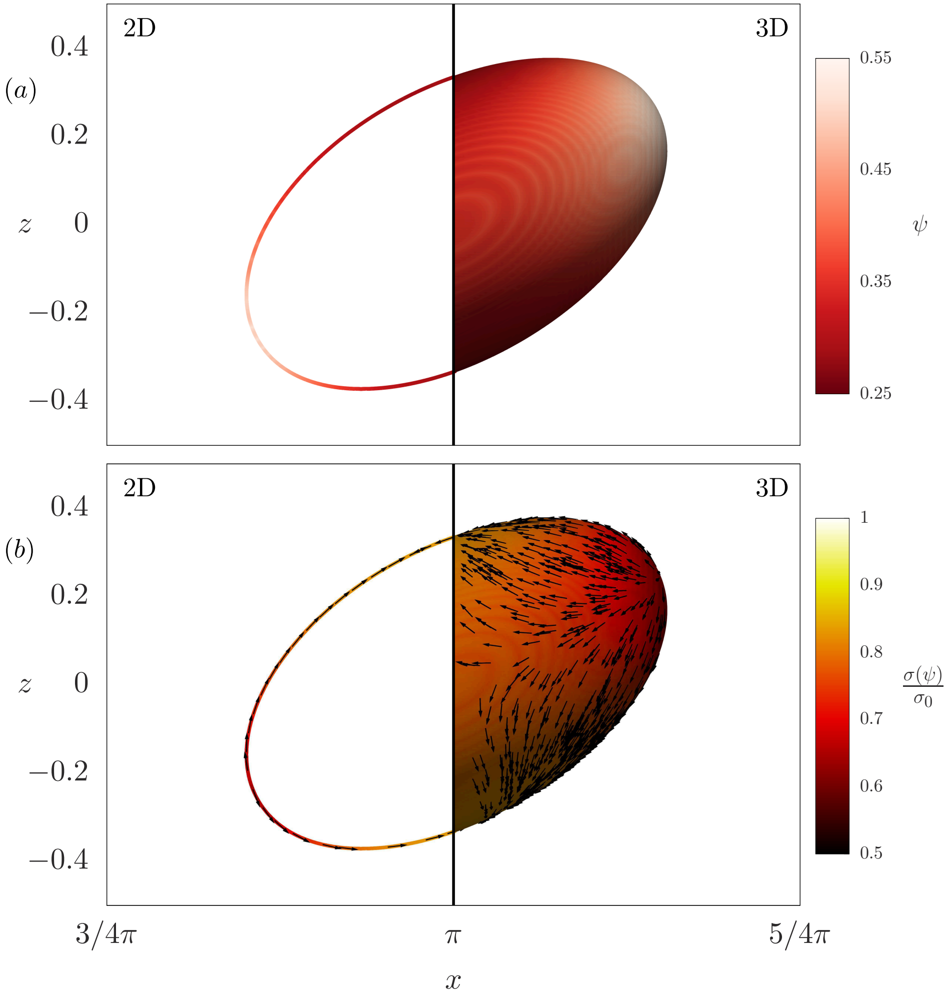

FIGURE 4.8 – Panel (a) shows the surfactant distribution over the droplet interface. Due to the action of the external shear stress, surfactant accumulates at the droplet front and back, while the droplet belly is depleted of surfactant. Panel (b) depicts the dimensionless surface tension, $\sigma(\psi)/\sigma_0$, over the droplet interface. Marangoni stresses, which originate from the surface tension gradients, are reported using black unit-length vectors. In both panels, results obtained from 2D cases are reported on the left, while those obtained from 3D cases are reported on the right. The snapshots are taken at $t = 2.5$ (steady-state deformation) and refers to the case H3 ($\psi_b = 0.02$, $Ca = 0.187$).

of Marangoni stresses; these cases will be used to better highlight the contribution of Marangoni stresses on the overall deformation.

4.4.1 Droplet deformation

The presence of surfactant over the interface increases the steady-state deformation of the droplets, as can be observed in Fig. 4.9(a)-(b). The deformation parameter increases with the amount of surfactant present in the system: at low surfactant loading, Fig. 4.9(a), the deformation of the droplet is slightly higher than that predicted by Taylor formula, while at high surfactant loading, Fig. 4.9(b), the deformation parameter is consistently higher. In addition, while Taylor formula well predicts the deformation parameter at the lower capillary numbers for the low surfactant loading case, it underestimates the deformation parameter obtained at $\psi_b = 0.02$ for all the capillary numbers tested.
With the aim of quantifying the contribution of each one of the three surfactant-induced effects on the droplet deformation, the effective capillary number has been considered. The capillary number, Ca, is defined here using the surface tension of a clean interface (absence of surfactant, σ_0); the effective capillary number, Ca_e, is defined using the actual surface tension over the droplet interface. The average surface tension, $\langle\sigma\rangle$, is calculated over the interface considering the reduction operated by the surfactant.

$$Ca_e = \frac{\eta u_w}{\langle\sigma\rangle}\frac{d}{2h} \tag{4.6}$$

This way, the result of the first surfactant-induced effect is highlighted: Ca_e considers only the effect introduced by a lower average surface tension. The deformation parameter is reported as a function of the effective capillary number in Fig. 4.9(c)-(d) for all the six surfactant-laden cases. When using the effective capillary number, a close agreement with Taylor analytic formula is observed. Still, at high capillary numbers Taylor formula under-predicts the results of the simulation; as already discussed earlier, this is an effect introduced by the prolate spheroid hypothesis used to derive the analytic solution. This result proves that, in the range of parameters investigated here, the most important surfactant-induced effect is the average surface tension reduction, which can be accounted for by using the effective capillary number, Ca_e.

4.4.2 Surfactant distribution

The latter two surfactant-induced effects, accumulation at the droplet tips and inhomogeneous surface tension over the interface, are now investigated. In particular, the surfactant distribution over the droplet interface is quantified using the joint Probability Density Function (PDF) of the surfactant concentration at the interface and of the mean curvature, κ. The mean curvature of the interface is calculated as the semi-sum of the two principal curvatures, κ_1 and κ_2, and can be directly computed from the phase field. For the 2D cases (circular droplet, cylindrical when extended to 3D), only the first principal curvature is defined, thus the second principal curvature is set to $k_2 = 0$. The mean curvature is defined as half of the divergence of the normal to the interface, $\mathbf{n}$, which, in the framework of the phase field method, can be computed

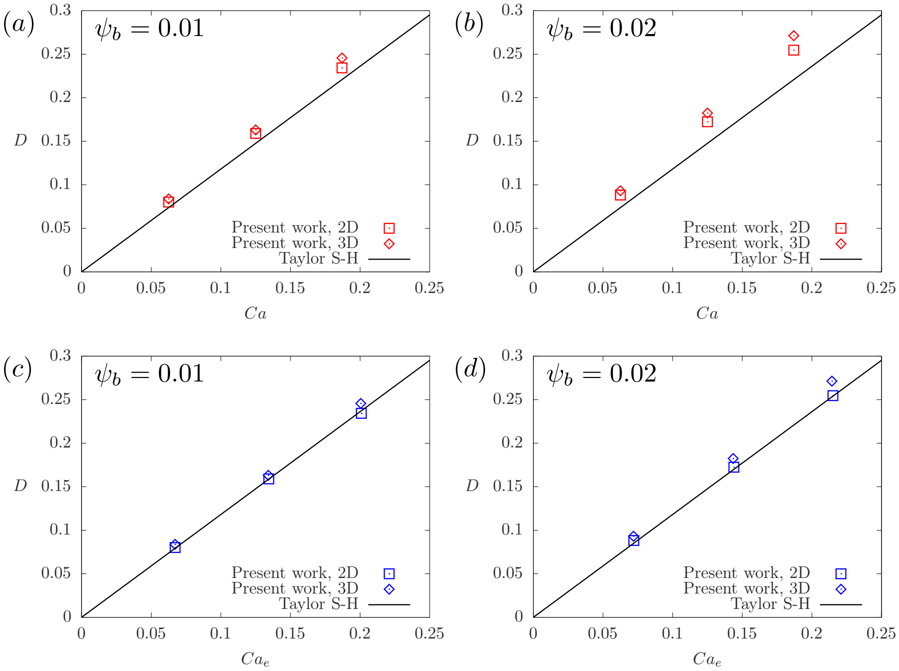

FIGURE 4.9 – Steady-state value of the droplet parameter deformation as a function of the capillary number, Ca, panels (a)-(b) and as a function of the effective capillary number, Ca_e, panels (c)-(d). Panels (a)-(c) refer to the cases L1, L2 and L3, surfactant bulk concentration $\psi_b = 0.01$ while panels (b)-(d) refer to the cases H1, H2 and H3, surfactant bulk concentration $\psi_b = 0.02$. Taylor formula [154] is plotted with a black solid line.

from the phase field as [5, 148]:

$$\mathbf{n} = -\frac{\nabla\phi}{|\nabla\phi|} \,. \tag{4.7}$$

The minus sign is needed to obtain the outward-pointing normal ($\phi = +1$ in the droplets and $\phi = -1$ in the carrier fluid). The mean curvature, thus, is:

$$\kappa = \frac{1}{2}\nabla \cdot \mathbf{n} = -\frac{1}{2}\nabla \cdot \left(\frac{\nabla\phi}{|\nabla\phi|}\right) \,. \tag{4.8}$$

Fig. 4.10 shows the joint PDF for the L-series (low surfactant loading, $\psi_b = 0.01$); results of 2D simulations are reported in the left column, while those of 3D simulations in the right column. Each row corresponds to a different capillary number: $Ca = 0.062$ (top row), $Ca = 0.125$ (middle row) and $Ca = 0.187$ (bottom row). A red vertical dashed line denotes the initial curvature, $k_0 = 2/d_0$ for the 2D cases and $k_0 = 4/d_0$ for the 3D cases, while a red horizontal dashed line identifies the initial (equilibrium) surfactant concentration at the interface, ψ_0. The effect of the capillary number on the droplet mean curvature can be immediately noticed: for increasing Ca the droplet deforms more, thus higher (at the tips) and lower (in the central region) curvature values of the mean curvature can be found. Conversely, the capillary number has a limited effect on the surfactant concentration. Also the problem dimensionality has a clear effect on the range of curvature values sampled: for circular droplets (2D) the second principal curvature is always zero (cylindric surface), so the mean curvature for 2D droplets is about half that of 3D droplets. The joint PDFs for 2D and 3D cases show a common trend: high surfactant concentration well correlates with high-curvature regions. However, even though the trend is similar, 2D and 3D simulations exhibit a different behavior: 2D cases show a bimodal distribution, while 3D cases a trimodal distribution.

The bimodal distribution observed on 2D surfactant-laden droplets originates from the asymmetric distribution of surfactant with respect to the major axis of deformation, a: the shear stresses sweep surfactant toward the back and the front of the droplet (see Fig. 4.2 for the denomination of the regions of the droplet). Thus, regions with the same curvature experience two different surfactant concentrations. As the capillary number is increased, panels (c) and (e), the bimodal distribution becomes even clearer and the two branches of the distribution part away. This particular distribution can be appreciated also in Fig. 4.8(a): surfactant accumulates at the back (and front, not shown) of the droplet, while the belly is depleted of surfactant (dark red). The left side of the joint PDF corresponds indeed to the droplet belly: low surfactant concentration in regions with a low mean curvature.

3D simulations are characterized by a trimodal distribution; the third branch corresponds to the sides of the droplets, where the surfactant concentration is lower, but the mean curvature is relatively high, see Fig. 4.8(a). The third branch become more evident for higher capillary numbers, as the droplet undergoes a stronger deformation, panels (d) and (f), and a wider range of curvature values is sampled.

The results from cases H1 to H3 (higher surfactant bulk concentration, $\psi_b = 0.02$) show an analogous behavior, thus they have not been reported. The joint PDF confirms the tendency of the surfactant to accumulate in high-curvature regions, which are also stagnation points [147]. However, the resulting surfactant distribution is not straightforward and it is affected by the local flow.

4.4.3 Effect of Marangoni stresses

Lastly, the importance of Marangoni stresses on the droplet deformation is investigated. In the previous section the accumulation of surfactant near the tips of the droplet (high curvature region) has been described; this inhomogeneous surfactant distribution (and, consequently, surface tension distribution) generates Marangoni stresses. The effects of the average surface tension reduction and of the higher deformability at the droplet tips (due to surfactant accumulation) have been quantified, showing how they increase the overall droplet deformation. Marangoni stresses, however, hinder droplet deformation: they are tangential to the interface and they follow the surface tension gradient, from low surface tension regions (high surfactant concentration) towards high surface tension regions (low surfactant concentration). Thus, these tangential stresses, reported as black arrows in Fig. 4.8(b), are directed from the tips to the belly of the droplet. Case L3 (2D and 3D) has been recomputed neglecting Marangoni stresses (see Eq. (4.1)) and the resulting steady-state deformation

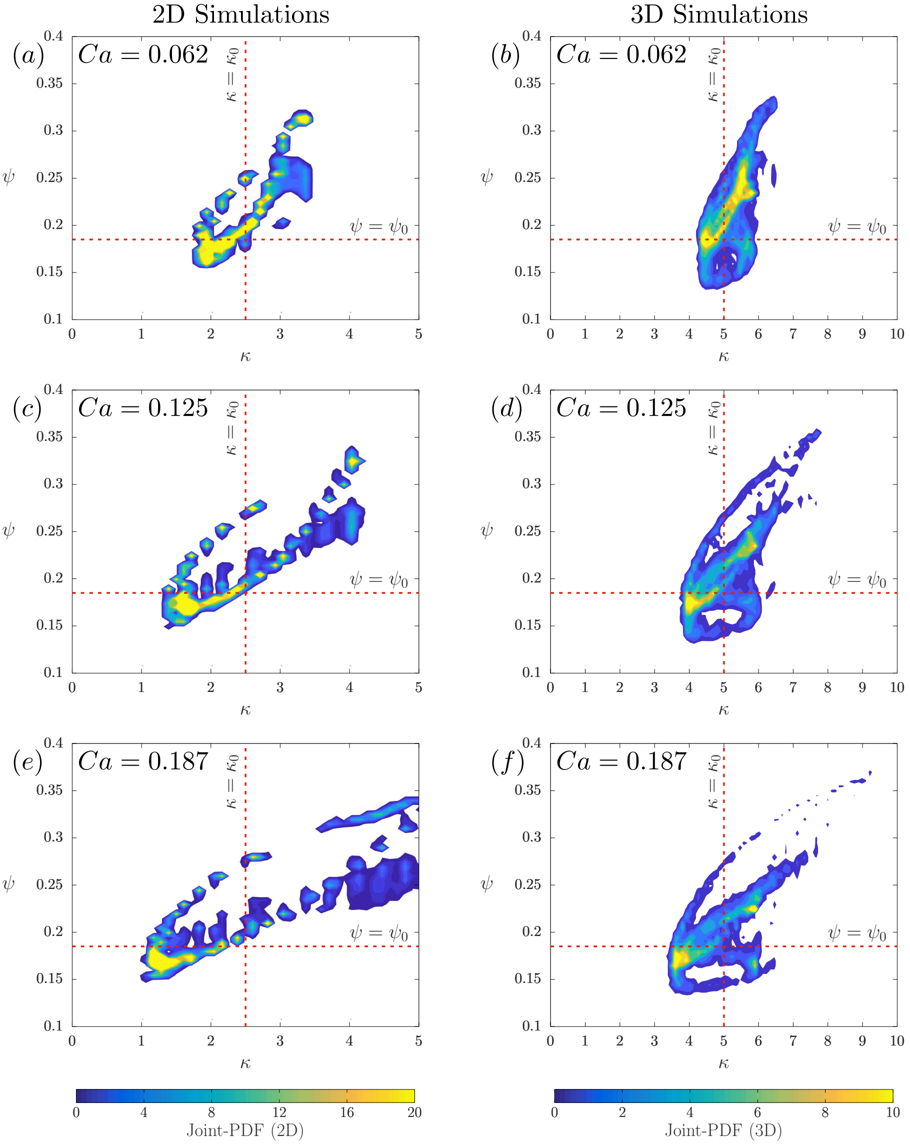

FIGURE 4.10 – Joint Probability Density Function (PDF) of the interface mean curvature, κ, and surfactant concentration, ψ, sampled at the interface of the deformed droplet for the lower surfactant bulk concentration, $\psi_b = 0.01$. The left column, panels (a)-(c)-(e), refers to 2D simulations while the right column, panels (b)-(d)-(f) refers to 3D simulations. Each row corresponds to a different capillary number, $Ca = 0.062$ (panels (a) and (b)), $Ca = 0.125$ (panels (c) and (d)) and $Ca = 0.187$ (panels (e) and (f)). A red vertical dashed line identifies the initial curvature, $\kappa_0 = 2/d_0$ (2D) and $\kappa_0 = 4/d_0$ (3D), while a red horizontal line identifies the initial surfactant concentration at the interface, ψ_0.

Table 4.2 – Droplet deformation parameter, D, for the simulation L3 ($Ca = 0.187$) with and without Marangoni stresses. First column, results obtained from 2D simulations; second column, results obtained from 3D simulations. It can be noticed that the role played by Marangoni stresses on the overall droplet deformation is marginal.

	2D Simulations	3D Simulations
With Marangoni term	0.235	0.244
Without Marangoni term	0.237	0.246

parameter has ben calculated and reported in Tab. 4.2. The results indicate that the contribution of Marangoni stresses is almost negligible, with a difference in the deformation parameter lower than 1% for both 2D and 3D droplets.

4.5 Conclusions

In this chapter the effect of the problem dimensionality (2D *vs* 3D) on the deformation of a droplet in laminar shear flow has been investigated for both clean and surfactant-laden droplets. First, the range of validity of Taylor formula for the steady-state deformation of a droplet has been tested and its predictions have been compared to numerical results from 2D (circular droplets) and 3D (spherical droplets) simulations. It was found that at low capillary numbers the droplet deformation predicted by Taylor formula well agrees with the numerical results. In particular, in the limit of small deformations, the deformation of circular and spherical droplets matches, thus lightweight 2D simulations can be used as a benchmark instead of more computationally-expensive 3D simulations. However, at the larger capillary number tested here, $Ca = 0.187$, the different problem dimensionality becomes important: the shrinkage of the third axis of the droplet plays an important role in the droplet deformation, leading to different results between 2D and 3D cases. Also Taylor analytic formula starts to under-predict experimental and numerical results at a similar capillary number: this formula was obtained with the hypothesis that the deformed droplet is a prolate spheroid, with the two minor axes of the same length. This hypothesis is not verified by numerical and experimental data.

In the second part of the chapter, the effect of a soluble surfactant has been investigated. For the range of parameters tested here, the main contributions of the surfactant to the droplet deformation are linked to the average surface tension reduction and to the accumulation of surfactant at the tips of the droplet: Taylor formula well predicts the deformation of a surfactant-laden droplet when the effective capillary number, Ca_e, is used (in the limit of small deformations). Conversely, Marangoni stresses hinder the droplet deformation; their effect however, for the range of parameters tested, is almost negligible. These results prove that Taylor formula can be used to predict the steady-state deformation of surfactant-laden droplets in the limit of small deformations; clearly, increasing the strength of the surfactant (e.g. increasing its elasticity number) or the total amount of surfactant (e.g. the surfactant bulk concentration) enhances the surface tension reduction, thus reducing the range of validity of Taylor formula for surfactant-laden droplets.

5

Surfactant effects on binary droplet interactions

Reproduced in part from:
G. Soligo, A. Roccon, and A. Soldati, *Coalescence of surfactant-laden drops by Phase Field Method*, Journal of Computational Physics 376:1292–1311, 2019.

The main effect of a dissolved surfactant is reducing surface tension with respect to a clean (without surfactant) interface. Without any external forcing or perturbation, the surfactant will homogeneously cover the entire interface available; in this case a uniform surface tension reduction will be observed. However, in most cases of interest the flow field strongly interacts with the interface, deforming it and advecting surfactant over it. When the surfactant concentration is perturbed from its uniform distribution over the interface, mainly two factors act to restore the homogenous distribution, namely Marangoni stresses and surfactant diffusion. The latter factor, diffusion, is generated by the entropy term in the surfactant chemical potential, Eq. (2.15), while the former one, Marangoni stresses, originates from the local surface tension reduction operated by the surfactant. This surface tension reduction is determined by the surfactant strength (the elasticity number, β_s) and by the local surfactant concentration. This effect is modelled here using the modified Langmuir equation of state, Eq. (2.26), which also accounts for the surfactant saturation observed in experiments [21, 71, 100, 149]. With the selected equation of state, the surface tension reduction depends on two parameters, a global one (elasticity number) and a local one (surfactant concentration). Thus, a non-homogeneous surfactant concentration generates a variable surface tension and, in turn, surface tension gradients over the interface. Such surface tension gradients produce stresses tangential to the interface, which are called Marangoni stresses. This stresses are directed as the surface tension gradient (thus opposite to the surfactant concentration gradient), from regions characterized by a lower surface tension (high surfactant concentration) to regions characterized by a higher surface tension (low surfactant concentration). As Marangoni stresses originate only from surface tension gradients, local modifications of the surface tension are needed for these stresses to manifest; thus, the need for a local change in surface

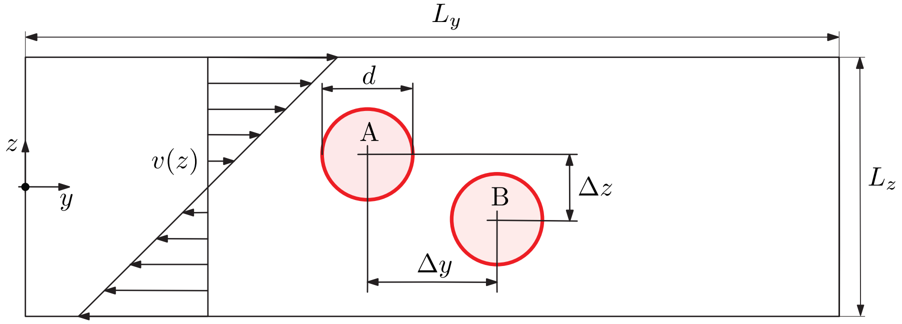

FIGURE 5.1 – Simulation setup used to analyze the effects of a dissolved surfactant on binary droplets interactions. Two circular droplets, $d = 0.7$, are placed at $y_c = \pi \mp 0.5$ and $z_c = \pm 0.25$ (coordinates of the droplets center of mass at the beginning of the simulation). The offset in the streamwise direction is $\Delta y = 1$, while in the wall-normal direction is $\Delta z = 0.5$. The two walls move in opposite directions, generating a laminar shear flow in the channel, $v(z)$.

tension, for instance through the addition of surfactant, as in this work, or with a temperature-dependent surface tension.

In the following, the collision of two droplets will be simulated to illustrate the importance of surfactant (and Marangoni stresses) in preventing, or at least delaying, coalescence. The surfactant dynamics (average surface tension reduction and Marangoni stresses) will be presented and their effect on the droplets interaction will be explained.

5.1 Simulation setup

The setup adopted for this test case is reported in Fig. 5.1: two droplets, $d = 0.7$, are brought into collision in a two-dimensional closed channel bounded by two walls at $z = \pm 1$. The two solid walls move in opposite directions: the top wall moves with velocity $v_w = +1$, while the bottom wall moves with velocity $v_w = -1$. At the beginning of the simulation a linear velocity profile, $v(z)$, is initialized in the channel; the Reynolds number, calculated using the wall velocity as the reference velocity scale, is $Re = 0.5$. Due to the different local velocity experienced, the two droplets will start approaching: droplet A will move towards positive y direction, while droplet B will move towards negative y direction.

The channel, with dimensions $L_y \times L_z = 2\pi \times 2$, is discretized with $N_y \times N_z = 512 \times 513$ grid points. To properly resolve the interfacial layer a Cahn number $Ch = 0.02$ was selected for the present configuration. The phase field Péclet number was set according to the scaling $Pe_\phi = 3/Ch = 150$ [108, 183]. The capillary number was set to $Ca = 0.1$. The capillary is calculated according to Eq. (2.128). The Péclet number for the surfactant was set to $Pe_\psi = 100$; the other surfactant parameters were set to $Pi = 1.35$ and $E_x = 0.117$ [47]. The elasticity number, β_s, and the surfactant bulk concentration, ψ_b, are the two free parameters used to control and investigate the surfactant-induced effects; the former determines the strength of the surfactant (efficacy in reducing surface tension), while the latter quantifies the total amount of surfactant available at the interface.

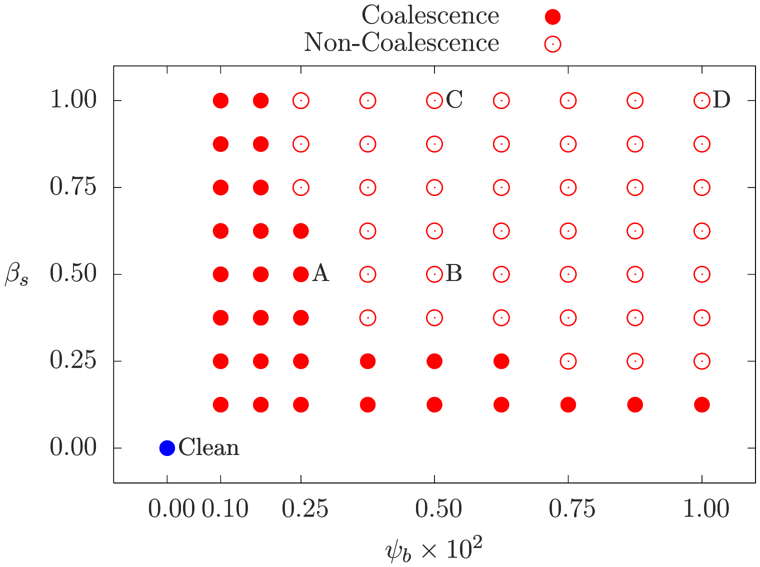

FIGURE 5.2 – Map of the droplet-droplet interaction outcome. A filled dot identifies a coalescence event, while an empty dot identifies a non-coalescence event. The clean case has also been reported for reference (blue filled marker); this case corresponds to complete absence of surfactant ($\psi_b = 0$) or to zero-strength surfactant ($\beta_s = 0$). The cases that will be used in the following have been labelled for reference: Clean, A, B, C, D.

At the beginning of the simulation two circular droplets with diameter $d = 0.7$ are initialized at $y_c = \pi \mp 0.5$, $z_c = \pm 0.25$ (mass center coordinates). Thus the offset between the droplets is $\Delta y = 1$, $\Delta z = 0.5$. The phase field and surfactant concentration are initialized with their respective equilibrium profiles, Eq. (2.11) for the phase field and Eq. (2.23) for the surfactant concentration. The droplets are characterized by $\phi = +1$, while the carrier flow by $\phi = -1$. The initial flow field is a laminar shear flow for the streamwise component, $v(z) = z$. The wall-normal velocity component is initialized to zero.

5.2 Outcome of binary droplets interactions

The outcome of the droplet-droplet interactions has been reported as a function of the surfactant strength, characterized with the elasticity number, and of the surfactant bulk concentration. The outcomes from all the simulations, reported in Fig. 5.2, allow to map coalescence (filled markers) and non-coalescence (empty markers) regions as a function of the surfactant parameters. It is clear that either a stronger surfactant (higher β_s), either a larger surfactant concentration (higher ψ_b) decreases the likelihood of a coalescence event. As can be seen from the outcome map, only the weakest surfactant, $\beta_s = 0.125$, is not able to prevent coalescence for any of the surfactant bulk concentrations tested here. Increasing the surfactant strength, $\beta_s = 0.25$, coalescence can be prevented for high surfactant bulk concentrations, $\psi_b > 7.5 \times 10^{-3}$. Further increasing the surfactant strength reduces the minimum surfactant bulk concentration needed to prevent coalescence: for $0.375 \leq \beta_s \leq 0.675$ coalescence is prevented for any surfactant bulk concentration above $\psi_b = 2.5 \times 10^{-3}$ and for $0.75 \leq \beta_s \leq 1.00$ this value decreases to $\psi_b = 1.25 \times 10^{-3}$.

The map of the interaction outcomes, Fig. 5.2, shows that an increase in either the total amount of surfactant (determined by the surfactant bulk concentration), either the surfactant strength (set through the elasticity number) favors a non-coalescence event. This result implies that the deformability of the interface is a key factor in determining the outcome of the interaction: a more deformable interface (lower average surface tension, determined by stronger surfactant effects) favors non-coalescence events. In the following section a detailed description of the droplets interaction will be given, particularly focusing on the mechanisms that prevent coalescence.

5.3 Interaction dynamics

The time evolution of two cases is reported in Fig. 5.3 and Fig. 5.4. Cases A and C have been chosen to display two different outcomes: a coalescence (case A) and a non-coalescence (case C). Case A is characterized by a lower amount of surfactant (lower ψ_b) and by a weaker surfactant (lower β_s). The strain rate $S_x = (\partial v/\partial z + \partial w/\partial y)/2$ is reported in Fig. 5.3, while the local surfactant concentration over the interface is reported in Fig. 5.4. The surfactant concentration is reported only at the interface ($\phi = 0$) to better highlight its dynamics; surfactant concentration in the bulk of the phases is not reported as it is constant and equal to the surfactant bulk concentration. Three different stages of the interaction process are reported: approaching, gap draining and final stage. At time $t = 1.0$ (approaching stage) the droplets are carried by the imposed shear flow and move towards the channel centre, Fig. 5.3(a)-(b). During this initial stage droplets are deformed by the shear flow and start to flatten due to the presence of the other droplet; surfactant accumulates at the droplets tips, Fig. 5.4(a)-(b). Later on, the draining stage starts: the liquid film that separates the droplets is squeezed by the approaching interfaces and starts draining. This stage determines the final outcome of the interaction: if the liquid film drains completely the attractive short-range van der Waals forces make the interface merge [24, 30, 33, 57, 93, 176, 180] and, thus, the droplets coalesce. Conversely, if the liquid film does not drain completely, the droplets slide one over the other, avoiding coalescence. The draining of the liquid film can be appreciated from Fig. 5.3(c)-(d): high strain rate regions highlight the carrier liquid being squeezed out from the gap between the approaching interfaces. The draining of the gap also transports surfactant along the interface: the surfactant is shifted out of the gap region, Fig. 5.4(c)-(d)-(e)-(f). Up to $t = 2.0$ there is no appreciable difference between the cases; at about $t = 3.0$ a clear difference between the strain rate distributions of the two cases can be observed. Starting from $t \simeq 3.0$ the two cases strongly differentiate: droplets will coalesce in case A, while they will slide over each other without merging for case C. The latter stages of the gap draining phase are reported in Fig. 5.3(e)-(f). The negative peak in the strain rate, dark blue region in Fig. 5.3(e), anticipates the coalescence outcome: the lower pressure in this area draws the interfaces closer until they merge. This effect is not seen for case C, where the gap is still draining (but at a lower rate with respect to case A, lower magnitude of the strain rate), Fig. 5.3(f). The same coalescence mechanism

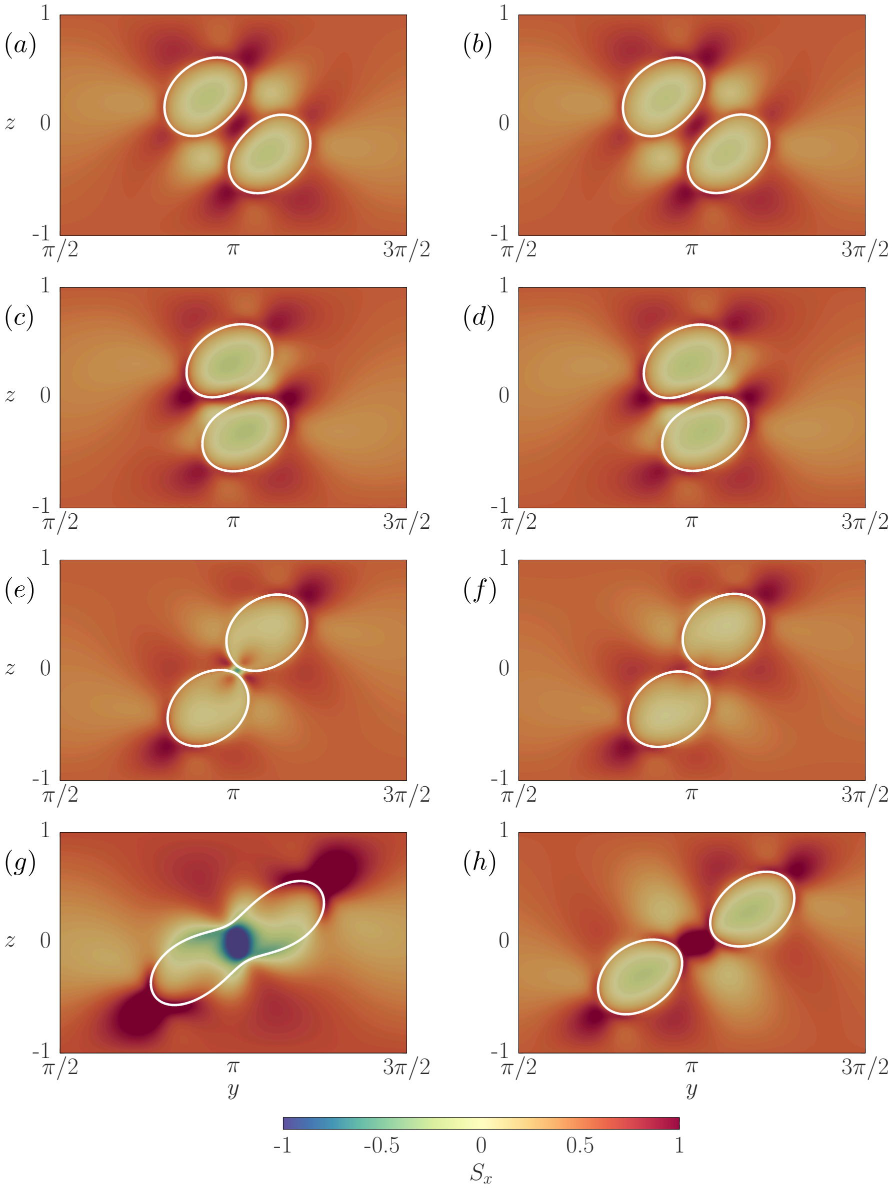

FIGURE 5.3 – Time evolution of the droplets interaction. Time increases from top to bottom: $t = 1.0$ (first row), $t = 2.0$ (second row), $t = 3.0$ (third row) and $t = 4.0$ (fourth row). The left column, panels (a)-(c)-(e)-(g), refers to the case labelled as A ($\beta_s = 0.5$ and $\psi_b = 2.5 \times 10^{-3}$), while the right column, panels (b)-(d)-(f)-(h), refers to case C ($\beta_s = 1.0$ and $\psi_b = 5.0 \times 10^{-3}$). Two different outcomes are observed: a coalescence for case A and a non-coalescence for case C. The interface, $\phi = 0$, is marked with a white solid line; the colormap shows the local value of the strain rate $S_x = (\partial v/\partial z + \partial w/\partial y)/2$.

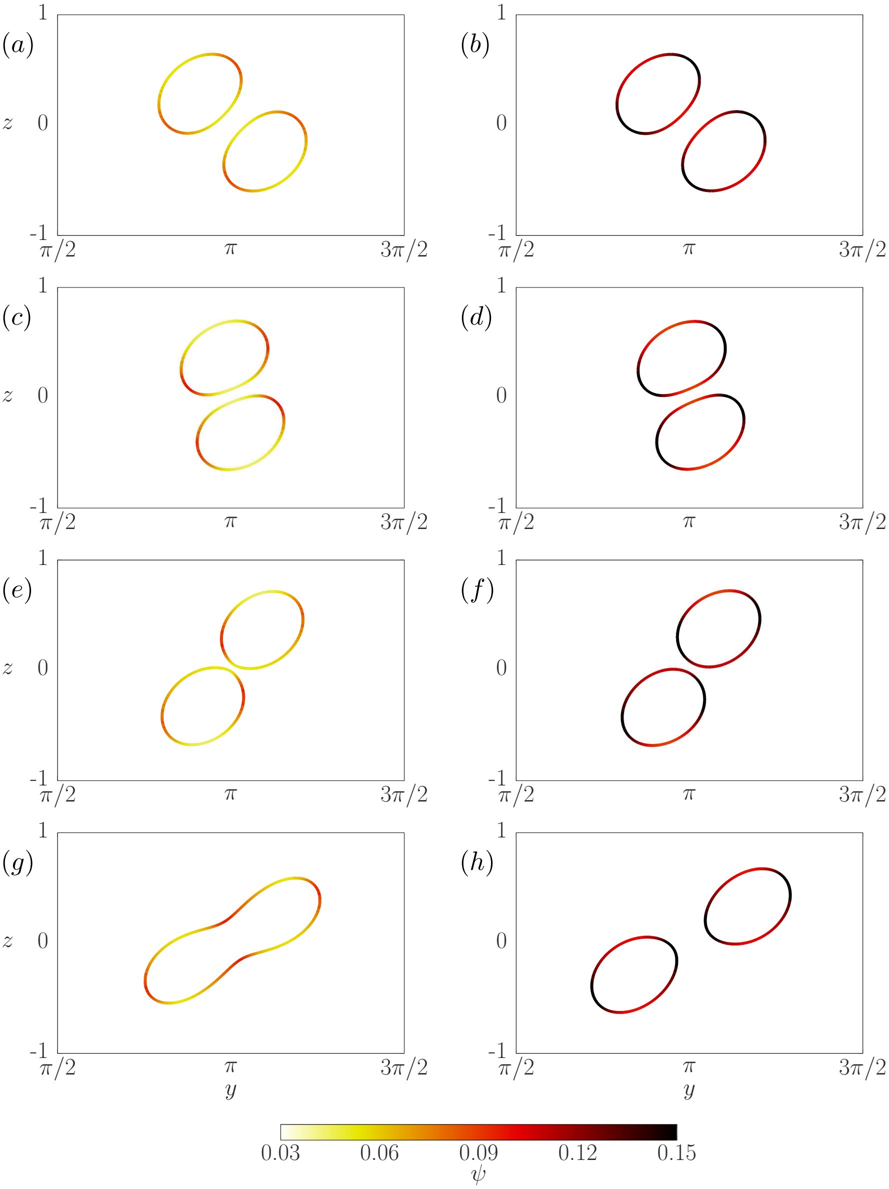

FIGURE 5.4 – Time evolution of the surfactant concentration over the droplets interface, $\phi = 0$, during the interaction. Time increases from top to bottom: $t = 1.0$ (first row), $t = 2.0$ (second row), $t = 3.0$ (third row) and $t = 4.0$ (fourth row). The left column, panels (*a*)-(*c*)-(*e*)-(*g*), refers to the case labelled as A ($\beta_s = 0.5$ and $\psi_b = 2.5 \times 10^{-3}$), while the right column, panels (*b*)-(*d*)-(*f*)-(*h*), refers to case C ($\beta_s = 1.0$ and $\psi_b = 5.0 \times 10^{-3}$). Case A is characterized by a lower amount of surfactant (lower ψ_b) and by a weaker surfactant (lower β_s) with respect to case C. Surfactant accumulates at the droplets tips for both cases; after the coalescence (case A), surface tension forces reshape the droplet and surfactant redistributes over the interface

is observed in experimental works [55]: droplets coalesce once they slide over each other and start to part away. Indeed, the lower pressure region that forms in the gap draws the interfaces together, leading to a coalescence event. Cases A and C differ for the relative strength of surfactant effects: in case A a weaker surfactant is employed and the total amount of surfactant is lower. Thus, on average surface tension will be lower and surface tension gradients will be higher for case C. These two effects prevent the two droplets from coalescing. The increased interface deformability helps in maintaining a thicker liquid film between the interfaces, so that the droplets can slide one over the other, while the higher surface tension gradients result in stronger Marangoni stresses. The draining of the liquid film generates a surface tension gradient along the interface: the gap region is depleted of surfactant (high surface tension), which accumulates outside the gap. This distribution generates a surface tension gradient directed inward the gap and, in turn, Marangoni stresses. These tangential stresses oppose the draining of the liquid film, thus allowing for a longer droplet-droplet interaction. Indeed, surfactant can drastically affect the interaction outcome by changing the draining rate of the liquid film through an increased interfacial deformability and Marangoni stresses [30]. In the following these two effects will be investigated and quantified separately in two distinct sections.

Lastly, the final stage shows the outcome of the interaction: for case C the droplets part away and are transported by the flow, Fig. 5.3(h) and Fig. 5.4(h). For case A, after the droplets coalesced, the newly formed droplet reshapes, Fig. 5.3(g), and the surfactant redistributes over the interface, Fig. 5.4(g). After an initial transient, this droplet will reach a steady state deformation with peaks of surfactant concentration at the droplet tips (not shown here).

5.3.1 Effect of interface deformability

In this section the effect of interface deformability on the outcome of binary droplets interaction is investigated. The deformation parameter, D, has been computed over time for the droplets; since the two droplets deform in the same way, only the deformation parameter of one of them is reported. The deformation parameter is defined as:

$$D = \frac{L - B}{L + B} \ , \tag{5.1}$$

where L and B are respectively the major and minor axes of the droplet, see Fig. 2.10 for reference. The deformation parameter quantifies the macroscopic effect of surfactant: a lower surface tension increases the deformability of the interface, thus increasing the drop deformation. The increased droplet deformability plays a key role in determining whether the droplets will coalesce. The time evolution of the deformation parameter for four surfactant-laden cases (A, B, C and D) and for the clean case (Clean) is reported in Fig. 5.5(a); the five small panels on the top report a qualitative snapshot of the instantaneous system configuration at the marked time for a non-coalescing case. In cases Clean and A, the droplets coalesce after the interaction; once the droplets coalesced (filled dot) the deformation parameter is not anymore computed.

In the initial stage, $t < 1.5$, all the cases evolve in a similar way: the initially circular droplets, $D = 0$, start to deform and their deformation parameter increases. The value

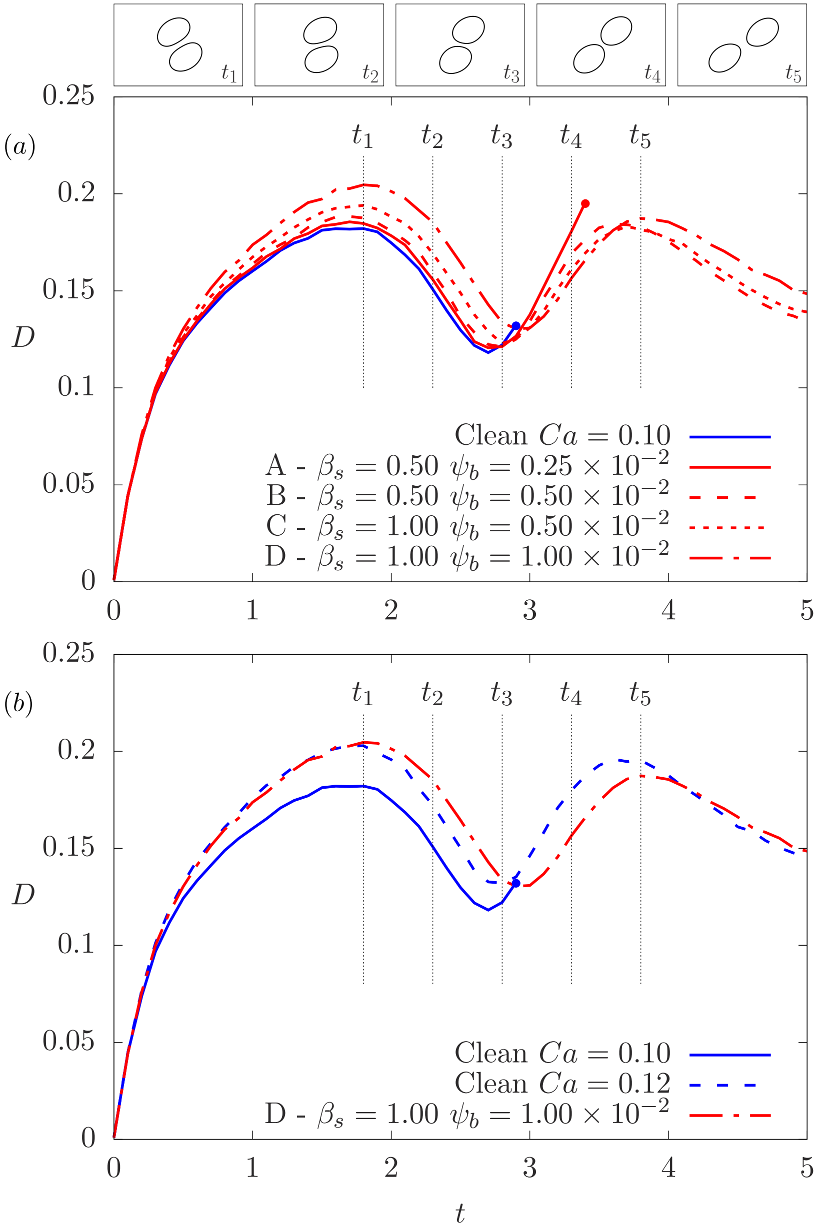

FIGURE 5.5 – Droplet deformation parameter, D, during the interaction; as the droplets evolve in the same way, the deformation parameter of only one droplet is reported. A filled dot identifies a coalescence event; after the coalescence the deformation parameter is not anymore computed. In panel (a) results for different surfactant bulk concentrations and elasticity numbers at capillary $Ca = 0.1$ are compared, while in panel (b) case D (highest surfactant bulk concentration and strongest surfactant) is compared against a clean case with a higher capillary number, $Ca = 0.12$ (same effective capillary, Ca_e of the surfactant-laden case D). The top panels show a qualitative snapshot of the system configuration for a non-coalescing couple at the marked time instant.

of the deformation parameter is different among the various cases: a lower surface tension (originated by stronger surfactant effects) leads to a higher deformation. At $t = t_1$ the droplets are close enough and start to interact; at this time the deformation parameter reaches its maximum value. From the snapshot on top, the liquid film dividing the droplets can be already identified. After $t = t_1$ the droplet deformation reduces until a minimum value is reached at $t = t_3$; this reduction in the deformation is due to the presence of the other droplet, which limits the deformation. Again, the value of the deformation parameter is determined by the average surface tension over the droplet interface: the Clean case (highest surface tension) is characterized by the smallest value, while case D by the highest value. Indeed, increasing the elasticity number or the surfactant bulk concentration reduces the average surface tension. The interaction stage, $t_1 \leq t \leq t_3$, is crucial in determining the outcome of the interaction: a higher deformation reduces the draining rate of the liquid film between the droplets, thus prolonging the duration of the interaction before the eventual coalescence. For cases B, C and D the time required for the complete draining of the liquid film is longer than the interaction time, thus coalescence is avoided. For the Clean and A cases, the draining time is lower than the interaction time and the droplets coalesce, filled circle in Fig. 5.5(a). After $t = t_3$ the droplets separate and the deformation parameter increases until a new maximum value is reached at $t \simeq t_5$; then, the deformation decreases and reaches a steady-state value for $t > 5$ (not shown here).

The results presented suggest that the deformability of the interface is a key factor in determining the outcome of the interaction. To further prove this observation an additional simulation of a clean system is performed. In this latter cases a higher capillary number is used: the capillary number chosen gives the same steady-state droplet deformation of case D. Indeed, given the steady-state deformation for case D, an equivalent capillary number for the clean case is calculated inverting Taylor formula, Eq. (2.131). This equivalent capillary number, which accounts for a lower averaged surface tension, is equal to $Ca = 0.12$ for a clean droplet which reaches the same steady-state deformation of a surfactant-laden droplet with $\psi_b = 1.0 \times 10^{-2}$ and $\beta_s = 1.0$. The time deformation of this latter case is reported in Fig. 5.5(b), together with that of cases D and Clean at $Ca = 0.1$. It can be immediately noticed that the higher capillary number (higher droplet deformability) prevents the two droplets from coalescing: a similar behavior is observed for cases D and Clean at $Ca = 0.12$. A small delay between the two deformations over time appears; this delay may be traced back to the action of tangential stresses along the interface.

The time evolution of the deformation parameter is also in good agreement with previous experimental [55] and numerical [9, 141, 176] studies. Limited differences can be observed during the initial approaching stage, as here a lower offset in the streamwise direction was adopted, thus droplets start to interact earlier. This difference does not affect the interaction and separation phases, which are similar to previous works. This agreement with experiments and numerical studies proves the capabilities of the proposed method in accurately reproducing the dynamics of droplet interaction.

In this section it was proven that the interface deformability alone can prevent droplets coalescence; the increased deformability of the interface increases the time required for a complete draining of the liquid film between the droplets. In the next section it will be shown that the effect of surfactant is more complex than just an average surface

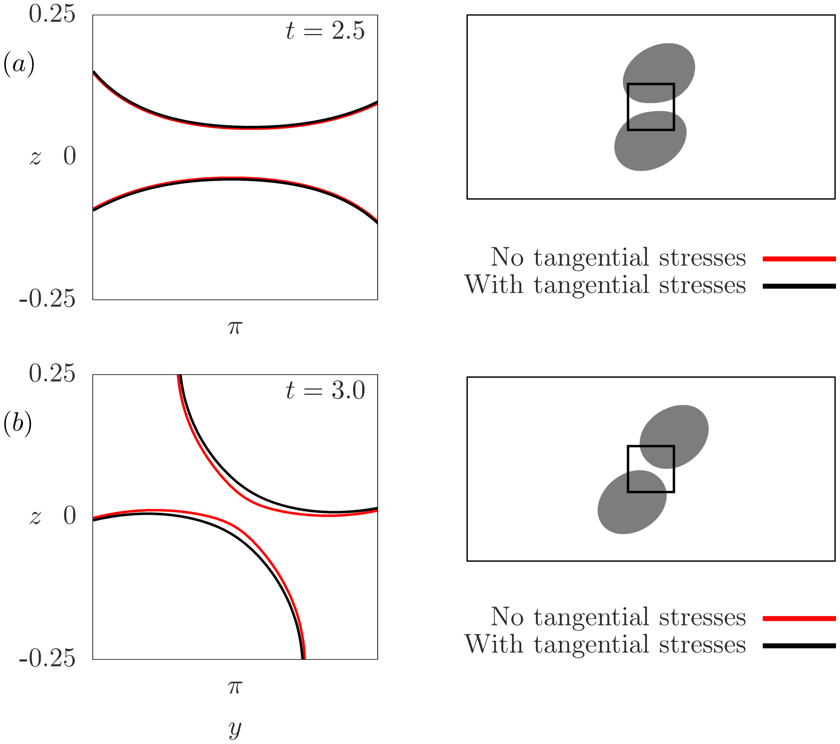

FIGURE 5.6 – Detail of the interface position for case B at $t = 2.5$, panel (a), and at $t = 3.0$, panel (b). Case B has been recomputed neglecting Marangoni stresses. The interface position for these two cases is reported in black for the complete model and in red for the case without tangential stresses. When tangential (Marangoni) stresses are neglected the draining of the liquid film is faster and the two droplets are closer (coalescence is favored).

tension reduction, which can indeed be achieved with a higher capillary number.

5.3.2 Effect of tangential stresses at the interface

The surface force term can be split in two contributions as shown in Eq. (5.2): a contribution normal to the interface, capillary stresses, and a contribution tangential to the interface, Marangoni stresses. A detailed explanation of the various quantities is reported in Sect. 2.2 and Sect. 2.3.

$$\frac{3}{\sqrt{8}}\frac{Ch}{We}\nabla\cdot[\overline{\tau}_c f_\sigma(\psi)] = \frac{3}{\sqrt{8}}\frac{Ch}{We}\left[\underbrace{f_\sigma(\psi)\nabla\cdot\overline{\tau}_c}_{\text{Capillary stresses}} + \underbrace{\nabla f_\sigma(\psi)\cdot\overline{\tau}_c}_{\text{Marangoni stresses}}\right] \tag{5.2}$$

The contribution normal to the interface is common between surfactant-laden and clean cases (for the latter case f_σ is equal to 1); conversely, tangential stresses are peculiar of surfactant-laden cases. In this section the importance of these tangential stresses (also called Marangoni stresses) is quantified: case B ($\psi_b = 5.0 \times 10^{-3}$,

$\beta_s = 0.50$) has been recomputed neglecting Marangoni stresses. This case was selected as small variations in the surfactant properties change the outcome of the interaction: a reduction in the elasticity number or in the total amount of surfactant shifts the outcome of the interaction from the non-coalescence to the coalescence region. When neglecting tangential stresses only part of the surfactant effect is deactivated: surface tension still depends on the local surfactant concentration but surface tension gradients, even though are present, do not generate Marangoni stresses. Thus, this case is different from a clean system with a lower, uniform surface tension.

The interaction outcome for case B is a non-coalescence; however, when neglecting Marangoni stresses the droplets coalesce. This preliminary result suggests that Marangoni stresses are an additional factor playing an important role in coalescence prevention, together with the interface deformability. A detail of the interface position in the interaction area (marked by the black box in the qualitative view on the right) is reported in Fig. 5.6 at two different times. A black line is used for case B (complete model), while a red line for case B recomputed without Marangoni stresses. It can be noticed that the interfaces are closer when tangential stresses are neglected; this effect is already visible at $t = 2.5$ and becomes clear later, at $t = 3.0$. This difference in the interfacial position is an explicit indication of the higher draining rate occurring when tangential stresses are neglected. To quantify the different draining rate between the two cases, the strain rate S_x in the liquid film has been reported in Fig. 5.7. The draining of the liquid film between the two approaching interfaces shifts surfactant outside the gap region; the surfactant concentration along the interface is reported with a grayscale colormap. A gradient of surfactant, generated by the draining of the liquid film, can be observed: the interaction area (point B) is depleted of surfactant, while outside of the gap surfactant concentration is higher (point A). This distribution of surfactant generates a surface tension gradient, which is directed along the interface from point A (high surfactant concentration – low surface tension) to point B (low surfactant concentration – high surface tension). Marangoni stresses, which are directed as the surface tension gradient, thus oppose the draining of the liquid film. This effect is highlighted by the stress distribution in Fig. 5.7: when tangential stresses are considered, panel (a), stresses are lower, with a value closer to the mean strain rate generated by the shear flow, $S_x = 0.5$. Conversely, when tangential stresses are neglected, panel (b), the magnitude of the strain rate is higher (dark blue regions corresponding to $S_x \leq -1$ and dark red regions corresponding to $S_x \geq +1$). The stronger strain rate indicates a higher draining rate, which is not opposed by tangential stresses; due to the higher draining rate the time for the complete depletion of the liquid film reduces, increasing the likelihood of a coalescence event.

The results presented so far indicate that the time required for the complete draining of the liquid film is crucial in determining the outcome of the interaction. In particular, two main mechanisms affecting the draining time have been identified: (i) the interfacial deformability and (ii) the presence of tangential stresses along the interface. The first mechanism derives from a lower average surface tension (higher effective capillary or Weber number) and it is present in both clean and surfactant-laden systems: more deformable interfaces reduce the draining rate of the liquid film. The latter one, however, is peculiar of surfactant-laden systems: the presence of a surfactant gradient and, in turn, of Marangoni stresses directly hinders the outflow from the gap region,

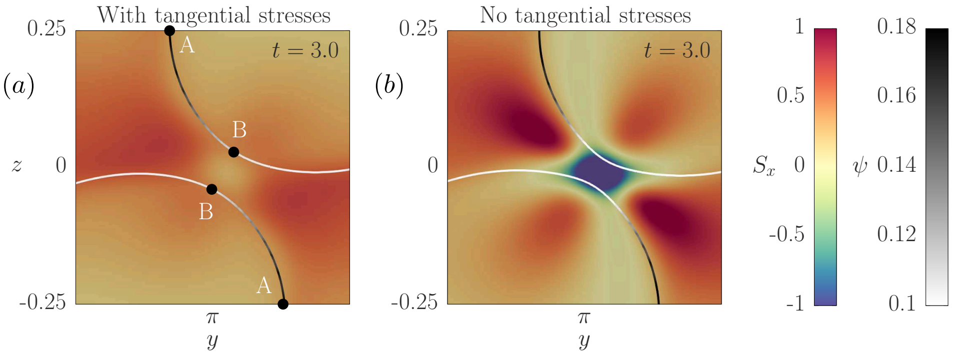

FIGURE 5.7 – Strain rate S_x distribution for case B, with Marangoni stresses, panel (*a*), and without Marangoni stresses, panel (*b*). The surfactant concentration at the interface (contour line $\phi = 0$) is also reported. Tangential stresses hamper the draining of the liquid film and suppress the formation of high strain rate magnitude regions. When these stresses are neglected, the draining process is faster: regions of high strain rate magnitude are observed (panel (*b*), dark red and dark blue areas).

thus reducing the draining rate. These observations are in agreement with previous experimental [30, 55, 93, 117, 169] and numerical [176] results for head-on and offset droplets collisions.

5.4 Conclusions

In this chapter the effect of a dissolved surfactant on the outcome of binary droplets interactions has been investigated and the main mechanisms preventing droplets coalescence have been identified. In particular, it was proven that the interface deformability strongly affects the draining rate of the liquid film: a rigid interface enhances the draining rate, while a more deformable interface is characterized by a higher draining time. This effect can be observed in both clean and surfactant-laden droplets: a uniform, lower surface tension increases the interface deformability and helps in preventing coalescence.

Conversely, the second mechanism, Marangoni stresses, is peculiar of surfactant-laden systems, as it originates from a non-uniform surface tension over the interface. The draining of the liquid film between the two interfaces generates a surfactant concentration gradient, with the gap region depleted of surfactant; the consequent surface tension gradient generates Marangoni stresses. These tangential stresses are directed inside the gap, thus hampering the draining of the liquid film and consequently increasing the draining time.

Finally, the presented results qualitatively agree with previous numerical and experimental works, thus proving the capabilities of the numerical method in accurately predicting and describing the interaction of binary droplets.

6

Breakage, coalescence and droplet size distribution

Reproduced in part from:
G. Soligo, A. Roccon, and A. Soldati, *Breakage, coalescence and size distribution of surfactant-laden droplets in turbulent flow*, Journal of Fluid Mechanics, 881:244–282, 2019.

In this chapter the dynamics of a large swarm of surfactant-laden droplets in turbulence will be investigated. This problem is of high interest, as the accurate prediction of momentum, heat and mass transfers through an interface is crucial in a wide range of industrial and environmental applications and in nature [84, 119, 129]. Mathematical models and empirical correlations, based on macroscopic observables, are often used to estimate these transfer rates [36, 75, 80] and are usually tuned on experimental data to improve the accuracy of their predictions. The development of numerical tools capable of performing high-fidelity numerical simulations is thus highly desirable in order to improve the accuracy of these models and correlations and to better understand the physics underlying the dynamics of surfactant-laden droplets in turbulence.

The main focus of this chapter is to investigate the effects of a dissolved surfactant on coalescence and breakage phenomena and on the resulting droplet size distribution. The description of coalescence and breakage events is extremely challenging, as they are characterized by a physics acting at many different scales: from the molecular scale of the interface (order of nanometers), to the Kolmogorov scale and up to the largest problem scales (order of meters). This wide range of scales, covering about nine orders of magnitude, cannot be resolved, even with the help of modern supercomputing resources: currently, the range of scales that can be resolved covers three to four orders of magnitude, from the large problem scale down to the smallest turbulence scales. Indeed, the molecular-scale of the interface cannot be resolved and has to be approximated on a much larger scale. Thus, the smaller scales involved in topological modifications of the interface (i.e. coalescences and breakages in this work) are smeared out on the smallest resolved scale. In the following paragraphs the dynamics of breakage and coalescence phenomena will be detailed, particularly focusing on their multi-scale character. This description will be the starting ground to assess the reliability of the numerical description of topological changes of the interface.

From the physical viewpoint, a breakage event can be divided in several stages [114]: (*i*) Thread formation, the shear stresses stretch the droplet and a ligament is formed; (*ii*) Pinch-off, the thread elongates and capillary instabilities pinch-off the ligament (neck formation); (*iii*) Thread breaking, the liquid thread breaks at the pinch-off and the newly formed droplets separate. Upon separation, surface tension reshapes the droplets and the threads are retracted. Overall, breakage is a very quick phenomenon that can be well approximated without resolving the dynamics at the molecular scale; there is evidence that the Navier-Stokes equations alone provide an adequate description of a breakage event [44]. In addition, the small time scale of a breakage limits the impact of the approximation on the overall dynamics of the flow [60, 103, 104]. Therefore, regardless of the methodology used, the description of breakages on turbulence-resolved grids is considered to be rather accurate, although in the pinch-off region the high curvature of the interface may not be perfectly resolved. Breakage events are implicitly described in interface capturing methods [62, 69, 137], while interface tracking methods require suitable closure models to manage the connectivity of the marker points [158, 159]. Fig. 6.1(*a*)-(*d*) shows the numerical simulation of a breakage event, together with the computational grid and the length scale in wall units; panels (*b*)-(*d*) report the different stages of the breakage. Although the grid resolution is sufficient to resolve the Kolmogorov length scale of the turbulent flow (see Sect. 6.1), it is clear from the time-sequence that the physical phenomena occur at length scales smaller than the grid resolution. As discussed before, however, the breakage occurs on a very short time scale, see Fig. 6.1(*c*)-(*d*), so that a rather good numerical representation of this phenomenon is expected.

The dynamics of a coalescence event is more complex compared to that of a breakage, it is influenced by phenomena occurring at very small length scales (order of the molecular scale) and it occurs on larger time scales. From the physical viewpoint, the coalescence process can be divided into the following stages [73]: (*i*) Approach, the two droplets approach each other; (*ii*) Drainage, the thin liquid film between the droplets starts to drain; (*iii*) Coalescence, small scale interactions lead to the rupture of the thin liquid film and to the formation of a coalescence bridge; (*iv*) Reshaping, surface tension forces reshape the droplet. Considering the small scales involved in the film drainage and rupture, the description of a coalescence event in numerical simulations is extremely challenging. In addition, the physical mechanisms driving the film rupture are still being investigated [26, 125, 146], and a correct prediction of the time required for the film rupture cannot be explicitly obtained [73]. Therefore, a part of the physics involved in the coalescence process cannot be resolved or included in the two-phase flow numerical simulations. Current numerical simulations rely on different approaches to describe and/or model coalescence: closure models are required in interface tracking methods [103, 104, 158], while coalescence is implicitly handled in interface capturing methods, where two separate interfaces merge when they are closer than the grid resolution [42, 130, 131]. The current literature standpoint is that, regardless of the specific approach employed to describe coalescence, numerical simulations fail to describe physical coalescence, with this inaccuracy referred to as numerical coalescence. For all interface capturing approaches, numerical coalescence over-predicts physical coalescence, while numerical coalescence for the in-

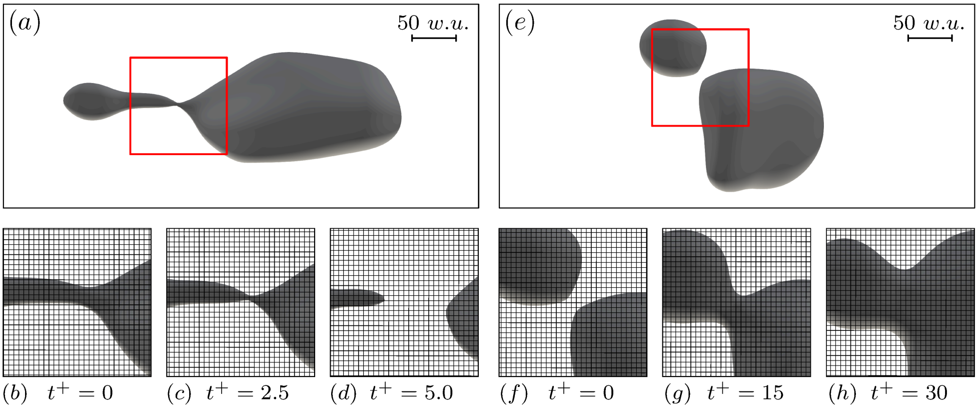

(b) $t^+ = 0$ (c) $t^+ = 2.5$ (d) $t^+ = 5.0$ (f) $t^+ = 0$ (g) $t^+ = 15$ (h) $t^+ = 30$

FIGURE 6.1 – Time sequence of a breakage event, panels (b)-(c)-(d), and of a coalescence event, panels (f)-(g)-(h). The breakage refers to the droplet reported in panel (a) while the coalescence refers to the droplets reported in panel (e). Time increases from the left to the right, the snapshots referring to the breakage event are captured every $\Delta t^+ = 2.5$, while those referring to the coalescence event every $\Delta t^+ = 15$. The panels show a small portion of the domain in the $x^+ - y^+$ plane. Considering the breakage event (left column), the thin thread becomes progressively thinner, panels (c)-(d), and subsequently breaks, panel (e). By opposite, considering the coalescence event (right column), after the initial approach, panel (f), the thin liquid film drains, a bridge is formed and the two droplets merge, panel (g); finally surface tension forces reshape the droplet, panel (h). As a reference, the computational grid employed (which has a uniform grid spacing $\Delta x^+ = \Delta y^+ = 3.68$ wall units) has been also reported. A red box (top row panels) identifies the region of the domain reported in the smaller panels (bottom row).

terface tracking methods depends on the parameters of the coalescence models used. What is the best method to circumvent the issues produced by numerical coalescence is still debated: currently some numerical methods exploit film drainage models [87]. These models, however, are based on strong simplifications (e.g. laminar flow of the film, flat or imposed interface shape, etc.), which might be not fully representative of the real configuration [2, 22] and require the use of *ad hoc* tuned parameters. In Fig. 6.1(e)-(h) the numerical simulation of a coalescence event is reported, together with the computational grid and the length scale in wall units. The different stages of the coalescence are shown in the bottom row, panels (f)-(h). Considering the grid employed, it is clear that the approach, Fig. 6.1(f), the film drainage, the coalescence bridge formation, Fig. 6.1(g), and the reshaping, Fig. 6.1(h), stages can be accurately resolved, while the film rupture (not shown here) is approximated on a much larger scale.

In this work no coalescence or breakage models have been used and the thermodynamic foundations of the phase field method has been preserved. However, to examine the influence of numerical coalescence on the obtained results, a simulation on a much finer grid with twice the number of points in all directions (i.e. $N_x \times N_y \times N_z = 2048 \times 1024 \times 1025$) has been performed. The use of a refined grid allows for the use of a halved thickness of the thin interfacial transition layer (i.e. a halved Cahn number) and, at the same time, allows to mitigate the effect of the numerical coalescence on the results obtained. The comparison of the results obtained on the two grids (coarse: $N_x \times N_y \times N_z = 1024 \times 512 \times 513$; fine:

$N_x \times N_y \times N_z = 2048 \times 1024 \times 1025$) seems to suggest that it is possible to obtain fairly consistent results only slightly influenced by the grid resolution. This fairly good convergence of the results is achieved thanks also to the adoption of a proper scaling between the mobility (Péclet number) and the thickness of the thin interfacial layer [108, 182]. In particular, the coalescence and breakage rates are mildly influenced by numerical coalescence: the rates obtained with the two grids differ by no more than 10%. In addition, the droplet size distributions computed on the two grids (coarse and fine) almost overlap: the only appreciable difference is at small droplet equivalent diameters (see Fig. 6.12), where the higher resolution of the finer grid allows to capture smaller droplets. The simulations here presented seem a fair approximation of the two-phase flow system from the macroscopic point of view (e.g. dispersed phase morphology, coalescence and breakage rates, surfactant distribution). However, it must be underlined that a main shortcoming of these simulations – based on a continuum description of the system – is that the molecular scales physics governing the film drainage and rupture [73] cannot be simulated. Thus, these simulations cannot be used to extract microscopic information on the film rupture and on the role played by the surfactant molecules on such process. Clearly, the importance of including the full physics (and the way in which it is modeled and included) cannot be estimated a-priori on a quantitative basis, and this is still an important open research question.
In the following, first the simulation setup will be introduced (Sect. 6.1), then the distribution of surfactant over the interface of the droplets and the dispersed phase morphology will be characterized in Sect. 6.2. In particular, the droplet size distribution will be quantified and compared with previous theoretical scalings [51], experimental observations [34] and numerical results [142].

6.1 Simulation setup

To investigate the dynamics of a swarm of surfactant-laden droplets a closed channel configuration (no slip condition for the flow field at both walls) is adopted; the channel has dimensions $L_x \times L_y \times L_z = 4\pi h \times 2\pi h \times 2h$, corresponding to $L_x^+ \times L_y^+ \times L_z^+ = 3770 \times 1885 \times 600$ wall units. In this chapter the wall units scaling system (denoted with a $^+$ superscript) will be adopted; please refer to Appendix B for further details on this scaling. The computational domain is discretized with $N_x \times N_y \times N_z = 1024 \times 512 \times 513$ grid points. The flow is driven by an imposed constant pressure gradient in the streamwise (x) direction; all cases are performed at a constant shear Reynolds number, $Re_\tau = 300$.

The Cahn number, setting the thickness of the interfacial layer, has been set according to the grid resolution, $Ch = 0.025$. The phase field Péclet number has been set according to the scaling $Pe_\phi = 1/Ch = 40$ [108, 182], which guarantees the convergence to the sharp interface limit for increasing grid resolution. Increasing the grid resolution (and, thus, the computational cost) allows to reduce the value of the Cahn number and, thus, smaller droplets can be described. However, the dynamics of the droplets can be already captured with the selected grid resolution. Similarly, the penalty flux parameter has been set according to the scaling proposed in Chap. 3: $\lambda = 2.5$ [96, 144].
Two different values of the Weber number have been investigated: $We = 1.50$ and $We = 3.00$. These values are typical of water/oil mixtures [155].

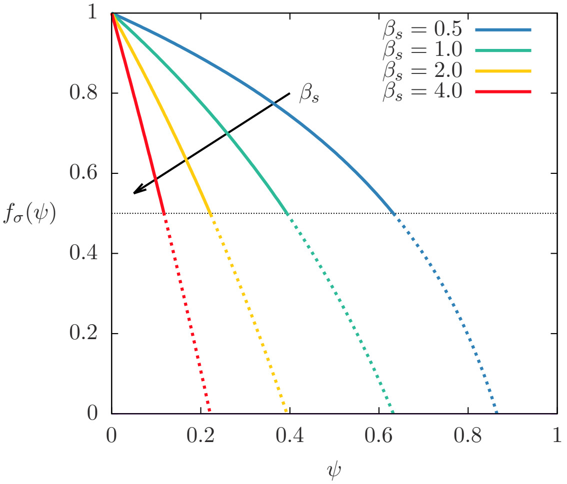

FIGURE 6.2 – Modified Langmuir EOS for all the elasticity numbers, β_s, tested. The surface tension reduction is stronger for higher elasticity numbers (stronger surfactants). According to experimental data, the minimum surface tension has been limited to $f_\sigma = 0.5$ (thin dashed black line). Indeed, experiments observed that surface tension never reduces below this threshold (roughly).

The Péclet number of the surfactant has been set to $Pe_\psi = 100$; this value is representative on nonionic and anionic surfactants in aqueous solutions [172]. The total amount of surfactant is kept fixed in all cases, via the surfactant bulk concentration, $\psi_b = 0.01$. The temperature-dependent parameter, $Pi = 1.35$, and the surfactant solubility parameter, $E_x = 0.117$, have been chosen according to Engblom et al. [47]. The effect of these parameters has not been investigated here; it is expected that for smaller values of E_x and/or higher values of Pi (stronger adsorption and diffusion, respectively) surfactant is more uniformly distributed due to the enhanced diffusion. Four different values of the elasticity number have been tested: $\beta_s = 0.50$ (weaker surfactant), $\beta_s = 1.00$, $\beta_s = 2.00$ and $\beta_s = 4.00$ (stronger surfactant). The modified Langmuir equation of state is reported in Fig. 6.2 for all the elasticity numbers tested. In addition two clean cases (absence of surfactant) have also been performed. A total of ten cases has been run: for each Weber number ($We = 1.50$ and $We = 3.00$) a clean case and four surfactant-laden cases ($\beta_s = 0.50$, 1.00, 2.00 and 4.00) have been performed.

At the beginning of the simulation, a regular array of 256 spherical droplets with diameter $d = 0.4h$ (corresponding to $d^+ = 120$ wall units) is initialized in a fully-developed turbulent channel flow; this flow field is obtained from a preliminary DNS of a single phase flow at $Re_\tau = 300$. The dispersed phase volume fraction is about 5.4% of the total volume. The phase field and the surfactant concentration are initialized with their respective equilibrium profiles: the phase field is constant in the bulk of the phases ($\phi = +1$ in the droplets and $\phi = -1$ in the carrier fluid) and undergoes a smooth transition across the thin interfacial layer. Similarly, the surfactant concentration is uniform in the bulk of the two phases ($\psi = \psi_b$) and reaches its peak value at the interface ($\psi = \psi_0$). At the beginning of the simulation, turbulent fluctuations of the undisturbed flow field strongly perturb the phase field interfacial profile, leading to a reduction of the mass of the dispersed phase. After this initial transient, during which the flow field and the phase field couple together, the mass of each phase keeps constant over time.

While the initial condition chosen for the phase field may seem unrealistic, as a swarm of spherical droplets is suddenly appearing in a single phase flow field, it was proven that the choice of the initial condition does not affect the steady-state results. Indeed, different initial conditions, as for instance the injection of a liquid film at the channel centre, were tested (not reported here): the same statistically steady-state results (coalescence and breakage rates, number of droplets, droplet size distribution) were obtained, indicating that memory of the initial condition is completely lost after an initial transient. The chosen initial condition requires a slightly lower time to reach a steady-state configuration; in addition, the very same initial condition was used in previous works from our group [128, 134, 135]. Thus, to reduce the duration of the transient and to better compare with previous works, the presented initial condition (regular array of spherical droplets) has been chosen.

6.2 Results

The dynamics of the multiphase flow is first analyzed from a qualitative viewpoint, visualizing the distribution and morphology of the dispersed phase and how the surfactant redistributes over the interface. The complex interplay among flow, surface tension and surfactant, which are deeply intertwined, are then investigated. Stretching, breakage and merging of the interface of the droplets are indeed controlled by this interplay, which will better illustrated in the following sections. Then, once laid a general and qualitative picture of the phenomena involved, the qualitative observations will be consolidated with more quantitative analyses. In particular, the surfactant distribution over the interface will be characterized for the various cases (different Weber and elasticity numbers). The analysis will then focus on the morphology of the droplets: the evolution of the number of droplets over time will be investigated and the breakage and coalescence rates will be calculated. The resulting droplet size distribution is then computed and compared with the theoretical scaling proposed by Garrett et al. [51].

6.2.1 Qualitative behavior of the multiphase flow

After the droplets are released in the channel ($t^+ = 0$), each single droplet starts interacting with the neighbouring droplets and with the turbulent flow field. During this initial phase, the flow field, via the shear stresses, deforms the droplets and breakage and coalescence events start to take place. At the same time the flow field and the deformation (i.e. stretching, breaking and merging) of the interface redistribute the surfactant over the interface. After this initial transient, memory of the initial condition (regular array of spherical droplets suddenly appearing in a single phase turbulent flow) is completely lost, and the multiphase flow reaches a new statistically steady-state configuration, shown in Fig. 6.3. This qualitative figure shows the instantaneous

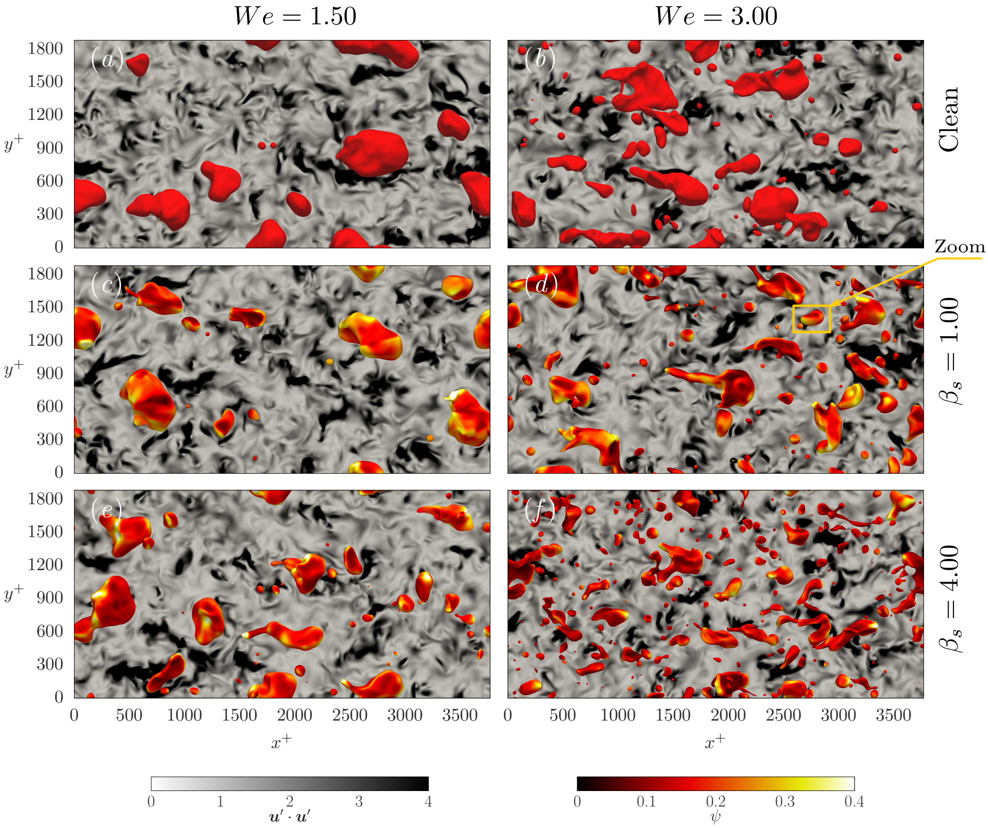

FIGURE 6.3 – Top view of the steady-state configuration ($t^+ = 3750$) for six different cases. The left column, panels (a)-(c)-(e), refers to $We = 1.50$, while the right column, panels (b)-(d)-(f), refers to $We = 3.00$. The first row, panels (a)-(b), refers to the clean cases, the middle row, panels (c)-(d), refers to $\beta_s = 1.00$ and the bottom row, panels (e)-(f), refers to $\beta_s = 4.00$. In each panel, the interface of the droplets (iso-contour $\phi = 0$) is colored in red (clean cases, top row) or by the surfactant concentration (surfactant-laden cases, middle and bottom rows). In the background, a $x^+ - y^+$ plane located at $z^+ = 0$ (centre of the channel) shows the magnitude of the velocity fluctuations, $\mathbf{u}' \cdot \mathbf{u}'$. The yellow box in panel (d) shows the sample droplet used in figure 6.5.

position of the interface of the droplets (iso-contour $\phi = 0$) at $t^+ = 3750$ for six different cases; the left column refers to $We = 1.50$, the right column to $We = 3.00$, while each row corresponds to a different surfactant strength (from top to bottom, clean, $\beta_s = 1.00$ and $\beta_s = 4.00$). The interface is colored in red for the clean case (first row), while, for the surfactant-laden cases (second and third rows), the surfactant concentration over the droplet interface is reported. The magnitude of the fluid velocity fluctuations, $\mathbf{u}' \cdot \mathbf{u}'$, is reported on the mid-plane ($x^+ - y^+$ plane located at $z^+ = 0$) of the channel. Clearly, the Weber number and the elasticity number, both acting on the surface tension, have a strong impact on the morphology of the dispersed phase: as the surface tension decreases, the number of droplets increases and their size, on average, consequently decreases. The lower surface tension weakens surface tension forces, thus favouring interface breakage and the chance of finding high curvature regions. The surfactant concentration changes over the interface of the droplets; in particular larger droplets exhibit a highly non-uniform distribution, while the surfactant concentration on smaller droplets is more uniform. In addition, small regions exhibiting extreme values of the surfactant concentrations (bright yellow/white regions) appear over the droplet interface.

The flow field, represented with the magnitude of the velocity fluctuations at the channel centre, shows minor modifications for different values of the Weber number or of the elasticity number. These modifications can be mainly attributed to the different local morphology of the dispersed phase (which originates from the values of We and β_s): as the surface tension decreases (higher We and/or β_s), regions characterized by high velocity fluctuations (darker area in the picture) are smaller and more fragmented. This difference is better appreciated when comparing the two extreme cases, Fig. 6.3(a) and Fig. 6.3(f).

6.2.2 Shear stresses, Marangoni stresses and interface deformation

As the flow field, the interface and the surfactant concentration are deeply intertwined and they influence each other through complex mechanisms, it is worth to qualitatively introduce these mechanisms and their effects, before starting a more quantitative analysis of the results. A qualitative scheme, reported in Fig. 6.4, will help in explaining the interaction channels among flow field, interface and surfactant concentration. It is clear that the contribution of each factor (flow, interface and surfactant) impacts the others and, thus, it cannot be easily disentangled, due to the feedback from the other factors.

The turbulent flow, and the associated shear stresses, deforms and eventually breaks the interface (shear stresses, top to bottom-right arrow). In addition, the flow sweeps surfactant along the interface, depleting some regions of surfactant and accumulating it in others (shear stresses, top to bottom-left arrow). The surfactant-laden interface, in turn, feeds back onto the flow field via capillary stresses (normal to the interface) and Marangoni stresses (tangential to the interface) according to the local dispersed phase morphology (i.e. local curvature) and surfactant concentration (Capillary and Marangoni stresses, bottom to top arrows). The deformation of the interface (breaking, merging, stretching and compression) favors the accumulation or dilution of surfactant and thus leads to a change in the local surfactant concentration (local curvature, right to left arrow). In addition, the interface curvature influences the adsorption of surfactant from the bulk towards the interface and vice versa [45, 63]. Lastly, surfactant modifies the local surface tension, thus changing the local deformability of the interface (local surface tension change, left to right arrow), and the local shear stress (via the action of Marangoni stresses). The stresses generated by the surfactant-laden interface (capillary and Marangoni stresses) modify the local flow field and shear stresses, which in turn affect the merging, breaking and stretching of the interface and the surfactant distribution. For instance, Marangoni stresses help in preventing coalescence, since they hinder the draining of the liquid film separating the droplets [30, 145]. In a similar way, the modifications of the local flow field produced by

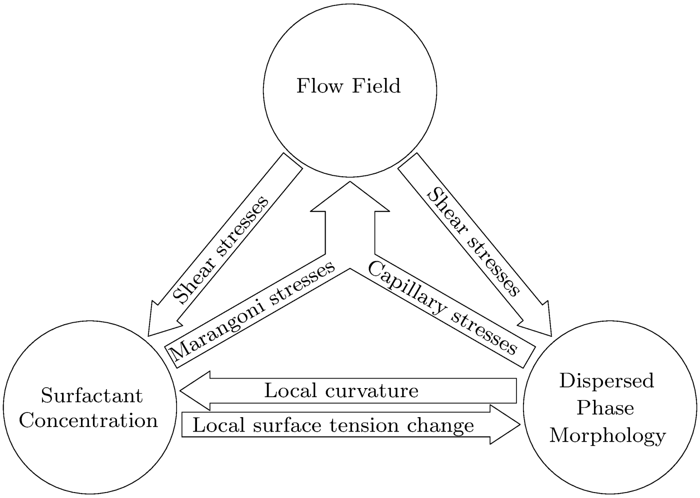

FIGURE 6.4 – Graphic representation of the main interactions among flow field, dispersed phase morphology and surfactant concentration. On one hand, the shear stresses produced by the flow field affect the dispersed phase morphology and the surfactant distribution (top to bottom arrows). On the other hand, capillary and Marangoni stresses influence the local flow field (bottom to top arrows). Then, also the dispersed phase morphology and the surfactant concentration mutually interact: the surfactant distribution locally reduces surface tension and increases the interface deformability (left to right to arrow). This effect is reflected in the interface morphology and dynamics, which in turn affect the surfactant distribution (right to left arrow).

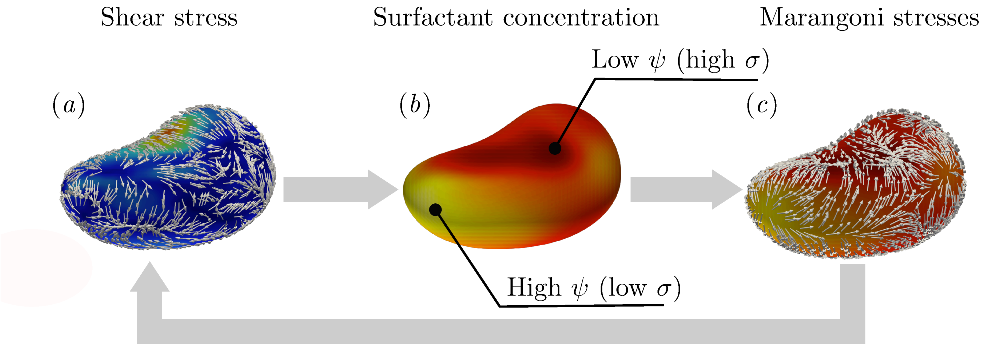

FIGURE 6.5 – Sketch of the coupling between shear and Marangoni stresses. The sketch is realized considering the droplet marked by the yellow box in figure 6.3(d). Panel (a) shows the component tangential to the interface of the shear stresses, $\mathbf{S}_t$, on the droplet interface and normalized by its magnitude. The interface is colored by the shear stress magnitude (blue–small; red–large). Panel (b) shows the resulting non-uniform surfactant distribution (red–low; yellow–high). This distribution, in turn, leads to a non-uniform surface tension distribution and thus gives rise to Marangoni stresses, shown in panel (c) using unit length vectors. These stresses try to restore a uniform value of the surface tension driving flow from high surfactant concentration regions (yellow) towards regions with a lower concentration (red). Marangoni stresses feeds back onto the local shear stresses distribution (right to left arrow).

Marangoni stresses are crucial in the breakage of droplets [147] and in the pinch-off of liquid threads [72].

The feedback loop shear stresses–surfactant concentration–Marangoni stresses is reported in Fig. 6.5: the shear stresses are shown in panel (a), the surfactant concentration in panel (b) and Marangoni stresses in panel (c). The sample droplet is taken from the case $We = 3.00$, $\beta_s = 1.00$ at $t^+ = 3750$ (yellow box in Fig. 6.3(d)). The shear stresses, blue to red colormap in Fig. 6.5(a), and, in particular their component tangential to the interface $\mathbf{S}_t$ (shown as unit-length vectors over the interface in the same panel), advect surfactant over the droplet interface and deform the interface (which, as was presented before, contributes to the local depletion/accumulation of surfactant). The shear stress for an incompressible flow with constant viscosity is defined as:

$$S_x = \tau_{yz} = \frac{1}{Re_\tau}\left(\frac{\partial v}{\partial z^+} + \frac{\partial w}{\partial y^+}\right), \tag{6.1}$$

$$S_y = \tau_{xz} = \frac{1}{Re_\tau}\left(\frac{\partial u}{\partial z^+} + \frac{\partial w}{\partial x^+}\right), \tag{6.2}$$

$$S_z = \tau_{xy} = \frac{1}{Re_\tau}\left(\frac{\partial u}{\partial y^+} + \frac{\partial v}{\partial x^+}\right). \tag{6.3}$$

This stress can be divided in a component normal to the interface, $\mathbf{S}_n$, and one tangential to the interface, $\mathbf{S}_t$:

$$\mathbf{S} = \underbrace{(\mathbf{S}\cdot\mathbf{n})\mathbf{n}}_{\text{Normal}} + \underbrace{\mathbf{S} - (\mathbf{S}\cdot\mathbf{n})\mathbf{n}}_{\text{Tangential}}, \tag{6.4}$$

where $\mathbf{n} = -\frac{\nabla\phi}{|\nabla\phi|}$ is the unit vector normal to the interface (outward-pointing normal). The generated non-uniform surfactant distribution, Fig. 6.5(b), generates a non-uniform surface tension, which, in turn, introduces Marangoni stresses, reported as unit-length vector in Fig. 6.5(c). Marangoni stresses are proportional to the surface tension gradient (roughly speaking to the surfactant concentration, red to yellow colormap in Fig. 6.5) and act to restore a uniform surface tension over the interface by sweeping surfactant from high concentration regions (low surface tension, yellow) towards low concentration regions (high surface tension, red), thus contrasting the action of the tangential shear stresses $\mathbf{S}_t$ (right to left arrow, feedback onto the shear stress).

6.2.3 Probability density function of interfacial surfactant concentration

In the previous section the effects of shear stresses, Marangoni stresses, adsorption/desorption phenomena and interface deformation in transporting surfactant have been introduced. To better characterize the generated surfactant distribution, the probability density function (PDF) of the surfactant concentration at the interface, defined as the iso-contour $\phi = 0$, is computed. The PDF has been computed once the multiphase system attained a steady-state configuration, $t^+ \geq 2500$ for all cases.

At the lower Weber number, $We = 1.50$, the PDF are asymmetric and right-skewed: stronger positive fluctuations in the surfactant concentration are more likely to occur, while strong negative fluctuations rarely happen. As the surfactant strength increases (higher elasticity number), the PDF becomes more asymmetric and the mean value of the interfacial surfactant concentration shifts towards lower values. This shift can be traced back to the increase of the total interfacial area, originating from a larger number of droplets with a more deformable interface. This effect is more pronounced for stronger surfactants (higher elasticity numbers), which indeed are more effective in reducing surface tension: surfactant distributes over the droplets interface, thus a larger interface extension reduces the average surfactant concentration. The different cases (different elasticity numbers) require however a specific discussion: as will be clarified in the following, the strongest surfactant case, $\beta_s = 4.00$, requires a separate analysis. For the other three cases ($\beta_s = 0.50$, $\beta_s = 1.00$ and $\beta_s = 2.00$), the PDF narrows about its peak as the elasticity number is increased. Indeed, Marangoni stresses, acting to restore a uniform value of the surface tension, favor a more uniform surfactant concentration over the interface. As reflected in the PDFs, Marangoni stresses are more effective for stronger surfactants: the magnitude of Marangoni stresses is proportional to the elasticity number. The positive skew of the PDFs is linked to the boundedness of the surfactant concentration: the chemical potential of the surfactant concentration, Eq. (2.62), strictly bounds the surfactant concentration values in $\psi \in (0, 1)$. Thus, low values of the surfactant concentration are strongly penalized. Turning to the strongest surfactant case, $\beta_s = 4.00$, it can be observed how the PDF is remarkably different from the previously described cases: the most probable value of the PDF is lower (with respect to $\beta_s = 2.00$) and the shape is more right-skewed. This different behavior can be traced back to the limited effect of Marangoni stresses: the surface tension is bounded (lower bound, see Eq. (2.26), and above a critical surfactant concentration value, here referred as shutdown concentration ψ_s, surface tension remains constant and the action of Marangoni stresses ceases. The shutdown concentration, ψ_s, can be computed from the surface tension EOS by imposing $f_\sigma(\psi_s) = 0.5$:

$$\psi_s(\beta_s) = 1 - e^{-0.5/\beta_s} \, . \tag{6.5}$$

The resulting shutdown concentrations ($\psi_s = 0.117$ for $\beta_s = 4.00$, $\psi_s = 0.221$ for $\beta_s = 2.00$ and $\psi_s = 0.393$ for $\beta_s = 1.00$) have been reported in Fig. 6.6(a) with thin dashed vertical lines (same colors as the corresponding PDF). The shutdown concentration for the weakest surfactant ($\beta_s = 0.50$) is not shown, since it exceeds the plot limits. It can be seen from Fig. 6.6(a) that the shutdown of Marangoni stresses affects only marginally the distribution of surfactant for $\beta_s = 2.00$ and lower, while most of the surfactant concentration values fall above the shutdown concentration for $\beta_s = 4.00$. Indeed, for this latter case, the shutdown occurs at concentrations lower than the most probable value. Therefore, for the strongest surfactant case, surface tension is constant for $\psi \geq 0.117$ and Marangoni stresses vanish, thus eliminating their feedback action on the shear stresses; this results in a wider and more asymmetric PDF.

For the cases at $We = 3.00$, Fig. 6.6(b), the PDF of the surfactant concentration follows a monotonic trend: large fluctuations in the surfactant concentration are less frequent and the most probable value shifts towards lower concentrations for increasing

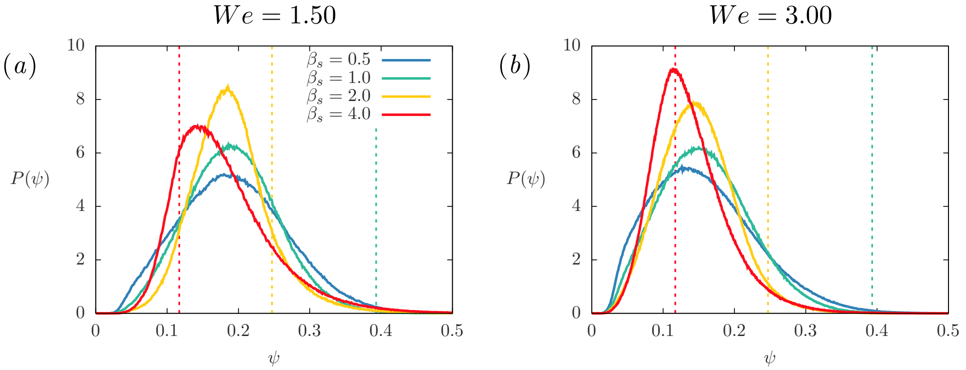

FIGURE 6.6 – Probability density function (PDF) of interfacial surfactant concentration. Panel (a) refers to $We = 1.50$ while panel (b) refers to $We = 3.00$. The different colors refer to $\beta_s = 0.50$ (blue), $\beta_s = 1.00$ (green), $\beta_s = 2.00$ (yellow) and $\beta_s = 4.00$ (red). The concentration at which the shutdown of Marangoni stresses occurs (shutdown concentration, ψ_s) is reported with thin dashed lines (same colors as before). In general, for higher elasticity numbers, the PDF becomes taller and narrows around the most probable value. However, for the cases at $\beta_s = 4.00$, the shutdown of Marangoni stresses drastically affects the PDF shape. This modification is particularly evident for $\beta_s = 4.00$ and $We = 1.50$, red line in panel (a).

elasticity numbers. These two observations directly reflect the action of Marangoni stresses, which favor a more uniform surfactant concentration. Interestingly, for the cases here considered ($We = 3.00$), the shutdown of Marangoni stresses has a minor impact on the shape of the PDF. Indeed, the higher Weber number (lower clean reference surface tension) leads to a much larger total interfacial area, thus the average concentration is lower. As a consequence, the resulting PDFs of these latter cases are shifted towards lower concentrations and a smaller portion of the PDF is influenced by the shutdown of Marangoni stresses. This minor impact of the shutdown of Marangoni stresses is clearly reflected in the PDFs: as the elasticity number is increased, the PDFs narrow and the amplitude of the PDFs peak continuously increases. However, for the highest elasticity number ($\beta_s = 4.00$), the effect of the shutdown is still visible and the respective PDF is strongly skewed to the right. Indeed, for this latter case, the shutdown concentration, $\psi_s = 0.117$, is slightly larger than the peak of the PDF. Therefore, only the part located to the right of the PDF peak is influenced by the shutdown. Finally, we can observe that for the two lower β_s, the boundedness of the surfactant concentration ($\psi > 0$) penalizes large negative fluctuations and affects the left tail of the distribution. This results in a more asymmetric PDF, especially for the lower elasticity numbers, as the PDF is wider (weaker restoring effect of Marangoni stresses) and shifted towards lower concentrations (larger interfacial area).

The surface divergence of Marangoni stresses has been computed over the interface to better characterize the dynamics of surfactant and the effect of Marangoni stresses. In the following, to keep a more compact notation, Marangoni stresses are defined as $\mathbf{M}$:

$$\mathbf{M} = \frac{3}{\sqrt{8}} \frac{Ch}{We} \nabla f_\sigma(\psi) \cdot \overline{\tau}_c \, . \tag{6.6}$$

The surface divergence allows to identify sinks and sources over the interface: sinks are

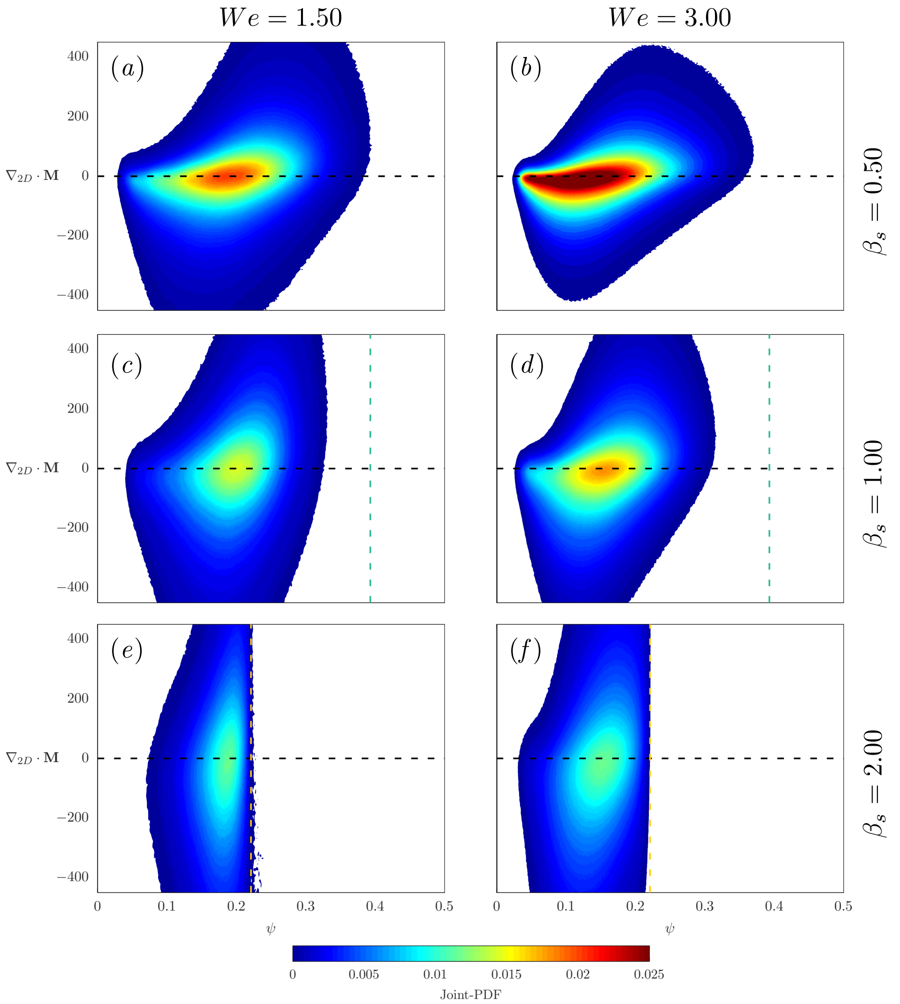

FIGURE 6.7 – Joint Probability Density Function (PDF) of the local surfactant concentration and of the surface divergence of the Marangoni stress. A black dashed line marks the zero-surface divergence. Colored dashed lines identify the shutdown surfactant concentration; for the cases at $\beta_s = 0.50$ the shutdown concentration is beyond the limits of the plot ($\psi_s = 0.63$). The columns correspond respectively to the cases at $We = 1.50$ (left) and $We = 3.00$ (right); each row correspond to a different elasticity number (increasing from top to bottom). The cases at the highest elasticity number have not been reported due to the extremely low shutdown concentration.

characterized by a negative value of the surface divergence, while sources by a positive value. The surface divergence of the Marangoni stress over the interface is calculated as:

$$\nabla_{2D} \cdot \mathbf{M} = \mathbf{n} \cdot \nabla \times (\mathbf{n} \times \mathbf{M}) \,, \tag{6.7}$$

with $\mathbf{n}$ being the unit-length vector normal to the interface. Here, the surface divergence of Marangoni stresses has been correlated with the local surfactant distribution, Fig. 6.7. In particular, it can be observed that sinks of Marangoni stresses well correlate with low surfactant concentration values, while sources with high surfactant concentration values. This result indicates how shear stresses and interface deformation dominate over Marangoni stresses in determining the surfactant distribution: Marangoni stresses are generated by the surfactant distribution and have a limited effect in restoring a uniform surfactant distribution. The restoring effect of Marangoni stresses can be appreciated for increasing values of the elasticity number: the range of surfactant concentration values is narrowed for stronger surfactants. Then, for surfactant concentrations above the shutdown value surface tension keeps constant and Marangoni stresses vanish.

6.2.4 Droplet size influence on the interfacial surfactant concentration

Once the general distribution of surfactant over the interface of the droplets has been characterized, the second qualitative result obtained from Fig. 6.3 can be tackled: surfactant is more uniformly distributed on smaller droplets. For this purpose, the PDF of the surfactant concentration over the interface has been calculated separately for each droplet and then sorted depending on the droplet size. For each droplet, we compute the equivalent diameter, d^+_{eq}, as the diameter of an equivalent spherical droplet with the same volume of the droplet considered:

$$d^+_{eq} = \left(\frac{6V^+}{\pi}\right)^{1/3}, \tag{6.8}$$

where V^+ is the volume of the droplet.

For the sake of clarity, only the mean value, the 5^{th} and 95^{th} percentiles of the surfactant concentration over the droplet interface have been reported in Fig. 6.8; solid lines identify the mean value, while dashed lines correspond to the percentiles (5^{th} percentile below the mean value and 95^{th} percentile above the mean value). The usual color scheme is adopted to distinguish among the various cases: $\beta_s = 0.50$ (blue), $\beta_s = 1.00$ (green), $\beta_s = 2.00$ (yellow) and $\beta_s = 4.00$ (red).

Starting from the lower Weber number, $We = 1.50$ in Fig. 6.8(a), it can be noticed that the mean surfactant concentration on the interface is not significantly influenced by droplet size. This indicates that the mixing effect induced by the coalescence and breakage events promotes a uniform surfactant distribution over the entire range of droplet sizes. A slight trend for the mean surfactant concentration can be observed for increasing elasticity numbers: as the elasticity number is increased (stronger surfactant), the number of droplets increases and so does the total interfacial area, leading to a slight reduction of the mean surfactant concentration. This result is in agreement with the previous observation on the PDF of the surfactant concentration (Fig. 6.6): the lower surface tension (stronger surfactant) increases the total interfacial area, thus reducing the average surfactant concentration over the interface. While the droplet size does not change the mean concentration of surfactant over the interface, a clear effect of the droplet size on the surfactant concentration fluctuations can be appreciated: the 5^{th} and 95^{th} percentiles lines are closer to the mean value for smaller droplets. This means that smaller droplets have a more uniform surfactant distribution over their interface with respect to larger droplets, as observed in Fig. 6.3. This effect can

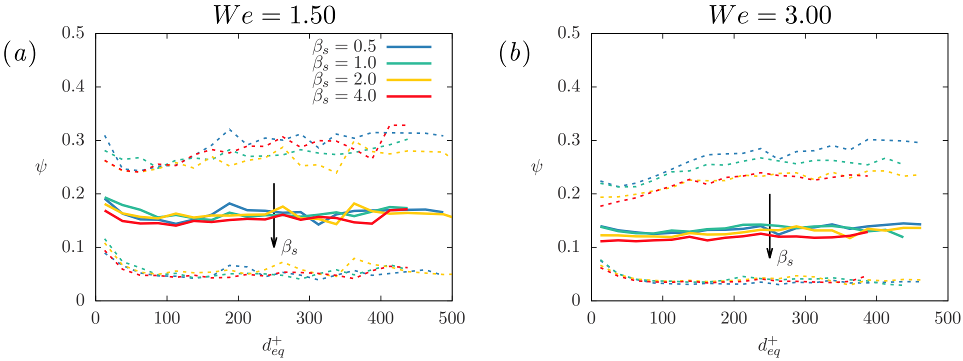

FIGURE 6.8 – Influence of droplets size on surfactant concentration at the interface; thick solid lines represent the mean surfactant concentration, while dashed lines represent the 5^{th} and 95^{th} percentiles. Panel (a) refers to $We = 1.50$ while panel (b) refers to $We = 3.00$. The different cases are marked with different colors: $\beta_s = 0.50$ (blue), $\beta_s = 1.00$ (green), $\beta_s = 2.00$ (yellow) and $\beta_s = 4.00$ (red). The mean concentration is almost constant and is not affected by the droplet size; conversely, the droplet size has an influence on the fluctuations in the surfactant concentration (as indicated by the percentile lines) and smaller droplets exhibit a more uniform concentration. This effect originates from Marangoni stresses, which are more effective on smaller droplets (smaller length scale).

be traced back to Marangoni stresses, the magnitude of which is proportional to the surface tension gradient. The surface tension gradient can be approximated as the ratio of the surface tension variation, $\Delta\sigma$, over the droplet equivalent diameter, here used as a characteristic length scale of the droplet. It is important to note that, for the higher elasticity number considered here ($\beta_s = 4.00$), the shutdown of Marangoni stresses has a remarkable effect on the positive fluctuations in the surfactant concentration: as Marangoni stresses vanish (surface tension is constant for surfactant concentrations above the shutdown concentration), their restoring effect on the surfactant distribution ceases. Indeed, the trend of the 95^{th} percentile line is lost for the stronger surfactant ($\beta_s = 4.00$), which is superposed to the 95^{th} percentile line of the case at $\beta_s = 2.00$. Considering the 5^{th} percentile lines, a similar trend can be observed among all the cases; this trend is particularly marked for larger droplets, $d^+_{eq} > 100$. This effect arises from the surfactant chemical potential, which strictly bounds the surfactant concentration between 0 and 1: thus, extremely low values of surfactant concentration are energetically unfavorable (high chemical potential) and strong negative fluctuations are hindered.

The effect of the droplet size on the surfactant distribution becomes more pronounced for $We = 3.00$, Fig. 6.8(b). A decrease in the mean surfactant concentration is observed for increasing elasticity numbers: the same total amount of surfactant distributes over a larger surface (higher interfacial area). As observed for $We = 1.50$, Fig. 6.8(a), the mean surfactant concentration does not depend on the droplet size, while the amplitude of the fluctuations increases with the droplet size. In particular, a clear trend is observed for the 95^{th} percentile: as the elasticity number increases, Marangoni stresses become stronger and extreme values of surfactant concentration are less likely to occur. Due to the shutdown of Marangoni stresses this trend is not observed between the cases with $\beta_s = 2.00$ and $\beta_s = 4.00$: for this latter case surface tension keeps constant above the shutdown concentration ($\psi_s = 0.117$) and, consequently, the action of Marangoni stresses vanishes. As the equilibrium-restoring effect of Marangoni stresses is partially lost, similar positive fluctuations of the surfactant concentration are observed for the two stronger surfactants ($\beta_s = 2.00$ and $\beta_s = 4.00$). Also for these cases, the boundedness of the surfactant chemical potential (which prevents large negative fluctuations of the surfactant concentration), leads to a very similar behavior for all the 5^{th} percentile lines.

6.2.5 Time evolution of the number of droplets

The distribution of the surfactant over the droplets interface has direct consequences on the dispersed phase morphology. In fact, the presence of surfactant produces a local decrease of surface tension (whose amplitude depends on the local surfactant concentration) and introduces Marangoni stresses, thus affecting the dynamics of coalescence and breakage events and the resulting dispersed phase morphology [30, 98, 151]. To characterize the dispersed phase morphology the time evolution of the number of droplets, $N(t^+)$, over time is computed. The results, normalized by the initial number of droplets $N_0 = 256$ (same for all the cases), are shown in Fig. 6.9.

For the lower Weber number, $We = 1.50$, all cases evolve in a similar manner: a steady decrease in the total number of droplets is observed down to about 40% of the initial value. Then, the five cases start to depart one from each other: the effect of surfactant and of its strength is clearly reflected in the number of droplets. The clean and weak surfactant cases show a faster decrease in the number of droplets with respect to the strong surfactant cases. Finally, at $t^+ \simeq 2500$, a steady-state for the number of droplets is reached, indicating that coalescence and breakage events balance out. The effect of surface tension on the steady-state number of droplets is clear: the clean case has the lowest number of droplets at the end of the simulation and, as the elasticity number is increased, also the final number of droplets increases. On average stronger surfactants are able to produce a higher number of smaller droplets in the channel. The different number of droplets attained at steady-state can be linked to the maximum stable diameter [61], which is determined by the competition between stabilizing effects (e.g. surface tension) and destabilizing effects (e.g. turbulent fluctuations). Decreasing the average surface tension over the interface (stronger surfactant) leads to a reduction in the maximum stable diameter, thus to the formation of smaller droplets. The effect of surfactant can be better appreciated in the inset, which shows the time-evolution of the number of droplets at steady-state. With respect to the clean case, the final number of droplets is increased by a factor ranging from 1.32 ($\beta_s = 0.50$) up to 3.32 ($\beta_s = 4.00$).

A remarkably different behavior is observed for the cases at $We = 3.00$, Fig. 6.9(b): after an initial decrease (up to $t^+ = 300$) in the number of droplets for all cases, a marked increase is observed for the stronger surfactant cases. For these cases breakage events outnumber coalescence events, thus increasing the total number of droplets: surface tension forces are too weak to prevent breakage of the interface, with respect to the cases at $We = 1.50$. After the initial transient stage, at about $t^+ = 2500$, the number of droplets reaches a statistically steady-state value, which increases with

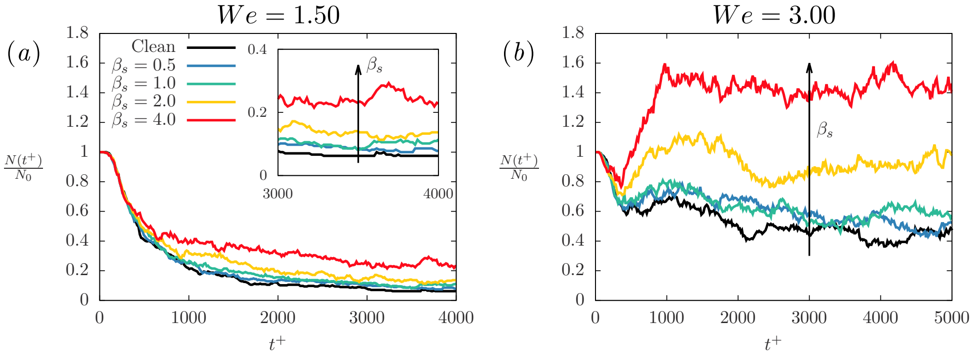

FIGURE 6.9 – Time evolution of the normalized number of droplets, $N(t^+)/N_0$. Panel (a) refers to $We = 1.50$, while panel (b) refers to $We = 3.00$. Different colors distinguish the various cases: clean (black), $\beta_s = 0.50$ (blue), $\beta_s = 1.00$ (green), $\beta_s = 2.00$ (yellow) and $\beta_s = 4.00$ (red). The surfactant action can be clearly observed: increasing the elasticity number β_s, the surface tension reduction is larger and a higher number of droplets is found in the channel. At the lower Weber number, $We = 1.50$, this effect can be better appreciated in the inset of panel (a).

the surfactant strength. In particular, the number of droplets in the clean and weak surfactant cases ($\beta_s = 0.50$ and $\beta_s = 1.00$) reaches a steady-state value of about $N(t^+) \simeq 0.5N_0$, while for the stronger surfactant ($\beta_s = 4.00$) it reaches about $N(t^+) \simeq 1.5N_0$. With respect to the clean case, the steady-state number of droplets is increased by a factor ranging from 1.18 ($\beta_s = 0.50$) to 3.16 ($\beta_s = 4.00$). It is worth noting that although the steady-state number of droplets strongly differs among the two Weber numbers, ranging between 19 (clean case) and 63 ($\beta_s = 4.00$) for $We = 1.50$ and between 116 (clean case) and 366 ($\beta_s = 4.00$) for $We = 3.00$, the increase in the number of droplets with respect to the clean reference cases is similar: from a factor of about 1.25 for the weakest surfactant ($\beta_s = 0.50$) up to about 3.25 for the strongest one ($\beta_s = 4.00$).

6.2.6 Coalescence and breakage rates

The number of droplets, while still being an important information, does not give any information on the actual number of coalescence or breakage events occurring, but just on their balance. To obtain a better insight on the surfactant effects on the morphology of the dispersed phase, the droplets population balance has been considered. In particular, in all the cases presented here, the number of droplets can be modified only by coalescence and breakage events [43, 92]; an overview of the algorithm used to detect coalescence and breakage events is reported in Appendix A. Hence, the following balance equation can be used to describe the time evolution of the number of droplets:

$$\frac{dN(t^+)}{dt^+} = \dot{N}_c(t^+) + \dot{N}_b(t^+)\,, \tag{6.9}$$

where $\dot{N}_c(t^+)$ and $\dot{N}_b(t^+)$ are respectively the coalescence and the breakage rates, i.e. the number of coalescence/breakage events occurring in a unitary time. Predictions of

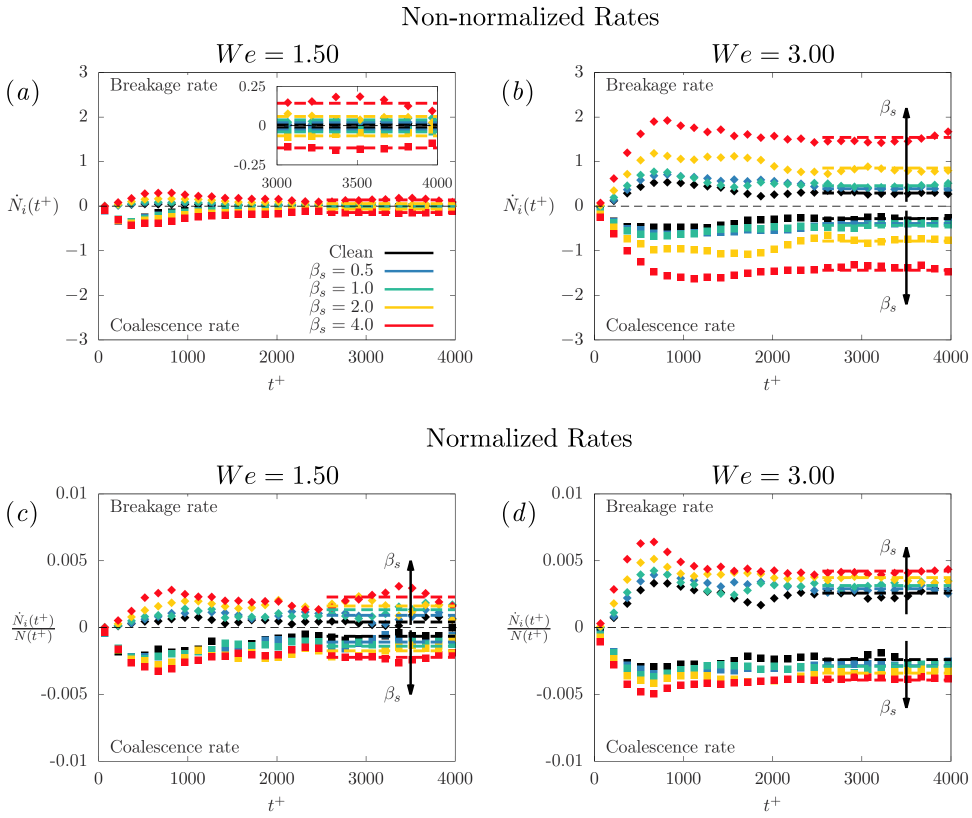

FIGURE 6.10 – Time evolution of the coalescence rate, $\dot{N}_c(t^+)$, and of the breakage rate $\dot{N}_b(t^+)$. The rates are shown non-normalized in panels (a)-(b) and normalized by the actual number of droplets, $N(t^+)$, in panels (c)-(d). Breakage rates, as they increase the number of droplets, are represented as a positive quantity, while coalescence rates, as they reduce the number of droplets, are reported as a negative quantity. Panels (a) and (c) refer to $We = 1.50$ while panels (b) and (d) refer to $We = 3.00$. In all the panels, the steady-state values are reported with thick dashed lines. For both the Weber numbers considered, the addition of a soluble surfactant leads to an increase (in magnitude) of both coalescence and breakage rates. This increase is larger when stronger surfactants are considered (larger elasticity numbers, β_s).

these rates are extremely difficult, as many different factors are involved in the complex dynamics of interface breaking and merging [29, 97, 106, 160, 162]. The problem further complicates when a soluble surfactant, which modifies the interfacial dynamics, is added to the multiphase system. Indeed, as shown in previous investigations performed in laminar flow conditions considering two equal size droplets, the presence of a surfactant prevents (or at least delays) their coalescence [30, 47, 145, 176], but at the same time it also promotes droplet breakage [10, 98].

Fig. 6.10 shows the time evolution of the coalescence and breakage rates for the different cases examined. The rates have been calculated considering the number of coalescence and breakage events, N_c and N_b, occurring in a time window $\Delta t^+ = 90$:

$$\dot{N}_c(t^+) = \frac{N_c}{\Delta t^+}\,, \qquad \dot{N}_b(t^+) = \frac{N_b}{\Delta t^+}\,. \tag{6.10}$$

The coalescence and breakage rates are reported non-normalized, Eq. (6.10), in Fig. 6.10(a)-(b) and normalized by the actual number of droplets, $N(t^+)$, in Fig. 6.10(c)-(d).

For the cases at $We = 1.50$, Fig. 6.10, the coalescence rate is larger than the breakage rate (in magnitude) during the initial transient. This results in a reduction of the number of droplets, see Fig. 6.9(a). After reaching a peak value at $t^+ \simeq 600$, the two rates start to smoothly decrease until a steady-state value is reached for $t^+ > 2500$, after which the average coalescence and breakage rates (dashed lines) are equal (in magnitude). Comparing the different cases, it can be noted how stronger surfactants (larger β_s) increase both breakage and coalescence rates. While the former effect is expected (a lower average surface tension increases the likelihood of the interface breaking), the latter effect is not as obvious. Indeed, previous works [30, 47, 145, 176] showed that surfactant hinders the coalescence of two droplets, while here we observe an increase of the coalescence rate for stronger surfactants. However, differently from the previous works [30, 47, 145, 176], in the cases presented here, the average droplet size and the number of droplets differ among the different cases. This difference influences the results obtained for the coalescence and breakage rates: stronger surfactants (i.e. higher elasticity numbers) lead to the formation of a higher number of smaller droplets which are less deformable and will more likely coalesce (faster drainage of the thin liquid film separating the two droplets). In addition, the higher number of droplets present in the channel increases the chances of droplets collision and of a subsequent coalescence. Thus, the increase of the coalescence rate for increasing elasticity numbers can be addressed to the different size of the droplets.

To remove the influence of the number of droplets in the coalescence and breakage rates, the rates have been normalized by the actual number of droplets, Fig. 6.10(c). In the initial stages, $t^+ < 1500$, the time evolution of the non-normalized and normalized rates is similar. However, differently from the non-normalized rates, for $t^+ > 1500$, the normalized rates reach a steady-state value. This suggests that the decrease of both breakage and coalescence rates (non-normalized) is due to the lower number of droplets present in the channel. Hence, while the coalescence and breakage rates (non-normalized) can be directly linked to the population balance as they represent the effective change in the number of droplets, the normalized rates give a more general information on the surfactant effects on the coalescence and breakage rates.

For the higher Weber number (lower clean surface tension) a much clearer effect on the coalescence and breakage rates can be observed, Fig. 6.10(b). In the initial transient, both coalescence and breakage rates increase until they reach their peak value at about $t^+ = 600$. After reaching this peak, the coalescence rates are almost constant at their steady-state value, while the breakage rates slightly decrease before reaching a steady-state value. For the stronger surfactant ($\beta_s = 4.00$), the breakage rate during the initial stage of the simulation exceeds the coalescence rate; this feature is reflected in the total number of droplets, Fig. 6.9(b), which for this case at steady-state is much higher than the initial number of droplets, about $1.5N_0$. The surfactant strength has

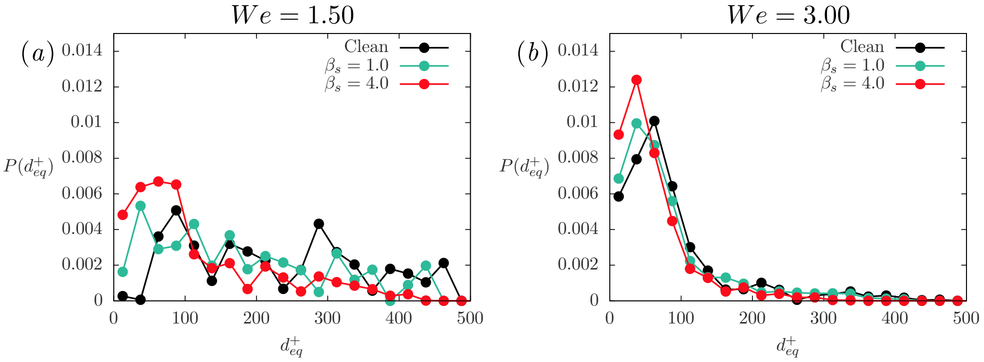

FIGURE 6.11 – Droplet size distribution (DSD) for $We = 1.50$, panel (a) and $We = 3.00$, panel (b). The different colors refer to the clean case (black), $\beta_s = 1.00$ (green) and $\beta_s = 4.00$ (red). For $We = 1.50$, the low number of droplets do not allow to obtain a clear trend; however, on a qualitative basis, it can be observed that increasing the surfactant strength (i.e. the elasticity number β_s), the probability of finding smaller droplets increases. This trend becomes clearer for the higher Weber number, $We = 3.00$: increasing the elasticity number β_s, the presence of small droplets is favored.

a clear effect on the rates: indeed, for larger elasticity numbers, the coalescence and breakage rates are larger (in magnitude). This is a direct consequence of the higher number of smaller droplets present in the channel: these smaller droplets will more likely coalesce (smaller size) and at the same time will more likely undergo breakage (lower surface tension).

Also for these cases, to remove the effect of the number of droplets in the coalescence and breakage rates, the rates have been normalized by the actual number of droplets present in the channel, Fig. 6.10(d). The trend observed are similar to those exhibited by the non-normalized rates and, for higher elasticity numbers, the steady-state values of the coalescence and breakage rates become larger (in magnitude); however, the differences among the cases become smaller. This observation suggests that the higher number of droplets present when larger elasticity numbers are considered produces an amplification of the non-normalized rates. In addition, the peak in the breakage rate exhibited by the two stronger surfactants ($\beta_s = 2.00$ and $\beta_s = 4.00$), becomes more pronounced. This indicates that the strong reduction of the surface tension, induced by the surfactant, strongly favors the breakage of the droplets.

6.2.7 Droplet size distribution

The addition of a soluble surfactant in the system, which modifies the droplet deformability (lower surface tension) and introduces Marangoni stresses, directly influences the coalescence and breakage rates and as a consequence the resulting droplet size distribution (DSD). The DSD is a fundamental tool, which has been extensively used in the past to characterize the dispersed phase morphology; several empirical models for the calculation of the DSD have been proposed in the past [7, 94, 168]. The DSDs for all the different cases (clean and surfactant-laden) have been computed using the droplet equivalent diameter as a measure of the droplet size. The distributions have been computed once the simulations reached a steady condition ($t^+ > 2500$). The results are shown in Fig. 6.11; the two panels correspond to $We = 1.50$ and $We = 3.00$, respectively panels (a) and (b). To better highlight the differences among the different cases, only three cases are reported: clean (black), $\beta_s = 1.00$ (green) and $\beta_s = 4.00$ (red).

The low number of droplets at $We = 1.50$ does not allow to obtain a clear statistic (especially for the clean case). However, a trend for increasing surfactant strength can still be appreciated: smaller droplets are more likely to be found as the elasticity number is increased. Indeed, for the stronger surfactant ($\beta_s = 4.00$), the DSD peaks for $d^+_{eq} < 100$ and falls almost to zero for larger droplet sizes. Conversely, for the clean case there is a low probability of having very small droplets, $d^+_{eq} < 50$, and a much higher probability of having larger droplets, $200 < d^+_{eq} < 500$. This observation can be directly linked to the average surface tension reduction produced by the surfactant: for higher elasticity numbers (larger surface tension reduction), larger droplets are not stable and undergo breakage and, as a consequence, the presence of smaller droplets is favored. This finding is in agreement with the breakage rates, Fig. 6.10(a)-(c), which increase when stronger surfactants are considered.

For $We = 3.00$, Fig. 6.11(b), a higher number of droplets is present and a much clearer trend can be observed. In particular, all the DSDs exhibit a marked peak for small droplet sizes, $d^+_{eq} < 100$; this peak shifts towards smaller diameters and increases its value as the elasticity number is increased. Indeed, for the clean case the peak value is at about $d^+_{eq} \simeq 75$, while it reduces to $d^+_{eq} \simeq 50$ for the two surfactant-laden cases, with the stronger surfactant showing a higher peak value. The probability of having larger droplet sizes, $d^+_{eq} > 200$, is extremely low, at least one order of magnitude lower than the peak value. The effect of the elasticity number can be appreciated also for the larger droplet sizes: a higher probability of finding larger droplets is observed for the clean case and for $\beta_s = 1.00$.

Overall, for both Weber numbers it has been observed that a higher surfactant strength (and, thus, the respective higher surface tension reduction) favors the breakage of the droplets, increasing the likelihood of finding smaller droplets.

6.2.8 Comparison with theoretical scaling

The droplet size distribution is an important quantity used to characterize the morphology of a dispersed phase; indeed several models and scaling have been proposed to predict it. Among these, the most commonly adopted distributions are: normal [13, 25], log-normal [23, 101, 120], Rosin-Rammler [74], Weibull [14], upper limit equation [110] and power law [34, 35, 51, 142]. Although a universal agreement over several decades has not been yet demonstrated, a reasonable number of experimental [34] and numerical [142] works showed a good agreement with the power law scaling proposed by Garrett et al. [51]. According to Garrett et al. [51], the DSD follows a $-10/3$ power law scaling with the droplet diameter. Deane and Stokes [34] showed that this distribution well described the DSD for droplet diameters larger than the relevant breakage scale; this latter scale can be estimated as the droplet maximum stable diameter, commonly referred as the Hinze inviscid scale, d^+_H [61]. For the simulation setup considered

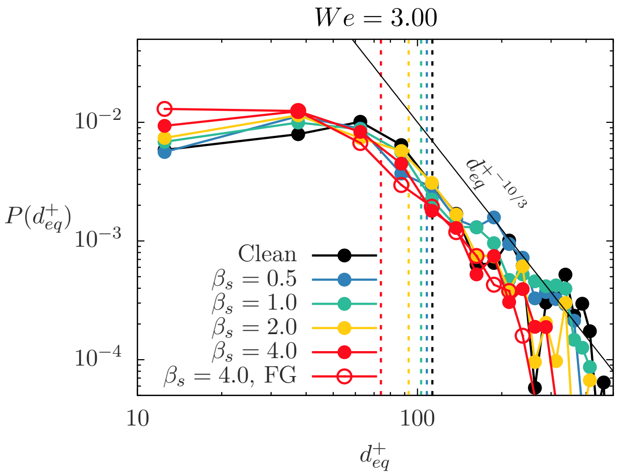

FIGURE 6.12 – Droplet size distributions reported (log-log scale). The results refer to $We = 3.00$ and the various cases are identified with different colors: black (clean), $\beta_s = 0.50$ (blue), $\beta_s = 1.00$ (green), $\beta_s = 2.00$ (yellow) and $\beta_s = 4.00$ (red). The theoretical scaling ${d^+_{eq}}^{-10/3}$ is reported with a thin continuous black line. The Hinze inviscid scale for each case is reported with vertical dashed lines (same color code as the droplet size distributions). The droplet size distributions obtained are in good agreement with theoretical scaling, especially for the larger elasticity numbers (larger number of samples). In addition, to show the effect of the grid resolution on the droplet size distribution, the results obtained from a simulation at $We = 3.00$ and $\beta_s = 4.00$ rerun on a finer grid (refined twice in each direction, $N_x \times N_y \times N_z = 2048 \times 1024 \times 1025$) have been reported with red empty circles.

here, the Hinze inviscid scale can be computed as follows [61, 120, 128]:

$$d^+_H = 0.725 \left(\frac{\sigma_0}{\sigma_{av}} \frac{We}{Re_\tau} \right)^{-3/5} |\varepsilon_c|^{-2/5} , \tag{6.11}$$

where the ratio σ_0/σ_{av} is used to account for the average surface tension reduction produced by the surfactant and ε_c is the turbulent dissipation at the channel centre. Here the equation is used in its dimensionless form (wall units), refer to Appendix B for further details. The turbulent dissipation depends on the distance from the wall; however, since droplets are more likely to be found in the core region of the channel [128, 135], the dissipation at the channel centre is used as a reference. From Eq. (6.11) it can be noted how the Hinze inviscid scale reduces for increasing surfactant strengths (lower average surface tension, σ_{av}).

The DSDs obtained from the larger Weber number, $We = 3.00$, have been reported in a log-log plot and compared with the power law scaling proposed by Garrett et al. [51] in Fig. 6.12. Results at the lower Weber number are not reported here, as the low number of droplets does not constitute a sufficient statistical sample (especially for the clean case); however, a good agreement (not reported here) is found for the highest elasticity number, $\beta_s = 4.00$ (highest number of droplets). In Fig. 6.12, a thin black line identifies the theoretical scaling, ${d^+_{eq}}^{-10/3}$, while thick lines identify the different cases: clean (black), $\beta_s = 0.50$ (blue), $\beta_s = 1.00$ (green), $\beta_s = 2.00$

(yellow) and $\beta_s = 4.00$ (red). The Hinze inviscid scales (maximum stable diameter of the droplet) are reported with dashed vertical lines using the same color code of the DSDs; as the elasticity number is increased, the average surface tension, σ_{av}, reduces, thus decreasing the Hinze inviscid scale.

The resulting droplet size distributions are in good agreement with the power law scaling proposed by Garrett et al. [51] for equivalent diameters larger than the Hinze inviscid scale, $d^+_{eq} > d^+_H$. This latter observation seems to confirm the validity of the scaling for droplets larger than the Hinze inviscid scale, as reported also by Deane and Stokes [34], who analyzed the size distribution of bubbles in breaking ocean waves and by Skartlien et al. [142], who analyzed the size distribution of droplets in surfactant-laden liquid/liquid systems. The quality of the agreement between numerical results and theoretical scaling improves for larger elasticity numbers and, specifically, for the cases $\beta_s = 2.00$ and $\beta_s = 4.00$. Indeed, the considerably higher number of droplets obtained for these cases leads to a smoother DSD over a wider range diameters. In addition, for larger elasticity numbers, the Hinze inviscid scale, d^+_H, shifts towards lower values and the agreement can be observed for a wider range of droplets equivalent diameters. Albeit the good agreement obtained between our results and the scaling proposed by Garrett et al. [51], the data and the range of sizes available are not sufficient to exclude other power law scalings with slightly different exponents [35]. Widening the size span of the droplets would require simulations at a higher Reynolds number; the Hinze inviscid scale is only marginally influenced by the Reynolds number, while the maximum droplet size is roughly the total channel height (which is proportional to the Reynolds number). Addressing this issue would require performing numerical simulations with a much higher computational cost, which are not feasible with the computational resources currently available. However, the impact of the grid resolution on coalescence and breakages (introduced at the beginning of this chapter) and consequently on the resulting droplet size distribution has been addressed here: the case $We = 3.00$, $\beta_s = 4.00$ has been rerun on a finer grid (refined twice in each direction, $N_x \times N_y \times N_z = 2048 \times 1024 \times 1025$) and employing an halved Cahn number, $Ch = 0.012$. Results of this latter simulation are shown using empty red circles in Fig. 6.12. An excellent agreement can be observed comparing the results for the two cases at $\beta_s = 4.00$: the large diameters are not much influenced by the grid resolution, while on the finer grid case more smaller droplets appear. Indeed, the simulation on the refined grid better captures the dynamics of the smaller droplets ($\mathcal{O}(10)$ wall units in size).

6.3 Conclusions

In this chapter the dynamics of a swarm of surfactant-laden deformable droplets in wall-bounded turbulence has been presented, mainly focusing on the surfactant distribution and on the morphology of the droplets. A total of ten different cases has been investigated: two different Weber numbers ($We = 1.50$ and $We = 3.00$) and five different elasticity numbers (clean, $\beta_s = 0.50$, $\beta_s = 1.00$, $\beta_s = 2.00$ and $\beta_s = 4.00$). Both the investigated parameters act on the surface tension: the Weber number uniformly changes the surface tension (clean, reference value), while the elasticity number directly controls the strength of the surfactant (which locally affects surface tension).

The complex interplay among flow, interface and surfactant has been described, showing how these elements are deeply interconnected and feed back onto each other, see Fig. 6.4 and Fig. 6.5. The flow field deforms the interface and advects the surfactant. In turn, the interface feeds back onto the local flow field and modifies the surfactant concentration, as it stretches, breaks and merges. Finally, the surfactant locally modifies the surface tension, increasing the local deformability of the interface and generating Marangoni stresses. These stresses (tangential to the interface) originate from surface tension gradients (i.e. surfactant concentration gradients) and promote a uniform surfactant distribution over the droplets interface. In particular, Marangoni stresses are more effective on smaller droplets, as their magnitude roughly scales with the inverse of the droplet length scale, and indeed the results of the numerical simulations show a more uniform surfactant concentration on smaller droplets. Surface tension determines also the maximum stable size for a droplet: as surface tension forces weaken, larger droplets become unstable and break. Indeed, as either the Weber number, either the elasticity number are increased, more and smaller droplets are found in the channel: as the total volume fraction is kept constant among all the simulations, the reduction of the droplet maximum stable size increases the total number of droplets. In addition, increasing the Weber number or the elasticity number increases also the breakage and coalescence rates. While the former is expected, as surface forces are weakened, the latter is, at first, counterintuitive. The increase in the breakage rate leads to many smaller droplets, which are more likely to coalesce: smaller droplets are less deformable and droplet-droplet collisions are more frequent due to the higher number of droplets. Increases (in magnitude) of coalescence and breakage rates become more pronounced for increasing Weber or elasticity numbers. Finally, it has been shown that the resulting droplets size distribution roughly scales with the inverse of the droplet volume. This observation is in agreement with previous theoretical and computational works: the computed droplets size distribution follows indeed the $-10/3$ theoretical power law scaling proposed by Garrett et al. [51], which was also confirmed by experimental [34] and numerical [142] investigations.

7

Concluding remarks and future developments

The dynamics of surfactant-laden droplets has been characterized throughout this thesis using a two-order-parameter phase field method. A novel numerical approach for the simulation of surfactant-laden interfaces has been presented, Chap. 2 and Chap. 3. In particular, a correction term has also been added to mitigate some of the well-known issues of the classical phase field approach (shrinkage, coarsening and misrepresentation of surface tension and thermo-physical properties); this modified approach has then been extensively tested.

The effects introduced by a dissolved surfactant has been investigated first in simpler laminar cases, Chap. 4 and Chap. 5, and then in a more complex, turbulent case, Chap. 6. The laminar cases allowed to separate and understand the various surfactant effects in a controlled setup (deformation of a droplet in laminar shear flow and binary droplets interactions in laminar flow). In particular, it was found that the average surface tension reduction has a major role in determining the overall droplet deformation, with Marangoni stresses having a negligible contribution, Chap. 4. These latter stresses, however, proved to be fundamental during the interaction of two droplets: together with the average surface tension reduction (i.e. a more deformable interface), Marangoni stresses avoid or, at least delay, the coalescence of the droplets, Chap. 5. Indeed, Marangoni stresses, acting tangentially to the interface, reduce the draining rate of the liquid film in between the two approaching interfaces, hindering coalescence. The surfactant distribution over the interface is then characterized in a more complex setup: a wall-bounded fully-developed turbulent flow, Chap. 6. The distribution of surfactant over the interface is determined by several factors, among which the flow (i.e., the shear stresses), the deformation, breaking and merging of the interface, Marangoni stresses and surfactant diffusion. Marangoni stresses, in particular, favor a uniform surfactant distribution as shown for increasing elasticity numbers (stronger surfactants, i.e. higher surface tension gradients). In addition, the presence of a surfactant phase strongly alters the morphology of the dispersed phase: the total number of droplets increases (and, thus, reduces in size) for increasing surfactant strengths. The reduced surface tension increases the likelihood of interface breaking (higher breakage rate), thus generating a higher number of smaller droplets. These droplets will more likely coalesce (many small and rather rigid droplets), hence the increase observed in the coalescence rates. After an initial transient, the number of droplets, and thus the coalescence and breakage rates, reaches a stationary value, which is higher for increasing surfactant strengths. The resulting droplet size distribution, computed once the dispersed phase morphology has reached steady-state conditions, well agrees with previous theoretical scalings [51], experimental measurements [34] and previous numerical simulations [142].

The proposed numerical approach proved to be a powerful tool for the simulation of multiphase flows laden with a fully soluble surfactant, and implicitly accounts for physically-grounded topological modifications of the interface. The follow-up of this thesis is the simulation of industrially-relevant surfactant-laden multiphase flows, as for instance gas/liquid and high-viscosity oil/water multiphase flows. These mixtures are characterized by high density and/or viscosity ratios between the two phases, thus making their simulation more challenging. An additional improvement that will be considered in the near future is the generalization of the solid wall-interface interactions: in this thesis a static, fixed contact angle has been considered. This choice does not affect anyhow the results presented, as the interface never reaches the solid wall. Including a model for the contact angle dynamics would, however, allow to simulate problems in which the wall is partially wet, as for instance a bubble layer lubricating the solid wall. This setup has shown promising results in several engineering applications, such as lubricating layers of air bubbles or air films covering the hull of ships to reduce the frictional drag [20, 113, 132, 163, 165, 167]. As a future perspective, next-generation phase field approaches might include coalescence models to mitigate numerical coalescences; while, on one hand, the rigorous thermodynamic foundation of the method would be compromised when simulating coalescences, on the other hand a well-tuned coalescence model would strongly reduce the influence of numerical coalescence at a reasonable computational cost. Another viable approach to improve the simulation of interface coalescence could be the use of an Adaptive Mesh Refinement (AMR) scheme to increase the grid resolution in the interfacial region. This strategy, however, contrasts with the pseudo-spectral discretization, thus a different spatial discretization method should be adopted. In addition, an AMR scheme would increase the complexity of data handling and load balancing at simulation run time. These two possibilities, alone or combined, would improve the description of coalescence and breakage and reduce the influence of numerical coalescence, while keeping a fairly reasonable computational cost.

A

Detecting breakages and coalescences

In the following an overview of the method used to detect coalescence and breakage events will be briefly reviewed; Fig. A.2 shows a visual representation of the algorithm. The input data needed are: the position of the center of mass of each droplet at the current time step, $\mathbf{x}^n$, the velocity of the center of mass of each droplet at the current time step, $\mathbf{u}^n$, and the position of the center of mass of each droplet at the following time step, $\mathbf{x}^{n+1}$. These quantities are calculated for each droplet i and are defined as:

$$\mathbf{x^n} = \frac{1}{V_i^n} \int_{V_i^n} \mathbf{x^n} \mathrm{d}V \ , \tag{A.1}$$

$$\mathbf{u^n} = \frac{1}{V_i^n} \int_{V_i^n} \mathbf{u^n} \mathrm{d}V \ , \tag{A.2}$$

$$\mathbf{x^{n+1}} = \frac{1}{V_i^{n+1}} \int_{V_i^{n+1}} \mathbf{x^{n+1}} \mathrm{d}V \ , \tag{A.3}$$

where the integral is computed over the volume V_i of each droplet. The apices n and $n+1$ identify respectively the current and the following time step; the elapsed time between the two time steps is ΔT. In the first step the estimated position of each droplet at the following time step is computed: $\mathbf{x}_{est}^{n+1} = \mathbf{x}^n + \Delta T \mathbf{u}^n$. To better explain the technique employed to detect translations, breakages and coalescences some examples have been reported in Fig. A.1. For each droplet (estimated position), the closest droplet at the following time step is found; at this step some droplets at the following time step may be left out (they are not the closest droplet to any estimated droplet position). This step corresponds to Fig. A.1(a): the estimated position of droplet T_n is calculated (red transparent droplet) and the closest droplet at the following time step is found out (droplet T_{n+1}). In the following stage breakage and coalescence events have to be sorted out from these data.

A breakage is detected whenever a droplet in $\mathbf{x}^{n+1}$ has no parent droplet: according to Fig. A.1(b) droplet $B_{n+1,2}$ has no parent droplet, thus it originated from a breakage event. Once a breakage event is identified, the algorithm searches for the the closest droplet to the droplet $B_{n+1,2}$ at time step $n+1$; in this case droplet $B_{n+1,1}$ is found.

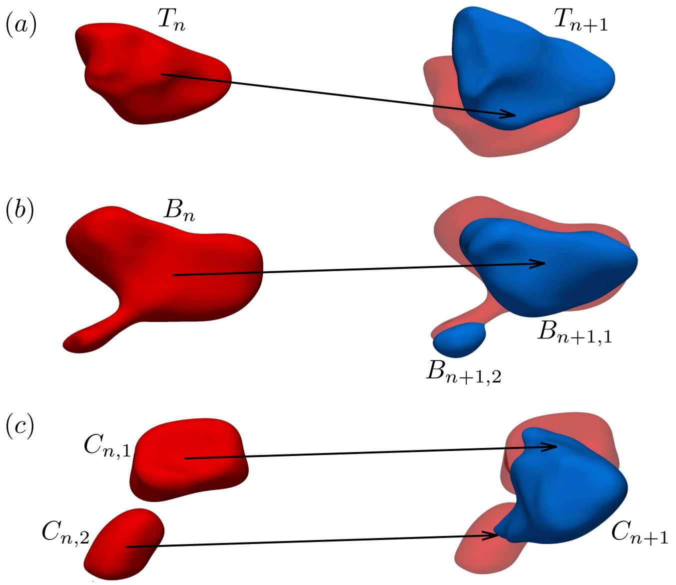

FIGURE A.1 – Possible cases considered: panel (a) corresponds to a translation, panel (b) to a breakage and panel (c) to a coalescence. Red droplets are at the current time step (n), while blue droplets are at the following time step $(n+1)$. Semi-transparent red droplets show the estimated position, $\mathbf{x}_{est}^{n+1}$. Arrows show the trajectory of the droplets, $\Delta T \mathbf{u}$.

It is then assumed that droplet B_n (whose estimated position is the closest to droplet $B_{n+1,1}$) breaks apart into droplets $B_{n+1,1}$ and $B_{n+1,2}$.
Once all breakages have been detected, the algorithm looks for coalescence events. A coalescence event is detected whenever two separate droplets at time step n are assigned to the same droplet at time step $n+1$. In particular, referring to Fig. A.1(c) droplets $C_{n,1}$ and $C_{n,2}$ are both assigned to droplet C_{n+1}, as it is the closest one to their estimated position.
So far, only kinematic criteria have been used to determine the trajectory and eventual interactions (coalescences and breakages) of each droplet. Once all the trajectories at the present time step have been determined, the quality index and the balance are computed. In particular, the quality index, Q, is initialized at the beginning of the time step to the number of droplets at the current time step, N_n; every time volume is not conserved (within a certain small threshold) in all the translation, breakages and coalescences, the quality index is reduced by one. At the end of the time step, it is normalized by N_n. Recalling the examples of Fig. A.1, three checks on the volume conservation are performed depending on the type of event:

$$\begin{cases} V_{T_n} = V_{T_{n+1}} \pm \varepsilon & \text{for translations} \\ V_{B_n} = V_{B_{n+1,1}} + V_{B_{n+1,2}} \pm \varepsilon & \text{for breakages} \\ V_{C_{n,1}} + V_{C_{n,2}} = V_{C_{n+1}} \pm \varepsilon & \text{for coalescences} \end{cases} . \tag{A.4}$$

To account for numerical errors that could occur in the calculation of the volume of

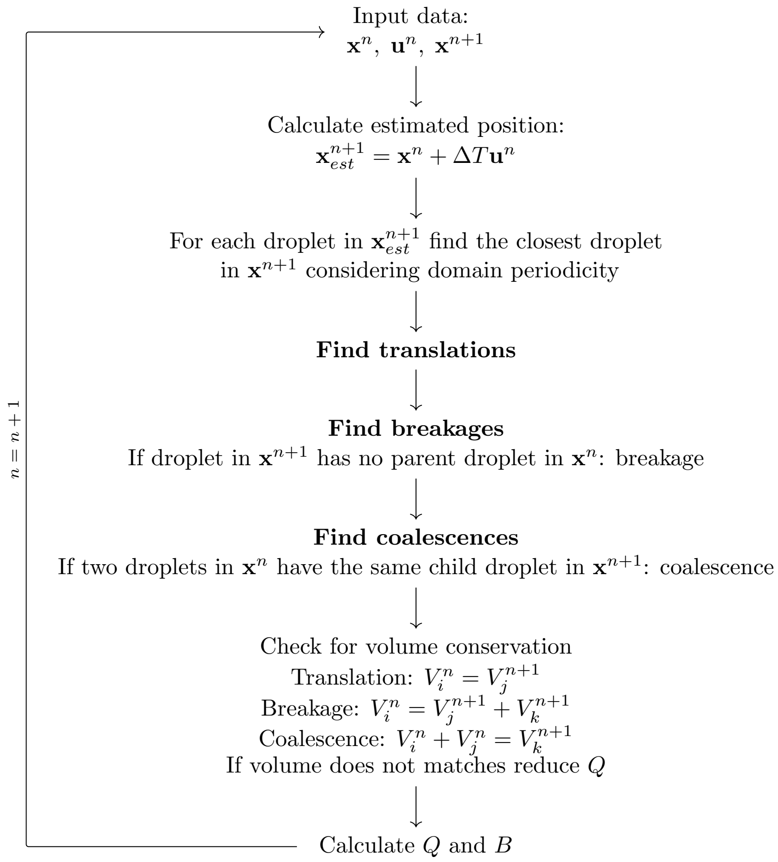

FIGURE A.2 – Flow chart of the method used to detect breakages and coalescences

each droplet (that would strongly reduce the quality index of the matching), a small tolerance ε (of the order of few percents of the volume of the parent droplet) is used when checking for volume conservation.

The second parameter controlling the quality of the calculated trajectories is the balance, B. The total number of droplets at each time step is known: N_n at the current time step and N_{n+1} at the following one. Once the number of breakage and coalescence events is known the balance can be calculated as:

$$B = N_{n+1} - (N_n + N_B - N_C) \ , \tag{A.5}$$

where N_B and N_C are respectively the number of breakage and coalescence events. The number of droplets at the current time step, N_n, is increased whenever a droplet undergoes breakage into two droplets and is decreased whenever two droplets coalesce into one droplet. Thus, considering these two parameters, a fair matching of the trajectories is obtained with a quality index $Q \rightarrow 1$ and a balance $B = 0$. This means that the volume is always matched (quality index never or rarely reduced) and no droplet is left out (balance equal to zero).

Here, only binary breakages and coalescences are considered; this assumption is not particularly limiting, as binary breakages/coalescences have the highest probability of occurrence [4, 6, 107]. This assumption is also confirmed by the simulations performed: the quality index never reduces below 0.85 (so the volume is matched for at least 85% of all the translation, breakage and coalescence events) and at most few droplets are left unmatched (the balance is almost zero).

B

Wall units scaling system

The reference quantities for the wall units scaling system are:

$$\widetilde{\mathbf{x}} = \frac{\nu}{u_\tau}\mathbf{x}^+ \,, \quad \widetilde{\mathbf{u}} = u_\tau \mathbf{u}^+ \,, \quad \widetilde{t} = \frac{\nu}{u_\tau^2} t^+ \,, \quad \widetilde{\phi} = \sqrt{\frac{\beta}{\alpha}}\phi^+ \,, \quad \widetilde{\psi} = \psi^+ \,, \tag{B.1}$$

where the $\widetilde{}$ symbol denotes dimensional quantities, the $^+$ superscript denotes dimensionless quantities (wall units) and $\nu = \eta_c/\rho_c$ is the kinematic viscosity.
The dimensional analysis from dimensional units to outer units (no superscript) has been introduced in Sect. 2.4. From the dimensional analysis for outer and wall units, the following relations can be obtained:

$$\mathbf{x}^+ = Re_\tau \mathbf{x} \,, \quad \mathbf{u}^+ = \mathbf{u} \,, \quad t^+ = Re_\tau t \,, \quad \phi^+ = \phi \,, \quad \psi^+ = \psi \,. \tag{B.2}$$

In this thesis all results presented are either in outer units (no superscript), either in wall units ($^+$ superscript). Superscripts have been dropped for the velocity, the phase field and the surfactant concentration as they have the same definition in both outer and wall units (superscripts, however, are kept for both time and length scales).

C

Publications, courses and projects

C.1 Refereed journals

J1 **G. Soligo**, A. Roccon and A. Soldati. Flow topology of turbulence with surfactant-laden droplets. *Phys. Rev. Fluids*, in preparation.

J2 **G. Soligo**, A. Roccon and A. Soldati. Breakage, coalescence and size distribution of surfactant-laden droplets in turbulent flow. *J. Fluid Mech.*, 881:244–282, 2019.

J3 **G. Soligo**, A. Roccon and A. Soldati. Deformation of clean and surfactant-laden droplets in shear flow. *Meccanica* (in press), 2019.

J4 **G. Soligo**, A. Roccon and A. Soldati. Mass-conservation-improved phase field methods for turbulent multiphase flow simulation. *Acta Mech.*, 230(2):683–696, 2019.

J5 **G. Soligo**, A. Roccon and A. Soldati. Coalescence of surfactant-laden drops by Phase Field Method. *J. Comput. Phys.*, 376:1292–1311, 2019.

J6 W. Wu, **G. Soligo**, C. Marchioli, A. Soldati and U. Piomelli. Particle resuspension by a periodically forced impinging jet. *J. Fluid Mech.*, 820:284–311, 2017.

C.2 Conferences

C1 G. Labanca†, **G. Soligo**, A. Roccon and A. Soldati, Dynamics of large and deformable bubbles in turbulence, *APS-DFD Annual Meeting*, Seattle (USA), November 23–26, 2019.

C2 A. Soldati†, **G. Soligo** and A. Roccon, Breakage, coalescence and droplet size distribution of surfactant-laden droplets in wall-bounded turbulence, *APS-DFD Annual Meeting*, Seattle (USA), November 23–26, 2019.

C3 **G. Soligo**†, A. Roccon and A. Soldati, Turbulence modulations induced by a swarm of surfactant-laden droplets, *APS-DFD Annual Meeting*, Seattle (USA), November 23–26, 2019.

C4 A. Soldati, **G. Soligo** and A. Roccon†, Turbulence interactions with large bubbles, *ICMF 2018*, Rio de Janeiro (Brasil), May 19–24, 2019.

C5 **G. Soligo**†, A. Roccon and A. Soldati, Surfactant-laden droplets in wall bounded turbulence, *ICMF 2018*, Rio de Janeiro (Brasil), May 19–24, 2019.

C6 **G. Soligo**†, A. Roccon and A. Soldati, Surfactant-laden drops in wall-bounded turbulence, *Österreichisches Nationalkomitee für Teoretische und Angewandte Mechanik Meeting*, Vienna (Austria), December 7, 2018.

C7 A. Roccon†, **G. Soligo** and A. Soldati, Turbulence interactions with large bubbles, *APS-DFD Annual Meeting*, Atlanta (USA), November 18–20, 2018.

C8 G. Leloup†, **G. Soligo**, A. Roccon and A. Soldati, Mass conservation improved Phase Field Methods for turbulent multiphase flows simulations, *APS-DFD Annual Meeting*, Atlanta (USA), November 18–20, 2018.

C9 **G. Soligo**†, A. Roccon and A. Soldati, Surfactant-laden drops in wall-bounded turbulence, *APS-DFD Annual Meeting*, Atlanta (USA), November 18–20, 2018.

C10 **G. Soligo**†, A. Roccon and A. Soldati, Turbulence interaction with large drops, *Dispersed Two-Phase Flows*, Toulouse (France), September 17–19, 2018.

C11 **G. Soligo**†, A. Roccon and A. Soldati, Coalescence of surfactant-laden drops by Phase Field Method, *Dispersed Two-Phase Flows*, Toulouse (France), September 17–19, 2018.

C12 **G. Soligo**†, A. Roccon and A. Soldati, Coalescence of surfactant-laden drops by Phase Field Method, *EFMC 12*, Vienna (Austria), September 9–13, 2018.

C13 **G. Soligo**†, A. Roccon and A. Soldati, Phase Field Method to predict coalescence of clean and surfactant-laden droplets, *EuroMech Colloquium*, Venice (Italy), May 9–11, 2018.

C14 **G. Soligo**†, A. Roccon and A. Soldati, Phase Field Method to predict coalescence of clean and surfactant-laden droplets, *Austrian High-Performance Computing*, Linz (Austria), February 19–21, 2018.

C15 **G. Soligo**†, A. Roccon and A. Soldati, Turbulence interactions with large bubbles, *APS-DFD Annual Meeting*, Denver (USA), November 19-21, 2017.

† Presentation speaker.

C.3 HPC projects

P1 **Drag reduction via a bubble lubricating layer (BELUGA)** (ISCRA grant), project ID: HP10B6RWC4, 9.6 millions CPU hours on Marconi Knights Landing hosted at CINECA, Casalecchio di Reno (Italy), 2019.

P2 **Dynamics of surfactant-laden droplets in turbulence** (PRACE grant), project ID: Pra18_4646, 30 millions CPU hours on Marconi Knights Landing hosted at CINECA, Casalecchio di Reno (Italy), 2019.

P3 **Surfactant-laden droplets in wall bounded turbulence (SURFER)** (ISCRA grant), project ID: HP10BOR3UN, 10 millions CPU hours on Marconi Knights Landing hosted at CINECA, Casalecchio di Reno (Italy), 2018.

P4 **Turbulence Interactions with large bubbles (TURBINLA)** (ISCRA grant), project ID: HP10BPBIXH, 2 millions CPU hours on Marconi Broadwell (moved to Knights Landing) hosted at CINECA, Casalecchio di Reno (Italy), 2018.

P5 **Large deformable droplets in wall bounded turbulence** (VSC grant), project ID: 71164, 3 millions CPU hours on VSC-3 hosted at Vienna Scientific Cluster, Vienna (Austria), 2018.

P6 **Scalability tests** (PRACE preparatory access), project ID: 2010PA4134, 100 thousands CPU hours on Marconi Knights Landing hosted at CINECA, Casalecchio di Reno (Italy), 2017.

P7 **Viscosity-modulated breakup and coalescence of large drops in bounded turbulence (VIMODETU)** (Director's Discretionary), 1 million CPU hours on Vesta hosted at Argonne National Laboratory, Chicago (USA), 2017.

C.4 Advanced courses

A1 **Scientific Visualization**, Höchstleistungsrechenzentrum Stuttgart (HLRS), Stuttgart (Germany), October 24–25, 2019/

A2 **International HPC Summer School**, RIKEN Center for Computational Science, Kōbe (Japan), July 7–12, 2019.

A3 **CISM-JMBC Course on Complex Flows and Complex Fluids**, International Centre for Mechanical Sciences (CISM), Udine (Italy), May 13–17, 2019. Coordinated by F. Toschi.

A4 **VSC Training Course: Node-Level Performance Engineering**, Vienna Scientific Cluster (VSC), Vienna (Austria), December 5–7, 2018.

A5 **6th International advanced course on Liquid Interfaces, Drops and Sprays (LIDESP VI)**, TU Wien, Vienna (Austria), September 4–7, 2018.

A6 **Argonne Training Program on Extreme-Scale Computing (ATPESC)**, Q-Center, S. Charles (USA), July 29 - August 8, 2018.

A7 **High-Performance computing of big data for turbulence and combustion**, International Centre for Mechanical Sciences (CISM), Udine (Italy), May 21–25, 2018. Coordinated by S. Pirozzoli and T.K. Sengupta.

A8 **VSC Training Course: Parallel I/O**, Vienna Scientific Cluster (VSC), Vienna (Austria), December 5–6, 2017.

A9 **Flowing Matter**, International Centre for Mechanical Sciences (CISM), Udine (Italy), September 25–29, 2017. Coordinated by B. Dollet and B. Mehlig.

A10 **VSC Training Course: Shared memory parallelization with OpenMP**, Vienna Scientific Cluster (VSC), Vienna (Austria), June 8–9, 2017.

A11 **26th Summer School on Parallel Computing**, CINECA, Casalecchio di Reno (Italy), May 15–26, 2017.

A12 **VSC Training Course: Parallelization with MPI**, Vienna Scientific Cluster (VSC), Vienna (Austria), May 9–11, 2017.

A13 **VSC Training Course: Introduction to Working on the VSC-3 Cluster**, Vienna Scientific Cluster (VSC), Vienna (Austria), April 27, 2017.

A14 **Advanced CFD techniques for turbulent flows: theory and applications**, University of Udine, Udine (Italy), May 19–22, 2015. Coordinated by U. Piomelli.

Acknowledgements

I would like to thank my PhD supervisor, Professor Alfredo Soldati, who first introduced me to the fascinating world of Fluid Mechanics during my Bachelor and Master degrees at the University of Udine and then gave me the opportunity to work on such an interesting topic during my PhD. I would also like to thank Professor Cristian Marchioli, my PhD co-supervisor, for the interesting discussions and the clever questions that gave new inputs to my work.

A special thank goes to the committee members and reviewers, Professor Luca Brandt and Professor Günter Brenn, who took time off their agenda for a thorough and careful review of the thesis; their insightful observations, suggestions and feedback have been greatly appreciated.

I would also like to thank all the friends and colleagues from the University of Udine and from the Institute of Fluid Mechanics and Heat Transfer at the TU Wien, who always supported me during all the three years of my PhD. Among them, I would like to thank, in particular, Alessio for all the critical discussions and his keen eye for graphical details, Francesco for the great lunchtime conversations and Mobin for hosting dinners and board games. A special mention goes to Kathi, for her friendship and for always being willing to help with translation from german.

A final thank goes to my parents for their continuous and tireless support throughout all these years.

Bibliography

[1] S. Afkhami, P. Yue, and Y. Renardy. A comparison of viscoelastic stress wakes for two-dimensional and three-dimensional Newtonian drop deformations in a viscoelastic matrix under shear. *Phys. Fluids*, 21(7):072106, 2009.

[2] R.S. Allan, G.E. Charles, and S.G. Mason. The approach of gas bubbles to a gas/liquid interface. *J. Colloid Sci.*, 16(2):150–165, 1961.

[3] D.M. Anderson, G.B. McFadden, and A.A. Wheeler. Diffuse interface methods in fluid mechanics. *Annu. Rev. Fluid Mech.*, 30(1):139–165, 1998.

[4] R. Andersson and B. Andersson. On the breakup of fluid particles in turbulent flows. *AIChE J.*, 52(6):2020–2030, 2006.

[5] R. Aris. *Vectors, Tensors and the Basic Equations of Fluid Mechanics.* Dover Publications, 1989.

[6] F. Azizi and A.M. Al Taweel. Turbulently flowing liquid-liquid dispersions. Part I: Drop breakage and coalescence. *Chem. Eng. J.*, 166(2):715–725, 2011.

[7] E. Babinsky and P.E. Sojka. Modeling drop size distributions. *Prog. Energ. Combust.*, 28:303–329, 2002.

[8] V.E. Badalassi, H.D. Ceniceros, and S. Banerjee. Computation of multiphase systems with phase field models. *J. Comput. Phys*, 190(2):371–397, 2003.

[9] M. Bayareh and S. Mortazavi. Binary collision of drops in simple shear flow at finite Reynolds numbers: Geometry and viscosity ratio effects. *Adv. Eng. Softw.*, 42(8):604–611, 2011.

[10] I.B. Bazhlekov, P.D. Anderson, and H.E. Meijer. Numerical investigation of the effect of insoluble surfactants on drop deformation and breakup in simple shear flow. *J. Colloid Interf. Sci.*, 298(1):369–394, 2006.

[11] T. Biben and C. Misbah. Tumbling of vesicles under shear flow within an advected-field approach. *Phys. Rev. E*, 67(3):031908, 2003.

[12] G. Boffetta and A. Mazzino. Incompressible Rayleigh–Taylor turbulence. *Annu. Rev. Fluid Mech.*, 49:119–143, 2017.

[13] D.E. Brown and K. Pitt. Drop size distribution of stirred non-coalescing liquid-liquid system. *Chem. Eng. Sci.*, 27(3):577–583, 1972.

[14] W.K. Brown and K.H. Wohletz. Derivation of the Weibull distribution based on physical principles and its connection to the Rosin-Rammler and lognormal distributions. *J. Appl. Phys.*, 78(4):2758–2763, 1995.

[15] B. Bunner. Direct numerical simulations of three-dimensional bubbly flows. *Phys. Fluids*, 11(8), 1999.

[16] J.W. Cahn and J.E. Hilliard. Free Energy of a Nonuniform System. I. Interfacial Free Energy. *J. Chem. Phys.*, 28:258–267, 1958.

[17] J.W. Cahn and J.E. Hilliard. Free Energy of a Nonuniform System. II. Thermodynamic Basis. *J. Chem. Phys.*, 30(5):1121–1124, 1959.

[18] J.W. Cahn and J.E. Hilliard. Free Energy of a Nonuniform System. III. Nucleation in a Two-Component Incompressible Fluid. *J. Chem. Phys.*, 31:688, 1959.

[19] C. Canuto, M.Y. Hussaini, A.M. Quarteroni, and T.A. Zang. *Spectral Methods in Fluid Dynamics.* Springer-Verlag, 1988.

[20] S.L. Ceccio. Friction drag reduction of external flows with bubble and gas injection. *Annu. Rev. Fluid Mech.*, 42:183–203, 2010.

[21] C. Chang and E. Franses. Adsorption dynamics of surfactants at the air/water interface: a critical review of mathematical models, data, and mechanisms. *Colloids Surf. A*, 100:1–45, 1995.

[22] G.E. Charles and S.G. Mason. The coalescence of liquid drops with flat liquid/liquid interfaces. *J. Colloid Sci.*, 15(3):236–267, 1960.

[23] E.G. Chatzi and C. Kiparissides. Drop size distributions in high holdup fraction dispersion systems: effect of the degree of hydrolysis of PVA stabilizer. *Chem. Eng. Sci.*, 49(24):5039 – 5052, 1994.

[24] D. Chen, R. Cardinaels, and P. Moldenaers. Effect of confinement on droplet coalescence in shear flow. *Langmuir*, 22(25):12885–12893, 2009.

[25] H.T. Chen and S. Middleman. Drop size distribution in agitated liquid-liquid systems. *AIChE J.*, 13(5):989–995, 1967.

[26] N. Chen, T. Kuhl, R. Tadmor, Q. Lin, and J. Israelachvili. Large deformations during the coalescence of fluid interfaces. *Phys. Rev. Lett.*, 92:024501, 2004.

[27] S. Chen and G.D. Doolen. Lattice Boltzmann method for fluid flows. *Annu. Rev. Fluid Mech.*, 30(1):329–364, 1998.

[28] P.Y. Chow and L.M. Gan. Microemulsion polymerizations and reactions. *Adv. Polym. Sci.*, 175(February 2005):257–298, 2005.

[29] D. Colella, D. Vinci, R. Bagatin, M. Masi, and E.A. Bakr. A study on coalescence and breakage mechanisms in three different bubble columns. *Chem. Eng. Sci.*, 54(21):4767–4777, 1999.

[30] B. Dai and L.G. Leal. The mechanism of surfactant effects on drop coalescence. *Phys. Fluids*, 20(4):1–13, 2008.

[31] B.J. Daly. Numerical Study of Two Fluid Rayleigh-Taylor Instability. *Phys. Fluids*, 10(2):297–307, 1967.

[32] R.C. Darton and K.H. Sun. The effect of surfactant on foam and froth properties. *Chem. Eng. Res. Des.*, 77(6):535–542, 1999.

[33] P. De Bruyn, R. Cardinaels, and P. Moldenaers. The effect of geometrical confinement on coalescence efficiency of droplet pairs in shear flow. *J. Colloid Interf. Sci.*, 409:183–192, 2013.

[34] G.B. Deane and M.D. Stokes. Scale dependence of bubble creation mechanisms in breaking waves. *Nature*, 418(6900):839, 2002.

[35] L. Deike, W.K. Melville, and S. Popinet. Air entrainment and bubble statistics in breaking waves. *J. Fluid Mech.*, 801:91–129, 2016.

[36] J.M. Delhaye and P. Bricard. Interfacial area in bubbly flow: experimental data and correlations. *Nucl. Eng. Des.*, 151(1):65–77, 1994.

[37] S.R. Derkach. Rheology of emulsions. *Adv. Colloid Interfac.*, 151(1):1 – 23, 2009.

[38] O. Desjardins, V. Moureau, and H. Pitsch. An accurate conservative level set/ghost fluid method for simulating turbulent atomization. *J. Comput. Phys.*, 227:8395–8416, 2008.

[39] H. Ding and C. Yuan. On the diffuse interface method using a dual-resolution cartesian grid. *J. Comput. Phys.*, 273:243 – 254, 2014.

[40] H. Ding, P.D.M. Spelt, and C. Shu. Diffuse interface model for incompressible two-phase flows with large density ratios. *J. Comput. Phys.*, 226(2):2078–2095, 2007.

[41] L.G. Dobbs. Pulmonary surfactant. *Annu. Rev. Med.*, 40(1):431–446, 1989.

[42] M.S. Dodd and A. Ferrante. On the interaction of Taylor length scale size droplets and isotropic turbulence. *J. Fluid Mech.*, 806:356–412, 2016.

[43] C.D. Eastwood, L. Armi, and J.C. Lasheras. The breakup of immiscible fluids in turbulent flows. *J. Fluid Mech.*, 502:309–333, 2004.

[44] J. Eggers. Theory of drop formation. *Phys. Fluids*, 7(5):941–953, 1995.

[45] C.D. Eggleton, T.M. Tsai, and K.J. Stebe. Tip streaming from a drop in the presence of surfactants. *Phys. Rev. Lett.*, 87(4):048302, 2001.

[46] S. Elghobashi. Direct numerical simulation of turbulent flows laden with droplets or bubbles. *Annu. Rev. Fluid Mech.*, 51(1):217–244, 2019.

[47] S. Engblom, M. Do-Quang, G. Amberg, and A.K. Tornberg. On diffuse interface modeling and simulation of surfactants in two-phase fluid flow. *Commun. Comput. Phys.*, 14(4):879–915, 2013.

[48] H. Farhat, F. Celiker, T. Singh, and J.S. Lee. A hybrid lattice Boltzmann model for surfactant-covered droplets. *Soft Matter*, 7(5):1968–1985, 2011.

[49] R.P. Fedkiw, T. Aslam, B. Merriman, and S. Osher. A non-oscillatory Eulerian approach to interfaces in multimaterial flows (the ghost fluid method). *J. Comput. Phys.*, 152(2):457–492, 1999.

[50] M. Frigo and S.G. Johnson. The design and implementation of FFTW3. *Proceedings of the IEEE*, 93(2):216–231, 2005. Special issue on "Program Generation, Optimization, and Platform Adaptation".

[51] C. Garrett, M. Li, and D. Farmer. The connection between bubble size spectra and energy dissipation rates in the upper ocean. *J. Phys. Oceanogr.*, 30(9): 2163–2171, 2000.

[52] F. Gibou, R. Fedkiw, and S. Osher. A review of level-set methods and some recent applications. *J. Comput. Phys.*, 353:82–109, 2018.

[53] N. Grizzuti and O. Bifulco. Effects of coalescence and breakup on the steady-state morphology of an immiscible polymer blend in shear flow. *Rheol. Acta*, 36 (4):406–415, 1997.

[54] J.-L. Guermond and L. Quartapelle. A Projection FEM for Variable Density Incompressible Flows. *J. Comput. Phys.*, 165(1):167 – 188, 2000. ISSN 0021-9991.

[55] S. Guido and M. Simeone. Binary collision of drops in simple shear flow by computer-assisted video optical microscopy. *J. Fluid Mech.*, 357:1–20, 1998.

[56] S. Guido and M. Villone. Three-dimensional shape of a drop under simple shear flow. *J. Rheol.*, 42:395–415, 1998.

[57] J.W. Ha, Y. Yoon, and L.G. Leal. The effect of compatibilizer on the coalescence of two drops in flow. *Phys. Fluids*, 15(4):849–867, 2003.

[58] X. He, S. Chen, and R. Zhang. A Lattice Boltzmann Scheme for Incompressible Multiphase Flow and Its Application in Simulation of Rayleigh-Taylor Instability. *J. Comput. Phys.*, 152(2):642 – 663, 1999.

[59] X. He, S. Chen, and R. Zhang. A Lattice Boltzmann Scheme for Incompressible Multiphase Flow and Its Application in Simulation of Rayleigh–Taylor Instability. *J. Comput. Phys.*, 152(2):642 – 663, 1999. ISSN 0021-9991.

[60] M. Herrmann. On Simulating Primary Atomization Using The Refined Level Set Grid Method. *Atomization Spray*, 21:283–301, 2011.

[61] J.O. Hinze. Fundamentals of the hydrodynamic mechanism of splitting in dispersion processes. *AIChE J.*, 1(3):289–295, 1955.

[62] C.W. Hirt and B.D. Nichols. Volume of fluid (VOF) method for the dynamics of free boundaries. *J. Comput. Phys.*, 39(1):201–225, 1981.

[63] C.T. Hsu, C.H. Chang, and S.Y. Lin. Study on surfactant adsorption kinetics: effects of interfacial curvature and molecular interaction. *Langmuir*, 16(3):1211–1215, 2000.

[64] M.Y. Hussaini and T.A. Zang. Spectral methods in fluid dynamics. *Annu. Rev. Fluid Mech.*, 19(1):339–367, 1987.

[65] M. Ikura, M. Stanciulescu, and E. Hogan. Emulsification of pyrolysis derived bio-oil in diesel fuel. *Biomass Bioenergy*, 24(3):221–232, 2003.

[66] T. Inamuro, R. Tomita, and F. Ogino. Lattice Boltzmann simulations of drop deformation and breakup in shear flows. *Int. J. Mod. Phys. B*, 17(1 & 2):21–26, 2003.

[67] N. Ioannou, H. Liu, and Y.H. Zhang. Droplets dynamics in confinement. *J. Comput. Sci.*, 17:463–474, 2016.

[68] Z. Izri, M.N. Van Der Linden, S. Michelin., and O. Dauchot. Self-propulsion of pure water droplets by spontaneous marangoni-stress-driven motion. *Phys. Rev. Lett.*, 113(24):1–5, 2014.

[69] D. Jacqmin. Calculation of two-phase Navier–Stokes flows using phase-field modeling. *J. Comput. Phys.*, 155(1):96–127, 1999.

[70] A.J. James and J. Lowengrub. A surfactant-conserving volume-of-fluid method for interfacial flows with insoluble surfactant. *J. Comput. Phys.*, 201(2):685–722, 2004.

[71] H. Ju, Y. Jiang, T. Geng, Y. Wang, and C. Zhang. Equilibrium and dynamic surface tension of quaternary ammonium salts with different hydrocarbon chain length of counterions. *J. Mol. Liq.*, 225:606–612, 2017.

[72] P.M. Kamat, B.W. Wagoner, S.S. Thete, and O.A. Basaran. Role of Marangoni stress during breakup of surfactant-covered liquid threads: Reduced rates of thinning and microthread cascades. *Phys. Rev. Fluids*, 3:043602, 2018.

[73] J. Kamp, J. Villwock, and M. Kraume. Drop coalescence in technical liquid/liquid applications: a review on experimental techniques and modeling approaches. *Rev. Chem. Eng.*, 33(1):1–47, 2017.

[74] A.J. Karabelas. Droplet size spectra generated in turbulent pipe flow of dilute liquid/liquid dispersions. *AIChE J.*, 24(2):170–180, 1978.

[75] J.E. Kelly and M.S. Kazimi. Interfacial exchange relations for two-fluid vapor-liquid flow: a simplified regime-map approach. *Nucl. Sci. Eng.*, 81(3):305–318, 1982.

[76] J. Kim. A continuous surface tension force formulation for diffuse-interface models. *J. Comput. Phys*, 204(2):784–804, 2005.

[77] J. Kim. A generalized continuous surface tension force formulation for phase-field models for multi-component immiscible fluid fows. *Comput. Method Appl. M.*, 189:3105–3112, 2009.

[78] J. Kim. Phase-Field Models for Multi-Component Fluid Flows. *Commun. Comput. Phys.*, 12(3):613–661, 2012.

[79] J. Kim and J. Lowengrub. Phase field modeling and simulation of three-phase flows. *Interfaces and free boundaries*, 7(4):435, 2005.

[80] A. Kiyomi and Y. Fumitake. Bubble size, interfacial area, and liquid-phase mass transfer coefficient in bubble columns. *Ind. Eng. Chem. Process Des. Dev.*, 13 (1):84–91, 1974.

[81] A.E. Komrakova, O. Shardt, D. Eskin, and J.J. Derksen. Lattice Boltzmann simulations of drop deformation and breakup in shear flow. *Int. J. Multiphas. Flow*, 59:24–43, 2014.

[82] S. Komura and H. Kodama. Two-order-parameter model for an oil-water-surfactant system. *Phys. Rev. E*, 55(2):1722–1727, 1997.

[83] D.J. Korteweg. Sur la forme que prennent les equations du mouvements des fluides si l'on tient compte des forces capillaires causées par des variations de densité considérables mais continues et sur la théorie de la capillarité dans l'hypothèse d'une variation continue de la densité. *Archives Néerlandaises des Sciences Exactes et Naturelles*, 6:1–24, 1901.

[84] I. Kralova and J. Sjöblom. Surfactants used in food industry: a review. *J. Disper. Sci. Technol.*, 30(9):1363–1383, 2009.

[85] G.P. Kumar and P. Rajeshwarrao. Nonionic surfactant vesicular systems for effective drug delivery an overview. *Acta Pharm. Sin. B*, 1(4):208–219, 2011.

[86] S. Kwak and C. Pozrikidis. Adaptive Triangulation of Evolving, Closed, or Open Surfaces by the Advancing-Front Method. *J. Comput. Phys.*, 145(1):61 – 88, 1998. ISSN 0021-9991.

[87] M. Kwakkel, W.-P. Breugem, and B.J. Boersma. Extension of a CLSVOF method for droplet-laden flows with a coalescence/breakup model. *J. Comput. Phys.*, 253:166–188, 2013.

[88] M.C. Lai, Y.H. Tseng, and H. Huang. An immersed boundary method for interfacial flows with insoluble surfactant. *J. Comput. Phys.*, 227(15):7279–7293, 2008.

[89] M.C. Lai, Y.H. Tseng, and H. Huang. Numerical simulation of moving contact lines with surfactant by immersed boundary method. *Commun. Comput. Phys.*, 8(4):735, 2010.

[90] A. Lamorgese, R. Mauri, and L.M.C. Sagis. Modeling soft interface dominated systems: A comparison of phase field and Gibbs dividing surface models. *Phys. Rep.*, 675:1–54, 2017.

[91] M. Laradji, H. Guo, M. Grant, and M.J. Zuckermann. The effect of surfactants on the dynamics of phase separation. *J. Phys. - Conden. Mat.*, 4:6715–6728, 1992.

[92] J.C. Lasheras, C. Eastwood, C. Martınez-Bazán, and J.L. Montanes. A review of statistical models for the break-up of an immiscible fluid immersed into a fully developed turbulent flow. *Int. J. Multiphas. Flow*, 28(2):247–278, 2002.

[93] L.G. Leal. Flow induced coalescence of drops in a viscous fluid. *Phys. Fluids*, 16(6):1833–1851, 2004.

[94] T.W. Lee and D. Robinson. Calculation Of The Drop Size Distribution And Velocities From The Integral Form Of The Conservation Equations. *Combust. Sci. Technol.*, 183:271–284, 2011.

[95] J. Li, Y. Renardy, and M. Renardy. Numerical simulation of breakup of a viscous drop in simple shear flow through a volume-of-fluid method. *Phys. Fluids*, 12 (2):269–282, 2000.

[96] Y. Li, J. Choi, and J. Kim. A phase-field fluid modeling and computation with interfacial profile correction term. *Commun. Nonlinear Sci.*, 30(1-3):84–100, 2016.

[97] Y. Liao and D. Lucas. A literature review on mechanisms and models for the coalescence process of fluid particles. *Chem. Eng. Sci.*, 65:2851 – 2864, 2010.

[98] H. Liu, Y. Ba, L. Wu, Z. Li, G. Xi, and Y. Zhang. A hybrid lattice Boltzmann and finite difference method for droplet dynamics with insoluble surfactants. *J. Fluid Mech.*, 837:381–412, 2018.

[99] M. Loewenberg and E.J. Hinch. Numerical simulation of a concentrated emulsion in shear flow. *J. Fluid Mech.*, 321:395–419, 1996.

[100] D. López-Diaz, I. Garcia-Mateos, and M.M. Velázquez. Surface properties of mixed monolayers of sulfobetaines and ionic surfactants. *J. Colloid Interf. Sci.*, 299:858–866, 2006.

[101] J. Lovick, A.A. Mouza, S.V. Paras, G.J. Lye, and P. Angeli. Drop size distribution in highly concentrated liquid-liquid dispersions using a light back scattering method. *J. Chem. Technol. Biotechnol.*, 80(5):545–552, 2005.

[102] J. Lu and G. Tryggvason. Effect of bubble deformability in turbulent bubbly upflow in a vertical channel. *Phys. Fluids*, 20(4), 2008.

[103] J. Lu and G. Tryggvason. Direct numerical simulations of multifluid flows in a vertical channel undergoing topology changes. *Phys. Rev. Fluids*, 3:084401, 2018.

[104] J. Lu and G. Tryggvason. Multifluid flows in a vertical channel undergoing topology changes: Effect of void fraction. *Phys. Rev. Fluids*, 4:084301, 2019.

[105] J. Lu, M. Muradoglu, and G. Tryggvason. Effect of insoluble surfactant on turbulent bubbly flows in vertical channels. *Int. J. Multiphas. Flow*, 95:135–143, 2017.

[106] H. Luo and H.F. Svendsen. Theoretical Model for Drop and Bubble Breakup in Turbulent Dispersions. *AIChE J.*, 42(5):1225 – 1233, 1996.

[107] S. Maaß, A. Gäbler, A. Zaccone, A.R. Paschedag, and M. Kraume. Experimental Investigations and Modelling of Breakage Phenomena in Stirred Liquid/Liquid Systems. *Chem. Eng. Res. Des.*, 85(5):703–709, 2007.

[108] F. Magaletti, F. Picano, M. Chinappi, L. Marino, and C.M. Casciola. The sharp-interface limit of the Cahn–Hilliard/Navier–Stokes model for binary fluids. *J. Fluid Mech.*, 714:95–126, 2013.

[109] T. Menard, S. Tanguy, and A. Berlemont. Coupling level set / VOF / ghost fluid methods : Validation and application to 3D simulation of the primary break-up of a liquid jet. *Int. J. Multiphas. Flow*, 33:510–524, 2007.

[110] R.A. Mugele and H.D. Evans. Droplet size distribution in sprays. *Ind. Eng. Chem. Res.*, 43(6):1317–1324, 1951.

[111] A. Muggeridge, A. Cockin, K. Webb, H. Frampton, I. Collins, T. Moulds, and P. Salino. Recovery rates, enhanced oil recovery and technological limits. *Phil. Trans. R. Soc. A*, 372(2006):20120320, 2014.

[112] M. Muradoglu and G. Tryggvason. Simulations of soluble surfactants in 3D multiphase flow. *J. Comput. Phys.*, 274:737–757, 2014.

[113] Y. Murai, H. Fukuda, Y. Oishi, Y. Kodama, and F. Yamamoto. Skin friction reduction by large air bubbles in a horizontal channel flow. *Int. J. Multiphas. Flow*, 33(2):147–163, 2007.

[114] P.K. Notz and O.A. Basaran. Dynamics and breakup of a contracting liquid filament. *J. Fluid Mech.*, 512:223–256, 2004.

[115] S. Osher and J. Sethian. Fronts Propagating with Curvature-Dependent Speed: Algorithms Based on Hamilton-Jacobi Formulations. *J. Comput. Phys.*, 49:12–49, 1988.

[116] S. Osher and J. Sethian. A Level Set Approach for computing solutions to incompressible Two-Phase Flow. *J. Comput. Phys.*, 114:12–49, 1994.

[117] K.L. Pan, Y.H. Tseng, J.C. Chen, K.L. Huang, C.H. Wang, and M.C. Lai. Controlling droplet bouncing and coalescence with surfactant. *J. Fluid Mech.*, 799:603–636, 2016.

[118] Y. Pawar and J. Stebe. Marangoni effects on drop deformation in an extensional flow: The role of surfactant physical chemistry. I. Insoluble surfactants. *Phys. Fluids*, 8(7):1738–1751, 1996.

[119] R. Pereira, I. Ashton, B. Sabbaghzadeh, J.D. Shutler, and R.C. Upstill-Goddard. Reduced air-sea CO_2 exchange in the Atlantic Ocean due to biological surfactants. *Nat. Geosci.*, 11:492–496, 2018.

[120] P. Perlekar, L. Biferale, and M. Sbragaglia. Droplet size distribution in homogeneous isotropic turbulence. *Phys. Fluids*, 065101:1–10, 2012.

[121] R. Peyret. *Spectral Methods for Incompressible Viscous Flow*, volume 148. Springer Science+Business Media, 2002.

[122] A. Piedfert, B. Lalanne, O. Masbernat, and F. Risso. Numerical simulations of a rising drop with shape oscillations in the presence of surfactants. *Phys. Rev. Fluids*, 3:103605, 2018.

[123] A. Prosperetti and G. Tryggvason. *Computational Methods for Multiphase Flow.* Cambridge Press, 2009.

[124] J.M. Rallison. The Deformation of Small Viscous Drops and Bubbles in Shear Flows. *Annu. Rev. Fluid Mech.*, 16(1):45–66, 1984.

[125] L. Rekvig and D. Frenkel. Molecular simulations of droplet coalescence in oil/water/surfactant systems. *J. Chem. Phys.*, 127(13):134701, 2007.

[126] Y. Renardy, M. Renardy, and V. Cristini. A new volume-of-fluid formulation for surfactants and simulations of drop deformation under shear at a low viscosity ratio. *Eur. J. Mech. B-Fluid*, 21(1):49–59, 2002.

[127] W.J. Rider and D.B. Kothe. Reconstructing volume tracking. *J. Comput. Phys.*, 141(2):112–152, 1998.

[128] A. Roccon, M. De Paoli, F. Zonta, and A. Soldati. Viscosity-modulated breakup and coalescence of large drops in bounded turbulence. *Phys. Rev. Fluids*, 2: 083603, 2017.

[129] M.J. Rosen and J.T. Kunjappu. *Surfactants and interfacial phenomena.* John Wiley & Sons, 2012.

[130] M.E. Rosti, F. De Vita, and L. Brandt. Numerical simulations of emulsions in shear flows. *Acta Mech.*, 230:667–682, 2019.

[131] M.E. Rosti, Z. Ge, S.S. Jain, M.S. Dodd, and L. Brandt. Droplets in homogeneous shear turbulence. *J. Fluid Mech.*, 876:962–984, 2019.

[132] W.C. Sanders, E.C. Winkel, D.R. Dowling, M. Perlin, and S.L. Ceccio. Bubble friction drag reduction in a high-Reynolds-number flat-plate turbulent boundary layer. *J. Fluid Mech.*, 552:353–380, 2006.

[133] S. Santra, R. Tapec, N. Theodoropoulou, J. Dobson, A. Hebard, and W. Tan. Synthesis and characterization of silica-coated iron oxide nanoparticles in microemulsion: The effect of nonionic surfactants. *Langmuir*, 17(10):2900–2906, 2001.

[134] L. Scarbolo, F. Bianco, and A. Soldati. Coalescence and breakup of large droplets in turbulent channel flow. *Phys. Fluids*, 27(7):073302, 2015.

[135] L. Scarbolo, F. Bianco, and A. Soldati. Turbulence modification by dispersion of large deformable droplets. *Eur. J. Mech. B-Fluid*, 55:294–299, 2016.

[136] R. Scardovelli and S. Zaleski. Direct numerical simulation of free-surface and interfacial flow. *Annu. Rev. Fluid Mech.*, 31(1):567–603, 1999.

[137] J.A. Sethian. *Level set methods and fast marching methods: evolving interfaces in computational geometry, fluid mechanics, computer vision, and materials science*, volume 3. Cambridge university press, 1999.

[138] X. Shan and H. Chen. Lattice Boltzmann model for simulating flows with multiple phases and components. *Phys. Rev. E*, 47(3):1815, 1993.

[139] M. Shapira and S. Haber. Low Reynolds number motion of a droplet in shear flow including wall effects. *Int. J. Multiphas. Flow*, 16(2):305–321, 1990.

[140] D.H. Sharp. An overview of Rayleigh-Taylor instability. *Physica D*, 12(1):3 – 18, 1984. ISSN 0167-2789.

[141] R.K. Singh and K. Sarkar. Effects of viscosity ratio and three dimensional positioning on hydrodynamic interactions between two viscous drops in a shear flow at finite inertia. *Phys. Fluids*, 21(10):103303, 2009.

[142] R. Skartlien, E. Sollum, and H. Schumann. Droplet size distributions in turbulent emulsions: Breakup criteria and surfactant effects from direct numerical simulations. *J. Chem. Phys.*, 139(17), 2013.

[143] A. Soldati and S. Banerjee. Turbulence modification by large-scale organized electrohydrodynamic flows. *Phys. Fluids*, 10(7):1742–1756, 1998.

[144] G. Soligo, A. Roccon, and A. Soldati. Mass-conservation-improved Phase Field Methods for turbulent multiphase flow simulation. *Acta Mech.*, 230(2):683–696, 2019.

[145] G. Soligo, A. Roccon, and A. Soldati. Coalescence of surfactant-laden drops by Phase Field Method. *J. Comput. Phys.*, 376:1292–1311, 2019.

[146] P. Sreehari, M.K. Borg, M.V. Chubynsky, J.E. Sprittles, and J.M. Reese. Droplet coalescence is initiated by thermal motion. *Phys. Rev. Lett.*, 122(10):104501, 2019.

[147] H.A. Stone and L.G. Leal. The effects of surfactants on drop deformation and breakup. *J. Fluid Mech.*, 220:161–186, 1990.

[148] Y. Sun and C. Beckermann. Sharp interface tracking using the phase-field equation. *J. Comput. Phys.*, 220(2):626–653, 2007.

[149] G. Suryanarayana and P. Gosh. Adsorption and Coalescence in Mixed-Surfactant Systems: Air-Water Interface. *Ind. Eng. Chem. Res.*, 49:1711–1724, 2010.

[150] N. Takada, A. Tomiyama, and S. Hosokawa. Lattice Boltzmann simulation of drops in a shear flow. *Proceedings of the 4th ASME/JSME joint fluids engineering conference, New York, USA*, 2003.

[151] S. Takagi and Y. Matsumoto. Surfactant effects on bubble motion and bubbly flows. *Annu. Rev. Fluid Mech.*, 43:615–636, 2011.

[152] H. Tang, L.C. Wrobel, and Z. Fan. Tracking of immiscible interfaces in multiple-material mixing processes. *Comp. Mater. Sci.*, 29:103–118, 2004.

[153] G.I. Taylor. The Viscosity of a Fluid containing Small Drops of Another Fluid. *Proc. R. Soc. Lon. Ser.-A*, 138:41–48, 1932.

[154] G.I. Taylor. The formation of emulsions in definable fields of flows. *Proc. Royal Soc. A*, 146:501–523, 1934.

[155] P. Than, L. Preziosi, D.D. Joseph, and M. Arney. Measurement of interfacial tension between immiscible liquids with the spinning rod tensiometer. *J. Colloid Interface Sci.*, 124(2):552 – 559, 1988.

[156] V.P. Torchilin. Structure and design of polymeric surfactant-based drug delivery systems. *J. Control. Release*, 73(2-3):137–172, 2001.

[157] G. Tryggvason. Numerical simulations of the Rayleigh-Taylor instability. *J. Comput. Phys.*, 75(2):253 – 282, 1988. ISSN 0021-9991.

[158] G. Tryggvason, B. Bunner, A. Esmaeeli, D. Juric, W. Tauber, J. Han, S. Nas, and Y. Jan. A front-tracking method for the computations of multiphase flow. *J. Comput. Phys.*, 759:708–759, 2001.

[159] G. Tryggvason, R. Scardovelli, and S. Zaleski. *Direct Numerical Simulations of Gas-Liquid Multiphase Flows.* Cambridge University Press, 2011.

[160] C. Tsouris and L.L. Tavlarides. Breakage and coalescence models for drops in turbulent dispersions. *AIChE J.*, 40(3):395–406, 1994.

[161] S. Unverdi and G. Trygvasson. A Front-Tracking Method for Viscous , Incompressible , Multi-fluid Flows. *J. Comput. Phys.*, 100(1), 1992.

[162] K.J. Valentas and N.R. Amundson. Breakage and coalescence in dispersed phase systems. *Ind. Eng. Chem. Fundam.*, 5(4):533–542, 1966.

[163] T.H. van den Berg, D.P.M. van Gils, D.P. Lathrop, and D. Lohse. Bubbly turbulent drag reduction is a boundary layer effect. *Phys. Rev. Lett.*, 98:084501, 2007.

[164] R.G.M. van der Sman and S. van der Graaf. Diffuse interface model of surfactant adsorption onto flat and droplet interfaces. *Rheol. Acta*, 46(1):3–11, 2006.

[165] D.P.M. van Gils, D. Narezo Guzman, C. Sun, and D. Lohse. The importance of bubble deformability for strong drag reduction in bubbly turbulent Taylor–Couette flow. *J. Fluid Mech.*, 722:317–347, 2013.

[166] A. Vananroye, P. Van Puyvelde, and P. Moldenaers. Effect of confinement on the steady-state behavior of single droplets during shear flow. *J. Rheol.*, 51: 139–153, 2007.

[167] R.A. Verschoof, R.C.A. Van Der Veen, C. Sun, and D. Lohse. Bubble drag reduction requires large bubbles. *Phys. Rev. Lett*, 117(10):104502, 2016.

[168] C.Y. Wang and R.V. Calabrese. Drop breakup in turbulent stirred-tank contactors. Part II: Relative influence of viscosity and interfacial tension. *AIChE J.*, 32(4):667–676, 1986.

[169] C.Y. Wang, C.B. Zhang, X.Y. Huang, X.D. Liu, and Y.P. Chen. Hydrodynamics of passing-over motion during binary droplet collision in shear flow. *Chinese Phys. B*, 25(10):108202, 2016.

[170] Y. Wang, C. Shu, H.B. Huang, and C.J. Teo. Multiphase lattice Boltzmann flux solver for incompressible multiphase flows with large density ratio. *J. Comput. Phys.*, 280:404 – 423, 2015. ISSN 0021-9991.

[171] Y. Wang, C. Shu, J.Y. Shao, J. Wu, and X.D. Niu. A mass-conserved diffuse interface method and its application for incompressible multiphase flows with large density ratio. *J. Comput. Phys.*, 290:336 – 351, 2015. ISSN 0021-9991.

[172] R.M. Weinheimer, D.E. Fennell, and E.L. Cussler. Diffusion in surfactant solutions. *J. Colloid Interface Sci.*, 80(2):357 – 368, 1981.

[173] O. Wurl, E. Wurl, L. Miller, K. Johnson, and S. Vagle. Formation and global distribution of sea-surface microlayers. *Biogeosciences*, 8(1):121–135, 2011.

[174] J.H. Xu. A level-set method for interfacial flows with surfactant. *J. Comput. Phys.*, 212:590–616, 2006.

[175] J.J. Xu and H.K. Zhao. An Eulerian formulation for solving partial differential equations along a moving interface. *SIAM J. Sci. Comput.*, 19(1):573–594, 2003.

[176] J.J. Xu, Z. Li, J. Lowengrub, and H. Zhao. Numerical study of surfactant-laden drop-drop interactions. *Commun. Comput. Phys.*, 10(2):453–473, 2011.

[177] T. Ye, N. Phan-Thien, and C.T. Lim. Particle-based simulations of red blood cells - A review. *J. Biomech.*, 49(11):2255–2266, 2016.

[178] D.L. Youngs. Time-dependent multi-material flow with large fluid distortion. *Numerical Methods for Fluid Dynamics*, pages 273–285, 1982.

[179] P. Yue, J.J. Feng, C. Liu, and J. Shen. A diffuse-interface method for simulating two-phase flows of complex fluids. *J. Fluid Mech.*, 515(1):293–317, 2004.

[180] P. Yue, J.J. Feng, C. Liu, and J. Shen. Diffuse-interface simulations of drop coalescence and retraction in viscoelastic fluids. *J. Non-Newton. Fluid*, 129(3): 163–176, 2005.

[181] P. Yue, C. Zhou, J.J. Feng, C.F. Ollivier-Gooch, and H.H. Hu. Phase-field simulations of interfacial dynamics in viscoelastic fluids using finite elements with adaptive meshing. *J. Comput. Phys.*, 219:47–67, 2006.

[182] P. Yue, C. Zhou, and J.J. Feng. Spontaneous shrinkage of drops and mass conservation in phase-field simulations. *J. Comput. Phys.*, 223(1):1–9, 2007.

[183] P. Yue, C. Zhou, and J.J. Feng. Sharp-interface limit of the Cahn–Hilliard model for moving contact lines. *J. Fluid Mech.*, 645(8):279, 2010.

[184] A. Yun, Y. Li, and J. Kim. A new phase-field model for a water-oil-surfactant system. *Appl. Math. Comput.*, 229:422–432, 2014.

[185] Y. Zhang and W. Ye. A Flux-Corrected Phase-Field Method for Surface Diffusion. *Commun. Comput. Phys.*, 22(2):422–440, 2017.

[186] C. Zhou, P. Yue, J.J. Feng, C.F. Ollivier-Gooch, and H.H. Hu. 3D phase-field simulations of interfacial dynamics in Newtonian and viscoelastic fluids. *J. Comput. Phys.*, 229:498–511, 2010.

[187] H. Zhou and C. Pozrikidis. The flow of suspensions in channels: Single files of drops. *Phys. Fluids*, 5:311–324, 1993.